Technische Universität München
Fakultät für Informatik

Diplomarbeit in Informatik

Error Classification and Propagation for Electromagnetic Tracking

Julian Much

Technische Universität München
Fakultät für Informatik

Diplomarbeit in Informatik

Error Classification and Propagation for Electromagnetic Tracking

(Fehlerklassifizierung und Fortpflanzung
für elektromagnetisches Tracking)

Julian Much

Supervisor: *Prof. Dr. Nassir Navab*

Advisors: *Dipl. Inf. Jörg Traub,*
Dr. Marco Feuerstein

Submission Date: *January 14, 2008*

I assure the single handed composition of this diploma thesis only supported by declared resources.

München, 14. Januar 2008 *Julian Much*

Acknowledgements

This work would not have been possible without the help, support and advices of my supervisors, colleagues, friends and family. Therefore, I want to say thank you to all people who supported me during writing this thesis:

First, I would like to thank Professor Navab for giving me the opportunity to work at the chair for computer aided medical procedures and augmented reality. My interest in the field of medical computer science is founded on the lectures, the research and the projects offered at this chair. A very big thank goes to my supervisors Jörg Traub and Marco Feuerstein. They did a perfect job at supporting me during the work on this thesis and answered all my questions with both patience and expertise. Furthermore, Jörg spent a lot of time at proof-reading and correcting this thesis even during his holidays. I would like to thank my colleagues at the CAMPAR chair, the MITI group and the complete IFL team: Thomas Wendler, Tobias Lasser, Alexander Hartl, Tassilo Klein, Armin Schneider, Adam Fiolka, Josef Ehrensberger and all the other persons I have met during the daily work at Klinkum Rechts der Isar. Additionally, the previous diploma or master theses written by Sukhbansbir Kaur, Claudia Thormann, Tobias Reichl and Tassilo Klein influenced this work and were a great guidance at developing this diploma thesis.

Horst Süggel, Roland Gruber and Mauritius Much did an excellent job at proof-reading this thesis and they helped a lot to improve the result. Finally, I want to say a very big thank to my family for the support during the years at university and especially at the work on this thesis.

Thank you very much!!!

Abstract

The negative influence of electromagnetic tracking errors on the accuracy of a number of image-guided surgery applications encourages the consideration of erroneous measurements on a lower level. An error classification methodology is described in this thesis and allows to group occurring errors into subclasses, to draw conclusions about their origins, and to propagate them for the prediction of the final error in the application. Positional and orientational errors can be classified into both static and dynamic distorted data, where static errors are grouped into jitter and field distortions caused by the influence of nearby metallic objects in the operating volume. Dynamic errors are subdivided into sensor velocity and errors caused by dynamically induced metals or electrical devices in the tracking area. Error propagation models help to predict the resulting error based on the initially reported tracking errors in a specific application.

Robotic devices, measurement tools and optical tracking systems can be used to classify an occuring electromagnetic error and to measure the magnitude of its components. To compensate the faulty tracking data, a number of error correction approaches can be applied and are described in this thesis. Several experiments were accomplished to classify occuring tracking errors in a distortion-free environment by using both a standardized assessment protocol with a high-precision measurement plate and a co-calibrated magneto-optical system. In general the flat transmitter showed an increased performance at orientation determination and metallic distortion experiments in comparision to the mid-range transmitter, however, with drawbacks at jitter errors and positional determinations. Furthermore, the error value provided by Ascension was observed throughout the experiments and its magnitude strongly depends on the distance between receiver and transmitter. The implemented applications of electromagnetic tracking systems in the field of navigated bronchoscopy and augmented camera systems were used to apply the error detection and correction models within this thesis. Additionally, the assessment experiments were performed in the bronchoscopy room and distortions were observed caused by metallic objects in the operating volume.

Zusammenfassung

Der negative Einfluss von elektromagnetischen Trackingfehlern auf die Genauigkeit einer Vielzahl von bildbasierten Navigationssystemen erfordert eine Betrachtung dieser fehlerhaften Messungen auf einer niedrigeren Ebene. Eine Methodik zur Fehlerklassifizierung wird in dieser Arbeit beschrieben, die es erlaubt die auftretenden Fehler in Unterklassen einzuteilen, Rückschlüsse über deren Entstehung zu ziehen und die Fehlerfortpflanzung bis hin zur Anwendung vorherzusagen. Unterteilen kann man Positions- und Orientierungsfehler in sowohl statische als auch dynamische Fehler, wobei statische Fehler weiter klassifiziert werden können in Jitter sowie Feldstörungen verursacht durch metallische Objekte im Messbereich. Dynamische Fehler hingegen werden gruppiert in Sensorenbewegungen und Fehler hervorgerufen durch dynamisch ins Trackingvolumen eingebrachte Metalle oder elektrische Geräte. Spezielle Fehlerfortpflanzungsmodelle können helfen, den sich ergebenden Applikationsfehler, basierend auf den anfänglich gegebenen Trackingfehlern, vorauszuberechnen.

Robotergesteuerte Systeme, Messwerkzeuge und optische Trackinggeräte können verwendet werden, um den auftretenden elektromagnetischen Trackingfehler zu klassifizieren und die Fehlerkomponenten zu messen. Um fehlerbehaftete Daten kompensieren zu können, kann eine Vielzahl von Fehlerkorrekturverfahren angewandt werden, die in dieser Arbeit zusammengefasst sind. Verschiedene Experimente wurden durchgeführt mit Hilfe sowohl eines standardisierten Messprotokolls in Verbindung mit einer Hochpräzisionsmessplatte als auch eines magneto-optischen Systems, um die Trackingfehler in einer störungsfreien Umgebung zu klassifizieren. Im Vergleich zum mid-range Feldgenerator zeigt der flat Transmitter eine verbesserte Leistung bei der Bestimmung der Orientierung und bei metallischen Gegenständen im Arbeitsbereich, jedoch mit Nachteilen beim Jitter und bei Positionsbestimmungen. Darüberhinaus wurde der Ascension Fehlerwert während den Experimenten beobachtet, der hauptsächlich von der Distanz zwischen Feldgenerator und Sensor beeinflusst wird. Die implementierten Applikationen von elektromagnetischem Tracking im Bereich der navigierten Bronchoskopie und erweiterten Kamerasystemen wurden zusätzlich betrachtet, um Fehlererkennungs- und korrekturverfahren anzuwenden. Die Messexperimente wurden zudem im Bronchoskopieraum durchgeführt, wo verschiedene Störungen verursacht durch metallische Gegenstände im Messbereich festgestellt wurden.

Contents

1 Introduction

Electromagnetic tracking systems (EMTS) are widely used in prototypes of image-guided surgery systems: They are popular in a diversity of fields e.g. in endoscopic navigation, 3D ultrasound, gene therapy, neurosurgery, bronchoscopy, cardiology or catheter tracking. However, EMTS are error-prone due to influences of metallic or electrical objects, fast sensor movements and limitations of the operating volume. Incorrect or distorted measurements will propagate through a registration procedure and can strongly affect the accuracy of the entire application. For that reason a specific classification approach is necessary to analyse the occuring error and to group it into defined subclasses. Furthermore, propagation models can give an idea of how specific applications depend on distorted outputs of EMTS.

In recent years several researchers focused on solutions for some drawbacks of EMTS in various ways: Several error detection methods are suggested in the literature based on robotic systems, high-precision tools and hybrid magneto-optical trackers. Such additives are usually applied to classify an occuring error and to measure the magnitude of distorted measurements. Error propagation techniques help to predict the accuracy of specific intra-operative navigation systems. An important technique for the future might be static and dynamic error correction methods which help to overcome the limitations of EMTS. Finally a short overview of some important applications developed by several groups in the last decade is presented in this thesis. They will likely benefit from improved error classification and propagation approaches.

The number of applications using EMTS will probably still increase in the future: The development of miniaturized electromagnetic sensors, which are now at a diameter of less than 1mm[1], the availability of larger tracking volumes and an improved accuracy (compared to early electromagnetic systems) opened the door for a couple of systems in medical environments. An error classification and propagation approach helps to analyse the errors reported by the tracking system and might influence the development of improved future systems and applications.

---

[1] Ascension Technology Corporation developed today's "smallest magnetic sensor in the world" with a diameter of 0.3mm. This 5DOF electromagnetic tracking receiver can be applied in vascular, urological or cardiac applications [5].

1.1 Electromagnetic tracking systems

Electromagnetic tracking systems are able to determine the position and orientation of a sensor (normally full six DOF[2]) relative to a transmitter in real-time. The field generator[3] consists of three orthogonal coils that are energized sequentially and creates three electromagnetic fields in each measurement cycle. Additionally, three perpendicularly aligned coils are located in each receiver which sense the pulses of the generated fields. Altogether at least nine values are acquired by a receiver in each measurement cycle and transfered to a processing unit. Raab *et al.* [63] described a basic method to compute the magnetic sensor position and orientation out of the measured signals. Recent algorithms improved the accuracy of EMTS and allow computations of the receiver alignment with variable system parameters like different turn numbers and areas of coils (see Zhigang and Kui [97]). The control unit of the EMTS determines the current position and orientation in tracking space automatically by applying such an algorithm and forwards the results to a computer connected via standard PC interfaces (e.g. USB or serial ports). Tracking data is usually provided by the systems as translation vectors $(x, y, z)^T$ for positional measurements and the orientation alternatively as rotation matrices R, euler angles[4] (α, β, γ) or quaternions (q_1, q_2, q_3, q_4).

EMTS differ in excitation frequency, max. number of emitter and receiver coils, arrangement of coil sets and creation of the electromagnetic fields. The systems can be classified into two major groups of field generation technologies: AC (alternating current) and DC (direct current) based devices [58]. The AC systems energize the transmitter coils with sinodial currents and the induced impulses are detected at passive sensor coils. The DC trackers use rectangular quasi-static square wave pulses and the currents are sensed by fluxgate receivers. Three additional passive measurements are performed in each cycle of DC based devices to detect and compensate the influence of the earth magnetic field. If metallic objects are located in the working volume of the EMTS, two major phenomena (eddy currents and ferromagnetism) can occure and will affect the system accurracy of both tracking technologies in a different way. Eddy current are induced in metals located in the tracking volume by a changing magnetic field and will appear mainly at materials with high conductivity. AC based systems are more affected by eddy currents than DC trackers, which were developed to avoid this effect. They usually do not suffer from this phenomena due to a short delay between receiver measurements. At this delay the eddy currents usually decay significantly[5]. The second phenomenon which influences the accuracy of both AC and DC

---

[2] Degree Of Freedom (DOF): The 6DOF of the receiver position and orientation can be subdived into three DOF for translation (x, y, z) and three DOF for rotation (α, β, γ).

[3] The terms field generator, transmitter and emitter are equivalent. Additionally, receiver and sensor are used synonymously in this thesis.

[4] Euler angles are usually denoted as Azimuth, Elevation and Roll.

[5] The sensing of the DC pulsed electromagnetic fields is delayed until the magnetic field is in a stable condition.

based systems is ferromagnetism. This effect is observed especially at metallic objects which produce a magnetization field depending on the material permeability and the excitation frequency of the EMTS. The problem of reducing the influence of ferromagnetism is still an important issue for both AC and DC based tracking technologies, what can be seen from the results of the experiments in this thesis (see section 6).

Advantages	**Disadvantages**
• no line of sight between transmitter and receiver necessary	• distortion caused by conductive or ferromagnetic materials and electrical devices
• relatively cheap in comparison to optical systems	• low accuracy (one order of magnitude lower than optical systems)
• convenient to use	• limited working volume: accuracy decreases with increasing transmitter/receiver distance
	• limited number of receiver

Table 1.1: A summary of several **advantages** and **disadvantages** of electromagnetic tracking systems.

There are several advantages and disadvantages (see table 1.1) of using EMTS in medical, industrial or military applications. Magnetic trackers are the only tracking technology nowadays which is able to determine the position and orientation of flexible endoscopes inside the human body because they do not depend on a line-of-sight between transmitter and receiver like optical tracking systems[6] do. They are quite cheap in comparison to vision based trackers and a minimum of time is required to prepare an EMTS in the operating room. No time-consuming preoperative trainings are necessary for surgeons or medical employees and a standard PC workstation can be used to process the tracking data.

EMTS lack of distortion caused by metallic objects and electrical devices in the operating volume. This problem is probably the most concerning drawback even in modern electromagnetic systems due to the overall presence of electrical devices (e.g. endoscopes, monitors, light sources) and metallic objects (e.g. table, surgical hammers, knives) in surgery rooms [9]. Nixon *et al.* [58] modeled the positional error Δp caused by metallic objects in the tracking volume to be proportional to $\Delta p \propto \frac{{d_{tr}}^4}{d_{tm}^3 d_{mr}^3}$ where d_{tr} denotes the distances between transmitter and receiver, d_{tm} the gap between field generator and metal and d_{mr} the displacement between metal and receiver (d_{mr}). In comparison to optical systems, the accuracy of electromagnetic measurements is at an one order of magnitude lower level[7]. Additionally, the tracking volume is usually quite small and a high accuracy is just guaranteed

---

[6] A detailed description of optical tracking systems (OTS) can be found in section 4.3.

[7] This fact explains why optical tracking systems are usually prefered in medical applications whenever a clear line-of-sight between target and tracker exists or can be established.

in this area. Several publications confirm that the accurracy in EMTS decrease significantly at an increasing distance between field generator and receiver. Nixon *et al.* [58] reported that the error of a positional measurement Δp seems to be proportional to the fourth power of the transmitter-receiver distance $\Delta p \propto d_{tr}^{4}$. Additionally, the number of simultaneously connected sensors is limited at EMTS.

In the following two different tracking systems commonly used in prototypes of medical applications are presented. Both EMTS provide receivers small enough to fit into a working channel of an endoscope (≤2mm). This fact is an essential detail for navigated endosopic systems, the target application of the here evaluated systems.

Ascension 3D Guidance^{TM}

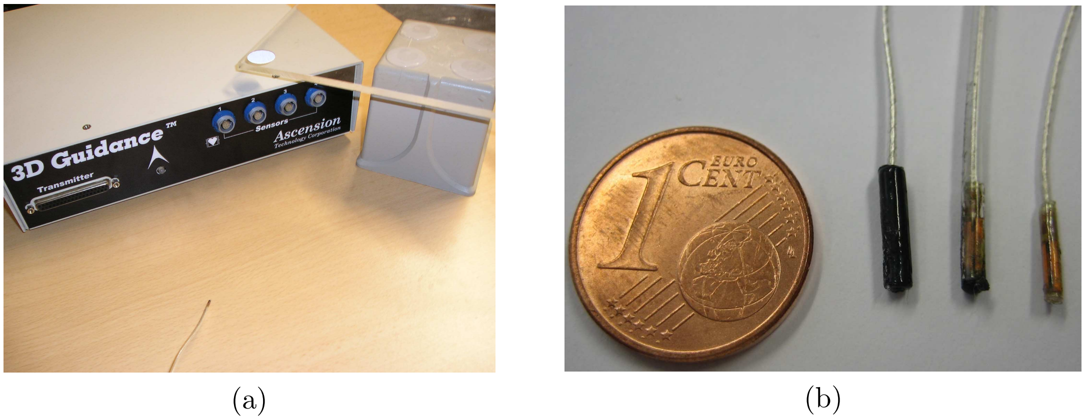
(a) (b)

Figure 1.1: The **Ascension "3D Guidance^{TM}" system** with the mid-range transmitter and the control unit, at which up to four receivers can be simultaneously connected (a). Several Ascension sensor types are shown in (b) (from left to right): model 180, model 180 (with vinyl) and model 130 (source [64]).

The direct current (DC) based "3D Guidance^{TM}" system was manufactured by Ascencion Technology Corporation[8] (see figure 1.1) [4, 3, 5] with a stated root mean square error of 1.4mm in position and 0.5° in orientation. Both a mid-range transmitter and a flat field generator which were investigated in the experiments of this thesis are pluggable to a processing unit. The flat emitter works at a frequency of 40.5Hz, whereas the mid-range field generator energizes its coils at 68.3Hz. Up to four receivers which are available in two variants with a diameter of 1.8mm (Model 180) and 1.3mm (Model 130) are simultaneously connectable to the "3D Guidence^{TM}". The specification of the working volumes with different receiver/transmitter combinations is shown in table 1.2 and can be seen in figure 1.2. The system is connected to a standard workstation PC via the USB interface

---

[8] Ascension, Burlington, VT, USA. http://ascension-tech.com/.

and addressable via linked libraries. For sterilisation and protection purpose both receiver types are available with or without vinyl isolation which allows an easy cleaning procedure in medical environments. In this thesis the "3D Guidance" system was used during all experiments with either the flat or the mid-range transmitter.

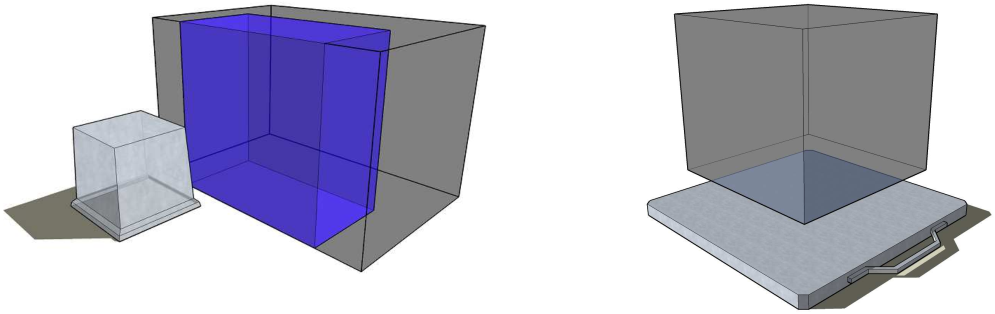
(a) (b)

Figure 1.2: **Transmitter and working volume** for different sensor types (gray-180), (blue-130) and the mid-range field generator (a) as well as the flat transmitter(b). The operating area of the flat transmitter is stated to be identical with both model 130 sensor and model 180.

Sensor	Diameter	Length	Working volume mid-range transmitter	Working volume flat transmitter
Model 180	1.8mm	6.5mm	X: 20 to 51cm Y: ±23cm Z: ±15cm	X: ±20cm Y: ±20cm Z: -10 to -46cm
Model 130	1.3mm	6.5mm	X: 20 to 36cm Y: ±15cm Z: ±15cm	X: ±20cm Y: ±20cm Z: -10 to -46cm

Table 1.2: **Technical data of the sensors**: The two types of sensors can be used with either a mid-range or a flat transmitter at the "3D Guidance" system with varying working volume specifications (source [5]).

NDI Aurora

Another commercially available tracking system is the Aurora (see figure 1.3). This EMTS is produced by NDI[9] and uses the AC tracking technology [59, 60, 61]. The tetrahedron shaped transmitter consists of six coils which generate electromagnetic fields at a frequency of 45Hz. The system is connected to a control unit via serial port (RS-232). Both 5DOF sensors and 6DOF receivers are available for the system. The 5DOF receiver is at a diameter

---

[9] Northern Digital Inc., Waterloo, Ontario, Canada. http://www.ndigital.com/.

of 0.9mm[10] and contains only one coil with 1000 windings of isolated copper wire wounded on piece of soft iron. Its orientational tracking data outputs are automatically converted by the system into quaternions with the forth element set to zero. This indicates that no rotation about the main axis of the receiver is detectable. NDI stated a system accuracy of 0.7mm for translation and 0.3° for rotational measurements. Two perpendicular arranged 5DOF sensors fixed in a plastic case form a 6DOF receiver for the system. The accuracy of the 6DOF sensor was stated with 0.9mm in position and 0.8° in orientation by NDI. Additionally, NDI offers a new Aurora system (see figure 1.3 (b)) providing full 6DOF with miniature receivers.

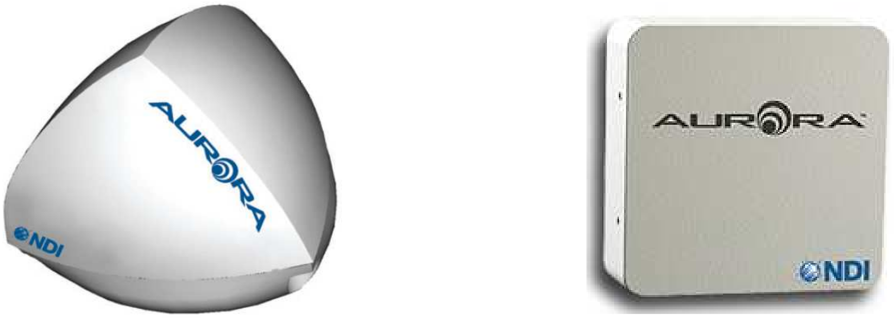

(a) (b)

Figure 1.3: The **NDI Aurora system** with the tetrahedron shaped field generator (a), which can be used with both 5DOF and 6DOF receiver. The novel 6DOF system (b) provides full 6DOF with sensor small enough to fit into a working channel of an endoscope (source [60, 61]).

1.2 Motivation

The classification of occuring errors in an EMTS is essential to understand the nature of the reported faulty data. With this knowledge it might be possible to determine the source for an erroneous measurement or to display the error components on the screen. Several researchers detected electromagnetic errors in diverse ways and classified them roughly into subcomponents. In this thesis a clear classification approach is provided based on previous publications. Detailed propagation models are rarely reported for specific applications but a short example of such an approach for the frequently used point-based registration method is presented in this thesis. Such models give an idea of how a classified electromagnetic error will propagate in the system and affects the entire application after performing a registration procedure.

---

[10] Smaller sensor types of 0.3mm are announced by NDI[61].

Furthermore, two applications based on EMTS, that suffer from the low accuracy of today's error-prone systems in the field of augmented camera systems and bronchoscopy are described. In the future reliable and errorless electromagnetic trackers might be a key technology for a number of new application areas in the field of medical navigation systems. The classification approach is a step towards improved EMTS which are able to visualize the currently occuring error. Very few propagation models were published, but they improved the knowledge of how distortion can affect a specific application after applying a registration procedure. A run-time error prediction for a specific system is possible by knowing both the magnitude of the electromagnetic error and the underlying propagation model.

1.3 Exemplary applications of improved EMTS systems

An error classification and propagation technique might help to improve the usablity of navigated bronchoscopy systems and of superimposed endoscopic applications in the future.

To superimpose endoscopic images with additional information about anatomical structures, metric properties or navigation details during a minimal invasive surgery, a camera calibration in combination with a tracking system is necessary (described in section 7.1). For that purpose electromagnetic systems can be used to track the endoscopic camera inside the human body and are crucial if the optic is attached to a flexible instrument. Such a system with an adjusted calibration pattern constructed to deal with heavily distorted visual systems was developed during the work on this thesis. These special optic cameras are quite common in endoscopic surgery, for example at flexible bronchoscopes.

Navigated bronchoscopy systems (described in section 7.2) usually rely on electromagnetic tracking to determine the position and orientation of non-rigid endoscopes inside the human lung. In this area the use of optical tracking systems is rather meaningless because medical instruments inside the human lung cannot be detected by cameras from outside the body. Several experiments were accomplished to examine the negative influence of metallic objects in the bronchoscopy room on the accuracy of the navigation system.

2 Related Work

Several reasearches published experimental results and assessment protocols for different EMTS in recent years. In this chapter a short overview is presented with related references of electromagnetic error evaluation.

2.1 Static and dynamic error evaluation

Three different error detection methods were described by Frantz *et al.* [26]. A robotic system in combination with an optical tracking system, a redundancy based tool and a hemispherical device (see figure 2.1 (top)) are suggested to evaluate the accuracy of EMTS.

Hummel *et al.* [32, 33] published a reproducible assessment protocol in combination with a precisely manufactured measurement plate (see section 4.2.2) to evaluate miniature EMTS. The Ascension MicroBird, NDI Aurora and the 6DOF Aurora system were investigated. The same protocol was reused for the experiments in this thesis to guarantee comparabilty to the results of Hummel *et al.* [32, 33].

Nafis *et al.* [54] estimated the static performance of EMTS by using a high precision robotic system. The dynamic tracking accuracy was evaluated using a T-shaped granite block (see figure 2.1 (middle)) and a redundancy based detection method.

Schneider and Stevens [68] used a robotic system to evaluate the Ascension "3D Guidance" system for static accuracy. The dynamic errors were analysed by using a redundancy based approach and by rotating the sensor at well-defined circles with the robot.

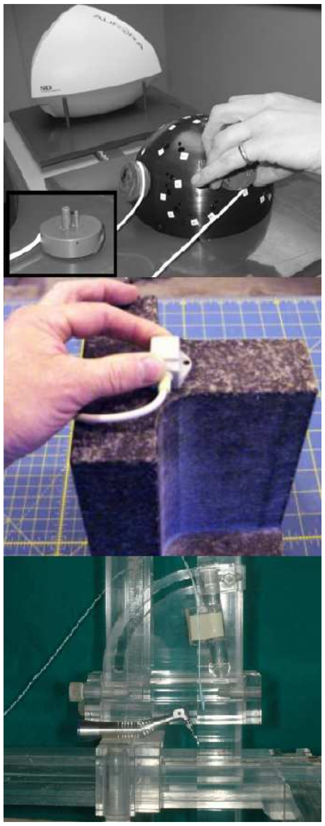

Figure 2.1: source [26, 54, 66]

2.2 Metallic distortion evaluation

Nixon *et al.* [58] accomplished several experiments to investigate the effect of metallic objects and electrical devices in the tracking volume. Additionally, theoretical models which allow to draw conclusions about the negative influence of metallic distortions and the distribution of positional errors in relation to the transmitter/receiver distance were proposed.

Birkfellner *et al.* [9] accomplished several experiments to examine systematic distortions caused by a mulitplicity of metallic objects in a medical environment. Both an AC and DC based EMTS were evaluated at the presence of surgical tools and medical devices in the experiments by using a 6DOF measurement rack (see figure 2.1 (bottom)).

Hummel *et al.* [34] evaluated the NDI Aurora system with several objects in the tracking volume. A fluroscopy unit, an ultrasound probe, biopsy forceps, guiding wires, and other objects were placed in the tracking volume and the positional deviation was observed.

Similarly Schicho *et al.* [66] compared an Medtronic StealthStation Treon-EM and the NDI Aurora in a medical environment. An ultrasound probe, a dental drill and a Largenbeck hook were positioned in the tracking area at varying transmitter/receiver distances.

2.3 Dynamic error evaluation

The evaluation of the tracking accuracy at different levels of sensor velocity was published by Mor [47]. The NDI Aurora and the Ascension MicroBird were evaluated by using a redundancy based detection tool where two receivers are rigidly attachted to wooden non-metallic instrument. By moving the handle freely through the test environment, the error was calculated in relation to the velocity of the receivers.

Mucha *et al.* [53] also used a redundancy based measurement instrument to define a simple error compensation algorithm. A plausibility check founded on the tracking data of two EMTS receivers was defined for endoscopic sinus surgery. This method allows to sense dynamic occuring errors in the surgery room.

Feuerstein *et al.* [19] proposed an online method to detect and correct field distortions occuring during abdominal surgeries by using a magneto-optical hybrid system. Two EMTS receivers were fixed at the shaft and the flexible tip of a laparoscopic ultrasound transducer and an optical tracking target is additionally attached to the shaft. The deviation (caused by dynamically induced metallic objects) between the redundantly tracked shaft sensor poses was additionally applied to correct the EMT receiver at the tip of the transducer. Furthermore, a model-based and image-based correction technique were suggested.

3 Error Classification and Propagation

In this chapter a basic classification of electromagnetic tracking errors is described, which is applied throughout this thesis. Several publications classified the EMTS errors in a similar manner, however, differences in nomenclature and computation algorithms usually occure [32, 54, 68]. Afterwards, a propagation model which allows to predict the occuring error in specific applications is discussed.

3.1 Error classification

Electromagnetic tracking errors can be classified into two major categories [40]: Static errors remain constant over time, whereas dynamic errors are occuring during the run-time of the system. An overview of the most important classes can be seen in figure 3.1 and will be described in more detail in the following subsections. But first some basic mathematics are introduced and are applied at the computation of classified errors.

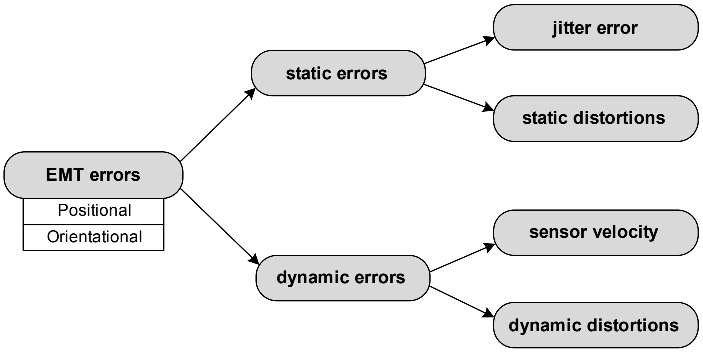

Figure 3.1: A **EMTS error classification approach**: They are grouped into both static and dynamic errors where static errors can be jitter errors and static distortions. Dynamic errors are subdivided into fast sensor movements and dynamically occuring distortions.

3.1.1 Basic mathematics

For the computation of the error components some basic mathematics are introduced to determine mean values and difference vectors of both positional and orientational measurements. Afterwards, the described formulas are applied at the determination of magnitudes of classified errors.

1. The mean location p_{mean} of a set of N recorded position data $p_i\{i = 1, ..., N\}$ can be simply found by avaraging the N position vectors:

   $$p_{mean} = \frac{1}{N}\sum_{i=1}^{N} p_i$$

2. The problem of averaging N rotations [27] is much more complicated than finding the positional mean p_{mean}. Therefore the quaternion representation of rotational measurements can be used to compute q_{mean} from a set of recorded unit quaternions Q $\{q_i \in Q \mid i = 1, ..., N\}$ with the following algorithm [38]:

   a) q_i defines the column vector representation of the i-th element of a set of unit quaternions Q.

   b) determine the $4 \times N$ matrix A, where the i-th column is q_i.

   c) compute $S = A \cdot A^T$, where S is a 4×4 matrix

   d) decompose S using a SVD[1] to determine eigenvectors e_i and eigenvalues a_i of this matrix.

   e) Now q_{mean} is defined as one (of the two) eigenvectors $\pm e_*$ which belongs to the largest eigenvalues a_*.

3. The euclidean distance d between two points $x = (x_1, x_2, x_3)^T$ and $y = (y_1, y_2, y_3)^T$ in $\mathbb{R}^3$ are defined as

   $$d(x,y) = \|x - y\|_2 = \sqrt{\sum_{i=1}^{3}(x_i - y_i)^2} = \sqrt{(x_1 - y_1)^2 + (x_2 - y_2)^2 + (x_3 - y_3)^2}.$$

---

[1] The Singular Value Decomposition (SVD) is a matrix decomposition technique which splits A into three matrices $A = UV\Sigma^*$. A detailed description to determine the results and an implementation of the SVD algorithm can be found in [62].

4. To compute the difference angle ϕ of two quaternions q_1 and q_2 in space, the rotation about the invariant Euler axis can be used:

$$\phi(q_1, q_2) = \frac{180}{\pi} \cdot arccos \left(\frac{trace\left[\bar{A}_{q_1} \bar{A}_{q_2}^{-1}\right] - 1}{2} \right)$$

where $\bar{A}_{q_1}, \bar{A}_{q_1}$ denotes the direct cosine matrices of the rotations defined by q_1 and q_2 [14].

3.1.2 Subclasses of electromagnetic tracking errors

Both static and dynamic occuring electromagnetic tracking errors can be further grouped into a number of categories. In this description the currently reported tracking position and orientation are denoted as p_{cur} and q_{cur}.

- The positional error (err_{pos}) is defined as the distance between a true location in space and the reported position of the tracking system. For the determination of the positonal error a ground trouth value p_{ref} is needed which is usually reported by a secondary tracking device[2]. Then err_{pos} can be computed with the formula

$$err_{pos}(x) = d(p_{ref}, p_{cur}) = \|p_{ref} - p_{cur}\|_2$$

- The orientational error[3] (err_{rot}) is defined as difference between a true orientation q_{ref} in space and the reported alignment q_{cur} of the tracking system. Again a ground trouth value q_{ref} is necessary to detect orientational errors which can be computed by the deviation between the reference orientation and the measured receiver alignment:

$$err_{rot}(x) = \phi(q_{ref}, q_{cur})$$

Static errors

- The jitter error[4] (err_{jitter}) describes the deviation of the electromagnetic measurements at a position x over a period of time ΔT. If the sensor is affixed at location x in space, then the reported receiver positions p_i $\{i = 1, ..., N\}$ and orientations q_i $\{i = 1, ..., N\}$ are acquired during ΔT and the differences between positional measurements are observed. At a positon x the magnitude of the jitter error can

---

[2] Several error detection devices are described in detail in section 4.

[3] The orientational error is also often denoted as rotation error.

[4] The jitter error is also sometimes denoted as “noise”.

be computed as root mean square error (RMS) from positional p_i or rotational q_i measurements. The positional and orientation jitter error can be computed by the formulas:

$$err_{posjitter}(x) = \sqrt{\frac{1}{N}\sum_{i=1}^{N} d(p_{mean}, p_i)^2}, \qquad err_{rotjitter}(x) = \sqrt{\frac{1}{N}\sum_{i=1}^{N} \phi(q_{mean}, q_i)^2}$$

The appliance of additional filters can help to reduce the occuring jitter error but usually increases the sensitivity to fast sensor movements.

- The static distortions are usually caused by metallic or electrical objects in the tracking environment. These materials have a major impact on the accuracy of EMTS [58]. Errors of millimeters or even centimeters can occure at the presence of conductive or ferromagnetic materials in the operating volume. The static positional and orientational distortion error can be computed by knowing the undistorted reference position p_{ref} and orientation q_{ref} at the formulas

  $$err_{posmetal}(x) = d(p_{ref}, p_{cur}) = \|p_{ref} - p_{cur}\|_2, \quad err_{rotmetal}(x) = \phi(q_{ref}, q_{cur})$$

  Error correction algorithms (see also section 5) can be applied to reduce the negative influence of static distortions in the tracking volume.

Dynamic errors

- The sensor velocity error[5] ($err_{velocity}$) is usually occuring at fast movements of the EMTS receiver. It is defined as the error occuring in relation to the current speed of the sensor. The current volocity is computed with $v = \frac{\Delta s}{\Delta t}$ from the observed positional changes Δs and differences in timestamps Δt of two successive tracking data outputs.

- The dynamic distortions occure due to the insertion of conductive or ferromagnetic materials or electrical powered devices in the tracking volume during run-time. The detection and (even more) correction of dynamic distortions is much harder than for static errors due to the missing ground truth or undistorted values.

---

[5] The sensor velocity error is also often denoted as speed error.

3.1.3 Additional error sources

The described and classified static and dynamic errors mainly influence the accuracy of EMTS. However, some additional impacts can also affect an output of EMTS in a negative way [4, 3]:

- A warm-up periode of approximately 5 minutes is usually recommended by the manufacturer before using the tracking system to ensure the highest available precision. After that the tracker usually shows an increased performance in terms of jitter, positional and orientational measurements.

- The measurement rate of EMTS is crucial to the overall system performance. In some applications it has to be adapted due to the influence of electronical devices working at a similar frequency as the EMTS in the operating volume. Its value is usually changable by the user via an application programming interface (API). However, the best performance in a distortion free environment is usually achieved with the default settings. Nixon *et al.* [58] investigated the effect of adapting the tracker sampling rate on distortions caused by electrically devices in the tracking area.

- Sensor proximity is another negative influence on the accuracy of EMTS. If the receivers are positioned in a small distance or even in contact to each other, then the sensor ferrite cores interact and disturb the measurement outputs.

- Damaged electromagnetic sensors are an additional source of errors. The use of miniature receivers which were developed in recent years by several manufacturers requires a careful handling of these devices. Damages of the sensors caused by heavily flexing or cracking of the receiver wires are hard to detect and a replacement of the faulty compontent is usually necessary.

- The distance between sensor and transmitter has major impact on system performance[6]. If the gap between receiver and field generator increases, then the tracking accuracy decreases.

The detection of these sources of errors is partially hard to achieve and can only be done with a careful inspection of the electromagnetic equipment. These items are usually not addressed in the classification approach because of their technical nature. However, it is recommended to check this list of errors before using an EMTS.

---

[6] This fact was already described in section 1.1 where an approximation of the error for the transmitter-receiver distance relationship based on the work of Nixon *et al.* [58] was described.

3.2 Error propagation

A special propagation model is necessary to determine the effect of an initial error reported by the tracking system on the precision of the entire application. Erroneous measurements usually influence the accuracy of a registration procedure of image-guided surgery systems and this affects the accuracy of the complete system. Unfortunately, just a few models which describe the error propagation for specific tasks in the field of medical navigation systems are proposed in literature.

A frequently used error propagation model was defined to predict the accuracy in applications using the point-based registration method[7] [46, 25, 87, 24]. This algorithm is usually applied to determine the 3D transformation between a set of points x_i $\{i = 1, ..., N\}$ to their corresponding locations y_i $\{i = 1, ..., N\}$. In a medical application the x_is are usually the fiducial positions physically measured with a tracking system and the y_is are the centroids of fiducial markers (or anatomical landmarks) extracted from CT or MRI image data.

The computation of the unknown transformation ${}^{image}\mathbf{T}_{physical}$ is usually done by iteratively minimizing the root mean square error distance between corresponding point pairs[8]. To predict the accuracy in an application using this registration method, the following error classes were defined [46] and are illustrated in figure 3.2: <u>F</u>iducial <u>L</u>ocation <u>E</u>rror (FLE), <u>F</u>iducial <u>R</u>egistration <u>E</u>rror (FRE) and <u>T</u>arget <u>R</u>egistration <u>E</u>rror (TRE).

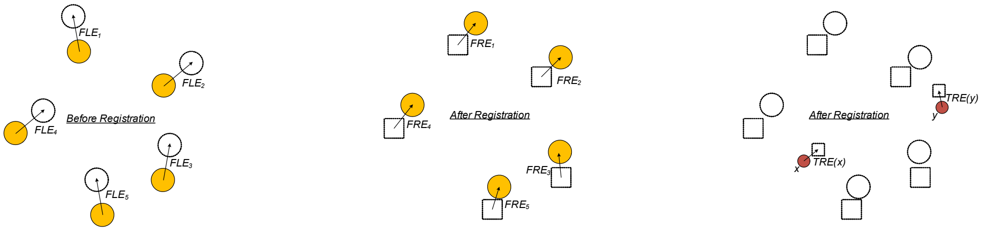

(a) (b) (c)

Figure 3.2: The errors in an application using a point-based registration procedure can be classified into **Fiducial Localization Error** (a), **Fiducial Registration Error** (b) and **Target Registration Error** (c). The FLE is the displacement between true positions (filled circles) and measured location (empty circles) of fiducials before performing the registration procedure. The FRE is the distance between measured and true fiducial positions after registration and the TRE denotes the gap between any corrosponding point pair in true space and in tracking space (except the fiducials positions) (source [24]).

---

[7] An example of an application can be found in the navigated bronchoscopy (see section 7.2.1).

[8] Mathematically the solution of the point-based registration transformation is defined as the minimum of the function $\frac{1}{N}\sum_{i=1}^{N}|Rx_i + t - y_i|$. A solution for the point-based registration problem based on dual-number quaternions was proposed by Walker *et al.* [82].

Fiducial Localization Error

The term fiducial localization error (FLE) describes the errors induced by localizing the fiducial positions in the tracking space[9] or to identify the exact centroids of markers in image space before applying the registration procedure. If an application which registers two corresponding point pairs with the point-based registration procedure acquires the registration points with an EMTS, then the FLE is mainly influenced by erroneous and inaccurate measurements of the fiducials with the tracking system. An increased value of this fault will then affect the entire system accuracy negatively.

Fiducial Registration Error

The fiducial registration error (FRE) defines the distance between corresponding marker pairs after the registration procedure. Its magnitude is usually automatically computed by the point-based registration procedure because the algorithm minimizes the FRE to find a best fitting transformation between the fiducials. Mathematically this error is defined as

$$FRE^2 = \sum_{i=1}^{N} |\mathbf{T}(p_i) - q_i|^2 = \sum_{i=1}^{N} FRE_i^2$$

with N the number of corresponding fiducials pairs $\{(p_i, q_i) \mid p_i \in P, q_i \in Q, i = \{1, ..., n\}\}$. By only considering the fiducial positions it is not possible to predict the overall system accuracy. Therefore, the FRE usually does not provide a relyable feedback of the current precision of the system. However, it provides some information about the accuracy of the matching of the fiducials in the registration procedure.

Target Registration Error

The target registration error (TRE) defines the distance of corresponding target points (except the markers) after performing the point-based registration procedure. A typical target in medical applications might be tumors, lesions or bone structures which can easily be identified in both image space and in physical space (e.g. at a phantom or the patient). The TRE is an essential reference for the accuracy of the entire application and is the only term which reflects clinical relevance. Mathematically the TRE is defined as

$$TRE = \mathbf{T}(p) - q$$

---

[9] In navigated bronchoscopy systems the localization of anatomical landmarks inside the human lung is a difficult procedure due to the deformation of human tissues, respiratory motion and the presence of metallic materials in the bronchoscope [73, 30].

where p and q are corresponding target points in physical and image coordinates and the transformation T registers p and q to each other.

Fitzpatrick *et al.* [25] derived approximations for the target registration error based on statistical analyses. These formulas can be used as a prediction of the accuracy. The expected magnitude of the TRE can be expressed as

$$\langle TRE^2(x)\rangle \approx \langle FLE^2\rangle(\frac{1}{N}+\frac{1}{K}\sum_{i=1}^{K}\sum_{i\neq j}^{K}\frac{x_i^2}{\Lambda_{ii}^2\Lambda_{jj}^2}) \qquad (3.1)$$

where Λ denotes the singular value of fiducial positions. In the three dimensional case (K=3) the above formula can be written as

$$\langle TRE^2(x)\rangle \approx \langle FLE^2\rangle\left(\frac{1}{N}+\frac{1}{3}\sum_{k=1}^{3}\frac{d_k^2}{f_k^2}\right) \qquad (3.2)$$

where $TRE(x)$ denotes the target registration error at a specific position x, d_k is the distance between the target position x and the kth principal axis and finally f_k describes the RMS distance of the fiducial positions from the kth principal axis.

Tool Design Issues

The configuration C of fiducials is an important factor for the target registration error. Therefore, the TRE can be reduced[10] by avoiding degenerated configurations, by finding optimized fiducial locations and by increasing the number of registration points. The equations 3.1 and 3.2 of the TRE can be used to find an improved design of targets or tools with attached fiducials. West *et al.* [88] summarized a set of guidelines for an optimal configuration C:

1. Avoid almost collinear fiducial marker configurations. Nearly linear alignments of the fiducials cause an increased TRE at target positions away from the line of markers. The reason for that can be seen from equation 3.2, because almost collinear placements lead to small values of the f_k term in the denominator of the formula and results in a large TRE.

2. The center of the marker configurations has to be placed as close as possible to the desired target region. The alignment of the center next to the target decreases the terms d_1, d_2 and d_3 in the nominator of equation 3.2 and leads to a reduced TRE.

---

[10] This is an important isssue at the design of surgical tools for specific applications.

3. Arrange the markers wide-spread, i.e. as far as possible away from each other. The values of the term f_k in the denominator of equation 3.2 will be increased and this results in improved TRE values.

4. Increase the number N of fiducials for the registration procedure. The TRE will be reduced due to a smaller value of the term $\frac{FLE^2}{N}$ in equation 3.2.

West and Maurer Jr. [89] discussed an optimized design for optical tracked tools in image-guided surgery systems. Additionally, the expected TRE can be predicted for the tip of the surgical instrument in relation to a coordinate reference frame (CRF). Such a situation can commonly be found in medical navigation system, where the CRF is defined by the current position and orientation of the patient[11].

Fischer *et al.* [23, 22] developed a simulator to predict the error of designed tools in EMTS environments. The time consuming tool design with different marker positions can be avoided and the expected TRE is automatically predicted by the implemented software.

Other propagation models

Bauer *et al.* [6] described an error prediction model for applications using optical tracking systems with N cameras. The error of detecting a fiducial in a camera image (image plane error - IPE) will propagate through the computation of the fiducial position in 3D (fiducial localization error FLE), during determination of the 3D target location (marker target error – MTE) and will affect the target registration error (TRE) in the application. Again the TRE can be used to predict the accuracy at a desired target location in the tracking volume, e.g. the tip position and the orientation of a rigid surgical instrument attached with retroflective markers.

The described propagation model is applicable to a number of applications using optical tracking devices, e.g. to predict errors of tracked β–probes for tumor resection (see Wendler *et al* [85]). The visualisation of the expected errors in a desired location can then be done e.g. by superimposing the real-time images with error ellipsoids at the target and fiducial positions of medical navigation systems (see Sielhorst *et al.* [71]).

---

[11] The current pose can be determined in real-time by tracking an additional sensor, optical target or fiducials fixed at the patient (see navigated bronchoscopy systems in section 7.2).

4 Error Classification Methods

4.1 Robotic systems

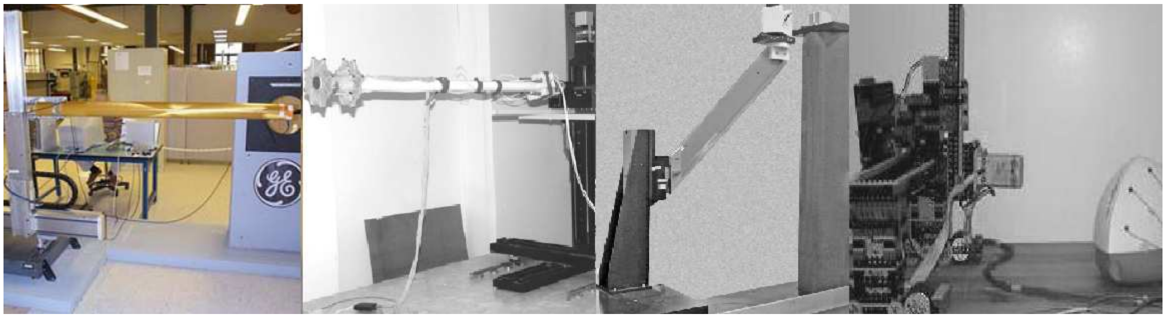

Figure 4.1: A number of **robotic systems** used by several researchers for the error detection in EMTS (source [54, 26, 68, 90]).

High-precision error evaluation and classification in EMTS can be done by applying robotic systems (see figure 4.1). Several researchers used industrial manufactured robots to place an electromagnetic receiver automatically at the desired measurement positions [26, 54, 68]. A motorized three axis-translation arm allows to move the sensor at 3DOF freely in the operating volume. Schneider *et al.* [68] additionally used a non-metallic gimbal with different receiver adapters rigidly attached to the device for orientational measurements. With this method the entire tracking volume can easily be evaluated at different positions and orientations at a very high precision level. The disadvantages of industrial manufactured robotic systems are the high cost compared to other detection methods. Additionally, robots usually consist of metal which can easily distort the electromagnetic tracking measurements. This problem can be solved by mounting the EMT receiver at a non-metallic bar rigidly attached to the robotic system. The gap between sensor and robotic device is usually bigger than the maximum dimension of the electromagnetic volume so that distortion causing materials are totally kept out of the tracking area.

Wu and Taylor prepared a small plastic Lego robot to collect a huge number of tracking data and used that information to correct static positional and orientational errors in the tracking environment [90]. Of course, these systems usually never provide a similar accurary as industrial manufactured robots but they allow to automate the error detection procedure for low-budget users. Furthermore, the accuracy can easily be increased in combination with an optical tracking system and an additional tracking target fixed at the Lego robot.

4.2 Measurement tools

The high costs and the necessary calibration procedure of robotic systems are a big drawback of such devices and usually allow only industrial manufacturers of EMTS to afford these systems. However, there were additionally simple and low budget methods published in the last decade. These techniques are very effective and can be easily used for several experiments with EMTS. Both a redundancy based approach and a manufactured non-metallic measurement plate are desribed in more detail in this section.

4.2.1 Redundancy based error detection

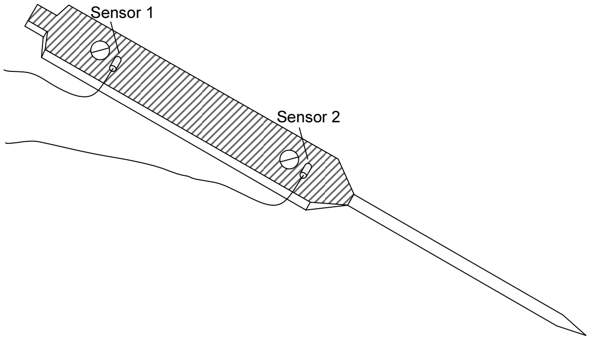

Figure 4.2: A **redundancy based tracking tool** enables the detection of dynamically occuring errors in medicial environments. Mucha *et al.* [53] used a similar pointer and observed the deviation of the tip positions computed from the reported data of both receivers.

A simple and effective method especially for the detection of dynamic errors is the redundancy based error detection technique [10, 26, 47, 53]. Two electromagnetic sensors which are rigidly attached to a non-metallic instrument are used in this approach to sense occuring errors of EMTS. Therefore, the distance between both receivers is calibrated once in a distortion free environment and serves as reference value. Assuming that a dynamic error (e.g. fast sensor movement or dynamically induced metals) affects both sensors in a different way, then the deviation of the distance between the receivers relative to the calibrated value indicates the level of distortion in the tracking system. A major advantage of the redundancy based approach is its applicabilty in medical environments: It is quite simple and cheap to mount both sensors at a non-metallic medical instrument and to define a threshold for a desired level of accuracy [10].

4.2.2 Polycarbonate measurement plate

Hummel *et al.* [32, 33] designed a polycarbonate measurement plate which was manufactured with a tolerance of 10μm in a conventional machine shop for their EMTS experiments (see figure 4.3). Its size of $550 \times 550 \times 14.7$mm enables volume analysis of EMTS in a plane and with certain dimensions. A grid of 10×10 holes was precisely drilled for positional measurements so that adjacent pairs of grid holes are 50mm away from each other.

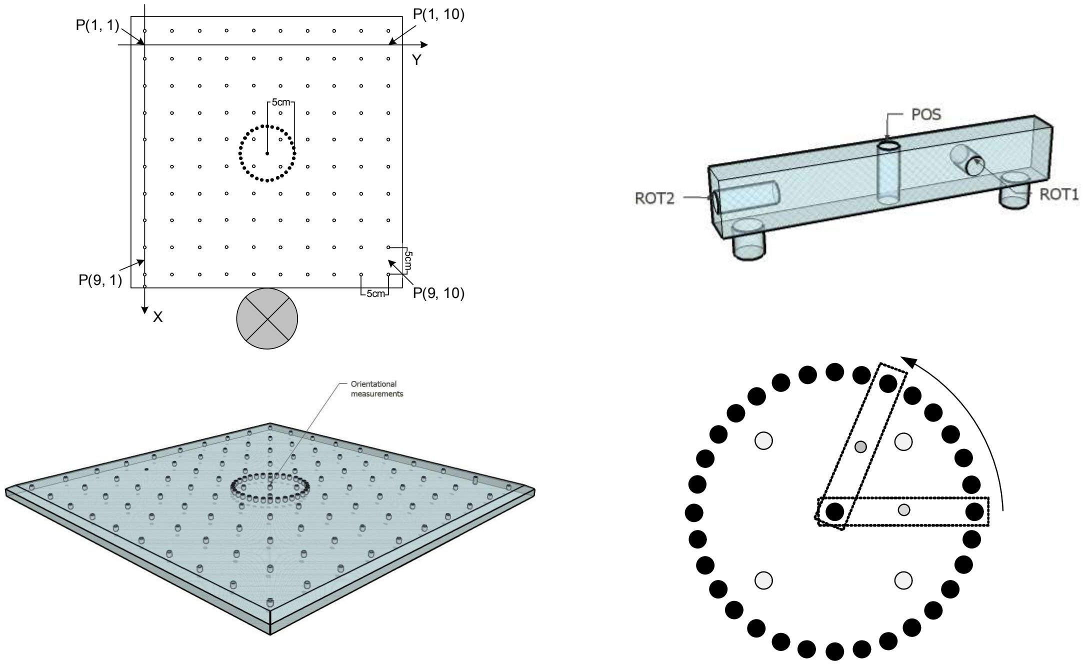

Figure 4.3: The polycarbonate **measurement plate** ($550 \times 550 \times 14.7$mm) was introduced by Hummel *et al.* [32, 33] A sensor mount can be fixed at adjacent pairs of grid holes on the plate at three receiver positions (Pos, Rot1 and Rot2). For orientational measurements a ring of 32 holes is located in the middle of the plate (∅10cm). The mount can be positioned in 11.25° steps between adjacent orientational locations (source [32, 33]).

The coordinate system of the base plate is labeled with X and Y in figure 4.3 with the origin located at the upper left corner. To ensure measurements with totally fixed EMTS receivers a sensor mount which fits into adjacent pairs of grid holes at the base plate was additionally created. The tip of an electromagnetic sensor can be rigidly attached to the mount with non-metallic screws at three possible positions (labeled with Pos, Rot1 and Rot2). For jitter and positional errors as well as detection of metallic distortions the sensor is usually fixed in Pos during data acquisition. In the center of the measurement plate a ring of holes can be used for relative orientational measurements. The sensor mount can be fixed at this sphere with a difference of 11.25° between adjacent hole pairs so that full 360°

can be accurately measured. In combination with the three attachment positions Pos, Rot1 and Rot2 of the mount the detection of rotation errors about all three main axes (α, γ, β) can be accomplished.

In the experiments of this thesis (described in section 6) the measurement plate was used for determination of jitter, positional, orientional and metallic distortion errors as well as for quality value observations. It provides a very high data acquisition accuracy and can be easily used for experiments in medical environments. A major drawback of the plate is the fact that dynamic errors (e.g. caused by fast sensor movements) are not detectable. Additionally, the acquisition procedure with replacing the sensor mount at the measurement grid is time-consuming, especially if the entire tracking volume is examined.

4.3 Magneto-optical tracking systems

A possibility to combine the advantages of vision-based and magnetic trackers is the development of hybrid magneto-optical tracking systems which can also be applied to detect erroneous measurement outputs of EMTS. In the last decade several researchers used co-calibrated devices e.g. in the field of 3D ultrasound, laparoscopic interventions or bronchoscopy [11, 56, 55, 90, 13]. Firstly, vision based tracking systems are introduced and afterwards a commonly used calibration procedure is discussed. Additionally, an optimization technique for the computed results and a temporal calibration method are described in this section.

Optical tracking systems

In contrast to EMTS the optical tracking systems provide an one order of magnitude higher accuracy in both positional and orientational estimation. This property leads us to use it as reference device for the detection of electromagnetic tracking errors. Vision based trackers are widely used in today's medical applications due to their high tracking precision [21, 78, 77, 85]. However, a major drawback of OTS is known as the line-of-sight problem, which means that a tracked object in space has to be visible for at least two cameras. The consequence of this phenomenon is that flexible endoscopes cannot be tracked by OTS inside the humen body due to the invisibility of the target markers in the camera images[1]. A schematic assembly of OTS can be seen in figure 4.4, where the cameras are aligned at a rectangluar fixture at the top of a laboratory.

---

[1] This is a big limitation especially in minimally invasive procedures where frequently non-rigid endosopic systems are used (e.g. navigated bronchoscopy in section 7.2).

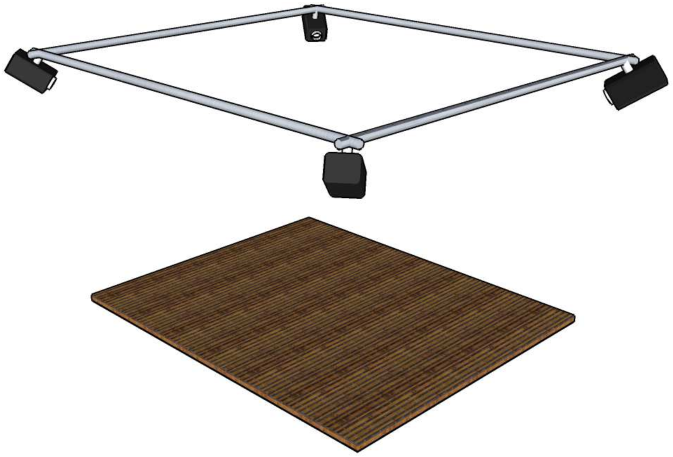

Figure 4.4: In a typical setup for **optical tracking systems** (at least two) cameras are rigidly attached at the top of the laboratory or surgery room. The redundant data segmented from the camera images can be used to determine the position and orientation of a 3D target in real-time.

An algorithm to determine the position and orientation of a number of redundant 2D information (e.g. pictures with corresponding point pairs) based on epipolar geometry can be found in Hartley and Zisserman [29]. At least two images with a minimum of 3 corresponding markers, which are visible in both pictures, are necessary to determine a position of an object in 3D.

During the experiments of this thesis a system manufactured by A.R.T.[2] was used with an reported root mean square error of 0.4mm for positional and 0.12° for orientational measurements [1, 2]. It consists of 4 infrared ARTtrack2 cameras which are rigidly fixed at the top of the laboratory. To track an object in space a special target is used containing at least 3 retroreflective markers or stickers. In each iteration of a measurement cycle the tracking cameras emit infrared flashes which are reflected by the markers and detected by the cameras. The segmented 2D marker positions from the image data are transfered to the A.R.T. tracking software running on an server computer which calculates primary all 3D marker locations and subsequently from that information the full 6DOF target translation and orientation in space. The tracking data is accessible for a couple of workstation PCs using a standard ethernet network connetion.

---

[2] Advanced Realtime Tracking GmbH, Weilheim, Germany (*http://www.ar-tracking.de*).

4.3.1 Co-calibration of magneto-optical systems

In a hybrid magneto-optical system EMTS and OTS are combined to overcome the limitations[3] of both devices. Such a system can be used to detect the errors occuring in electromagnetic tracking systems with a vision based tracker. Two additional optical targets are necessary for the calibration of hybrid trackers (see figure 4.5): the first is rigidly attached to the electromagnetic field generator and consists of non-metallic materials with visual markers on it. The second is a combined target with both optical markers and an electromagnetic receiver fixed on it.

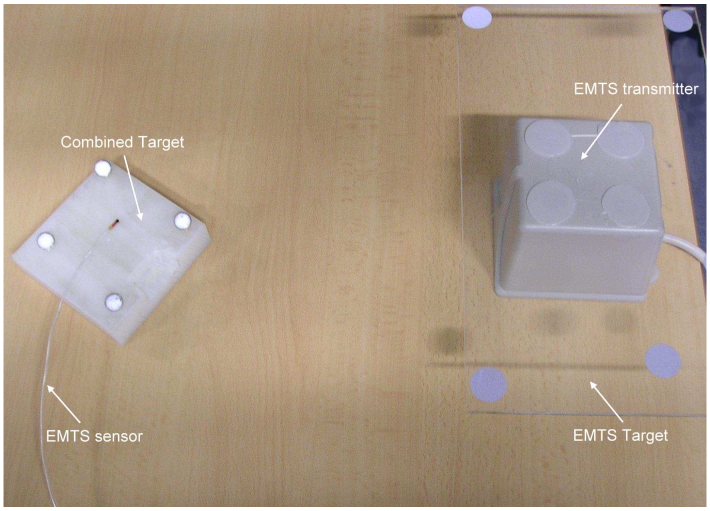

Figure 4.5: The **magneto-optical system** uses two additional tracking targets: One is fixed at the transmitter and the second is a combined target with optical markers and an electromagnetic sensor rigidly attached to each other.

Mathematically, the coordinate frames of electromagnetic and optical tracking systems have to be combined into one common world coordinate system. Several calibration procedure steps are required to achieve this aim. They have to be performed only once and can stay unchanged until the basic setup was modified by the user[4]. For a co-calibrated hybrid system two unknown static transformations which will be calculated by using a hand-eye calibration approach have to be determined (${}^{Sensor}\mathbf{T}_{CombTarget}$ and ${}^{Transmitter}\mathbf{T}_{EmtsTarget}$). It is essential to know these transformations to compare the optical tracked position p to the location reported by the EMTS $\bar{p}$. The basic setup with all involved transformations of magneto-optical systems is illustrated in figure 4.6. Afterwards, the transformations are explained in detail:

---

[3] Advantages and disadvantages of EMTS are summarized in table 1.1.

[4] The changing of the setup usually means that either the sensor at the combined target or transmitter target was repositioned.

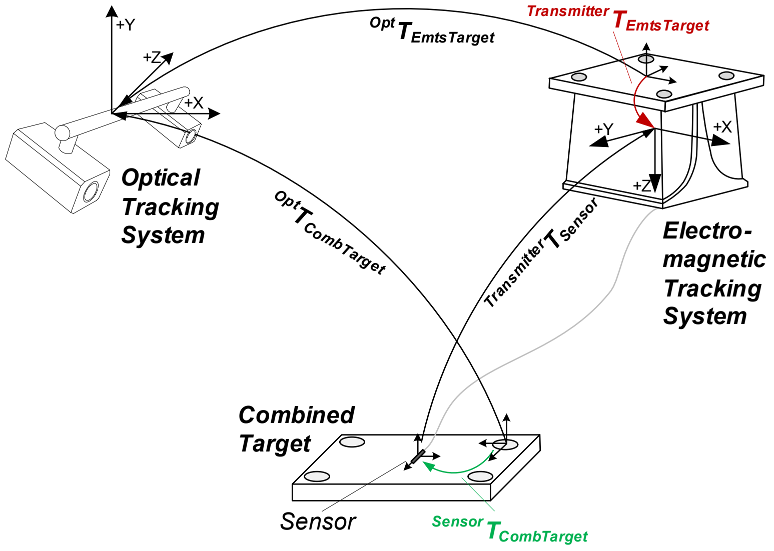

Figure 4.6: The basic setup of **magneto-optical systems** contains several transformations. The transformations from the combined target to the EMTS sensor (green) and from the EmtsTarget to the transmitter (red) are initially unknown and can be computed by the hand-eye calibration procedure. The other mappings can change dynamically in real-time and are reported by the involved tracking systems.

1. The static transformation ${}^{Sensor}\mathbf{T}_{CombTarget}$ from the combined optical target to the electromagnetic sensor is initially unknown and will be computed once using the hand-eye calibration procedure.
2. The mapping ${}^{Opt}\mathbf{T}_{CombTarget}$ from the combined target to the optical tracking origin is reported dynamically by tracking the combined target with the vision based tracker in real-time.
3. The transformation ${}^{Opt}\mathbf{T}_{EmtsTarget}$ from the target attached at the transmitter to the optical tracking origin is reported dynamically by the optical tracking system in real-time.
4. The static mapping ${}^{Transmitter}\mathbf{T}_{EmtsTarget}$ from the optical target fixed at the field generator to the EMTS origin is initially unknown and will also be computed once in the calibration procedure.
5. The transformation ${}^{Transmitter}\mathbf{T}_{Sensor}$ from the electromagnetic sensor to the field generator is provided dynamically by the EMTS in real-time.

Determination of the unknown transformations using Hand-Eye Calibration

The computation of the unknown transformations will be done by using the hand-eye calibration approach. Tsai and Lenz initially described an efficient way to compute a problem in robotic systems where a camera is rigidly attached to the robot hand[5] [81]. A similar situation is also occuring at the calibration of hybrid trackers namely for the determination of the unknown transformations ${}^{Sensor}\mathbf{T}_{CombTarget}$ and ${}^{Transmitter}\mathbf{T}_{EmtsTarget}$. Therefore it is necessary to acquire several poses k_i $(i = 1, ..., N)$ of the combined target. This is achieved by replacing this object at different positions and orientations in space. As illustrated in figure 4.7, the unknown transformations remain unchanged by the movements of the target.

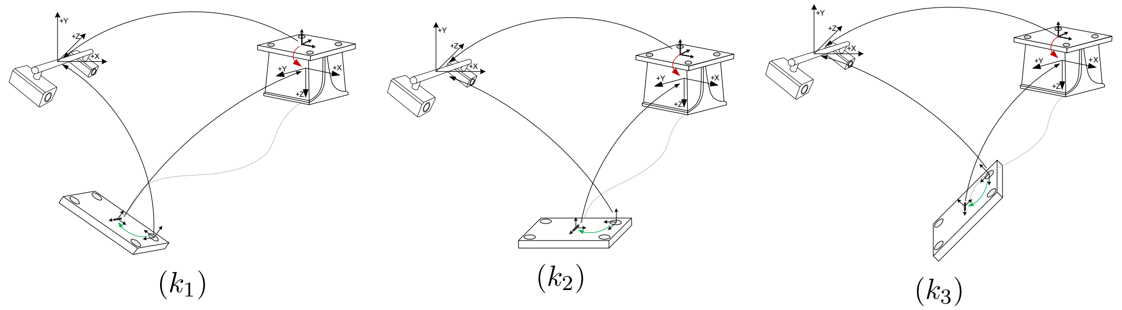

(k_1) (k_2) (k_3)

Figure 4.7: At least **three poses with the combined optical-magnetic target** are necessary to determine the unknown transformations. The redundant data can be used to compute the solution using the algorithms of Tsai and Lenz or Daniilidis.

Mathematically the motions from k_i to k_j of combined target and the electromagnetic sensor can be written as

$$\begin{aligned} \mathbf{T}_{combTarget_{k_i \to k_j}} &= ({}^{Opt}\mathbf{T}_{combTarget}(k_j))^{-1} \cdot {}^{Opt}\,\mathbf{T}_{combTarget}(k_i) \\ \mathbf{T}_{sensor_{k_i \to k_j}} &= ({}^{Transmitter}\mathbf{T}_{sensor}(k_j))^{-1} \cdot {}^{Transmitter}\,\mathbf{T}_{sensor}(k_i) \end{aligned}$$

For each movement a relation between motions and the unknown transformations can be defined by applying the basic hand-eye calibration equation $A \cdot X = X \cdot B$ where A, B denote the displacements and X is the searched transformation. Here, the hybrid tracker calibration problem can easily be adapted to the fundamental hand-eye equation:

$$\begin{aligned} A \cdot X &= X \cdot B \\ \mathbf{T}_{sensor_{k_i \to k_j}} \cdot {}^{sensor}\,\mathbf{T}_{combTarget} &= {}^{sensor}\mathbf{T}_{combTarget} \cdot \mathbf{T}_{combTarget_{k_i \to k_j}} \end{aligned}$$

---

[5] The name hand-eye calibration was taken from this problem: The transformation from the hand (i.e. the robot gripper) to the eye (i.e. the camera device) is an unknown transformation which can be determined from a number of collected camera and gripper motions.

A basic equation system can be built up by moving the combined target to several positions in space. At least three tracking data outputs of the sensor and of the optical target (i.e. two different motions of the combined target) are necessary to determine a solution. One movement from $k_i \rightarrow k_j$ provides three additional equations from which the unknown 6DOF[6] transformation ${}^{sensor}\mathbf{T}_{combTarget}$ can be computed. With more motions an overdetermined equation system can be built up. This can be solved by using the classic method of Tsai and Lenz based on a QR decomposition [81] or a technique of Daniilidis which uses dual quaternions and a singular value decomposition [15].

The computation of ${}^{Transmitter}\mathbf{T}_{EmtsTarget}$ can be done in a similar way, but now three possibilities can be used to determine the result:

1. Compute the unknown transformations by multiplications of the involved transformation:

$$
\begin{aligned}
{}^{Transmitter}\mathbf{T}_{EmtsTarget} &= {}^{Transmitter}\mathbf{T}_{Sensor} \cdot {}^{Sensor}\mathbf{T}_{CombTarget} \\
&\quad \cdot ({}^{Opt}\mathbf{T}_{CombTarget})^{-1} \cdot {}^{Opt}\mathbf{T}_{EmtsTarget}
\end{aligned}
$$

2. Determine the unknown mapping by collecting transmitter poses for a hand-eye calibration approach. The “hand” and “eye” motions are redefined as well as the hand-eye equation:

$$
\begin{aligned}
\mathbf{T}_{EmtsTarget_{k_i \rightarrow k_j}} &= ({}^{Opt}\mathbf{T}_{EmtsTarget}(k_j))^{-1} \cdot {}^{Opt}\mathbf{T}_{EmtsTarget}(k_i) \\
\mathbf{T}_{Transmitter_{k_i \rightarrow k_j}} &= {}^{Transmitter}\mathbf{T}_{sensor}(k_j) \cdot ({}^{Transmitter}\mathbf{T}_{sensor}(k_i))^{-1} \\
\mathbf{T}_{Transmitter_{k_i \rightarrow k_j}} \cdot {}^{Transmitter}\mathbf{T}_{EmtsTarget} &= {}^{Transmitter}\mathbf{T}_{EmtsTarget} \cdot \mathbf{T}_{EmtsTarget_{k_i \rightarrow k_j}}
\end{aligned}
$$

3. Reuse the poses which were acquired by moving the combined target for determining ${}^{sensor}\mathbf{T}_{combTarget}$ and perform a hand-eye calibration procedure. In this approach the transmitter position can remain unchanged. Again the “hand” and “eye” motions are redefined as follows:

$$
\begin{aligned}
\mathbf{T}_{EmtsTarget_{k_i \rightarrow k_j}} &= \left(({}^{Opt}\mathbf{T}_{CombTarget})^{-1} \cdot {}^{Opt}\mathbf{T}_{EmtsTarget}(k_i)\right)^{-1} \\
&\quad \cdot \left(({}^{Opt}\mathbf{T}_{CombTarget})^{-1} \cdot {}^{Opt}\mathbf{T}_{EmtsTarget}(k_i)\right) \\
\mathbf{T}_{Transmitter_{k_i \rightarrow k_j}} &= {}^{Transmitter}\mathbf{T}_{sensor}(k_j) \cdot ({}^{Transmitter}\mathbf{T}_{sensor}(k_i))^{-1}
\end{aligned}
$$

   The hand-eye equation is then defined in the same way in 2.

$$
\mathbf{T}_{Transmitter_{k_i \rightarrow k_j}} \cdot {}^{Transmitter}\mathbf{T}_{EmtsTarget} = {}^{Transmitter}\mathbf{T}_{EmtsTarget} \cdot \mathbf{T}_{EmtsTarget_{k_i \rightarrow k_j}}
$$

---

[6] Three unknowns belong to rotational (α, β, γ) and three to translation (x, y, z) variables.

To improve the precision and robustness of the calibration procedure, a critical selection of the recorded poses is necessary [67]. The rotation angles between motion pairs have major impact on the accuracy of the method and it is recommended to increase these orientions between the collected poses for a stable computation of the unknown transformations.

4.3.2 Optimization of the co-calibration results

The output of the hand-eye calibration procedures strongly depends on the accuracy of poses reported by the tracking systems [67]. An imprecise determination of positional and orientational data affects the calibration precision in a negative way. Therefore the estimated transformations ${}^{Sensor}\mathbf{T}_{CombTarget}$ and ${}^{EmtsTarget}\mathbf{T}_{Transmitter}$ can be optimized by using the Levenberg-Marquardt algorithm [43, 45]. Firstly, the matrix T_δ is defined in the following way:

$$T_\delta = \begin{bmatrix} R_\delta & t_\delta \\ 0 & 1 \end{bmatrix} = {}^{Sensor}\mathbf{T}_{CombTarget} \cdot {}^{CombTarget}\mathbf{T}_{Opt} \cdot {}^{Opt}\mathbf{T}_{EmtsTarget} \cdot {}^{EmtsTarget}\mathbf{T}_{Transmitter} \cdot {}^{Transmitter}\mathbf{T}_{Sensor}$$

If the reported tracking data of both optical and electromagnetic systems are assumed to be totally undistorted and the unknow matrices can be accurately determined by the calibration procedure, then T_δ would be the identity matrix. However, due to inaccurate and erroneous tracking or calbration outputs this will usually never be the case. Feuerstein *et al.* [19, 20] used T_δ in a cost function for optimizing the previously computed results:

$$\delta = \delta_{trans} + 3 \cdot \delta_{rot} = \underbrace{||t_\delta||}_{\delta_{trans}} + 3 \cdot \underbrace{\frac{180}{\pi} \cdot arccos(\frac{trace(R_\delta) - 1}{2})}_{\delta_{rot}}$$

The function δ weights positional to orientational errors with 1:3 corresponding to the relationship between translation and rotational root mean square error of optical and electromagnetic systems. The Levenberg-Marquardt algorithm can now be applied using the estimated martices from the previous hand-eye calibration procedures as initial parameters. The optimized transformations ${}^{Sensor}\mathbf{T}_{CombTarget}$ and ${}^{EmtsTarget}\mathbf{T}_{Transmitter}$ are computed iteratively by minimizing the cost function δ.

4.3.3 Temporal Calibration

After spatial calibration of magneto-opical hybrid tracking systems it is essential to additionally perform a temporal registration due to a short time delay occuring between reported measurements of the co-calibrated trackers [55, 79]. To synchronise the optical system with a workstation PC, the CAMPAR framework provides a solution to adapt the optical system to a computer based on the NTP[7] protocol [72]. However, the task to synchronise the electromagnetic tracking systems with the computer is a non-trivial issue because the EMTS do not provide a reliable timestamp at the moment of data acquisition. The necessary temporal information is added manually at the host PC in the moment of incomming data at the system. The procedure of determining this short time delay between moment of data acquisition at the tracking system and the processing of the measurement on the client computer is known as temporal calibration procedure.

In the calibration process the combined optical and electromagnetic target (described in the previous section) is moved up and down, while both electromagnetic and optical tracking data are acquired. The recorded data is transformed into 2D (time vs. 1D translation) by using a principal component analysis. An optimization can be performed to find the best fitting translation of the time axis to match both curves. The optimal Δt is the unknown temporal offset between optical and electromagnetic tracking data and can be computed by using the Levenberg-Marquardt algorithm [43, 45].

4.4 Initial experiments of EMTS errors and quality values

At the beginning of the work on this thesis a basic software interface was implemented to group EMTS errors into the described subclasses and to examine the significance of the reported quality values in relation to the classified error (see figure 4.8). A standard workstation PC was used running Windows XP and the optical tracker as well as the Ascension "3D Guidance^{TM}" EMTS were connected via ethernet and via USB interface. The software for the EMTS error evaluation and classification was written in C++ using the CAMPAR framework[8], which provides support for combining different kind of tracking devices, synchronisation of the data at the host computer and running high resulution graphic applications.

A hybrid magneto-optical tracking system was implemented in this software to provide the reliable ground truth data. A spatial calibration, a temporal registration and the optimization using the Levenberg-Marquardt algorithm was realised based on the mathematical models described previously in this section. All necessary calibration steps can be selected at the graphical user interface and the currently occuring error is classified and visualized in a number of different plots at the main window. Advanced third party software (OpenGL, QT or OpenCV) was used for 3D and 2D visualization, graphical user interface design and image processing. Additionally, a second tracking sensor was rigidly attached to the

---

[7] Network Time Protocol.

[8] The CAMPAR framework was developed at the chair for computer aided medical procedures and was described by Sielhorst *et al.* [72].

combined target of the hybrid system to evaluate the redundancy based detection method.

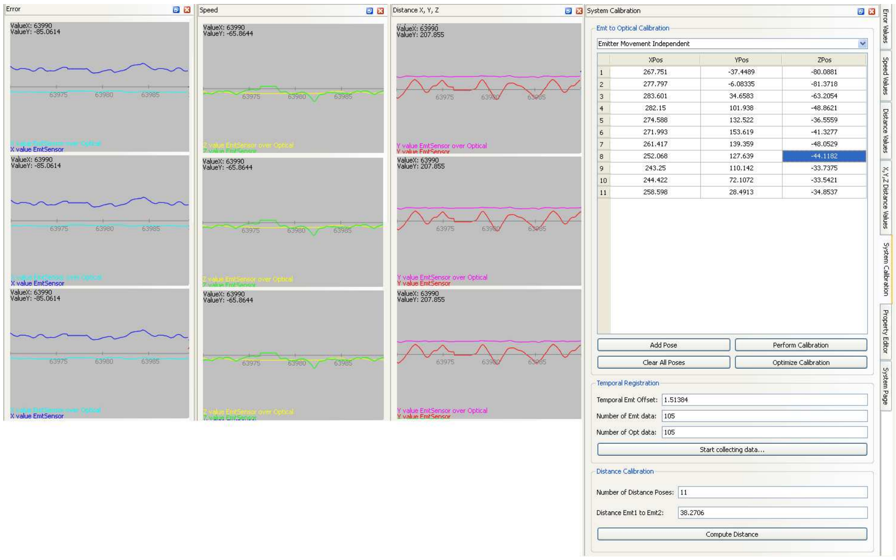

Emt to Optical Calibration

Emitter Movement Independent

	XPos	YPos	ZPos
1	267.751	-37.4489	-80.0881
2	277.797	-6.08335	-81.3718
3	283.601	34.6583	-63.2054
4	282.15	101.938	-48.8621
5	274.588	132.522	-36.5559
6	271.993	153.619	-41.3277
7	261.417	139.359	-48.0529
8	252.068	127.639	-44.1182
9	243.25	110.142	-33.7375
10	244.422	72.1072	-33.5421
11	258.598	28.4913	-34.8537

Temporal Registration

Temporal Emt Offset: 1.51384
Number of Emt data: 105
Number of Opt data: 105

Distance Calibration

Number of Distance Poses: 11
Distance Emt1 to Emt2: 38.2706

Figure 4.8: The **user interface of the implemented software** for the initial experiments to examine occuring errors in EMTS and to investigate the Ascension quality value. A hybrid magneto-optical system was built up to provide the reliable ground truth data.

The system clearly shows that distortions caused by dynamic errors can easily be detected by the redundancy based detection approach. The quality value of Ascension was not a reliable indicator for the system accuracy during these experiments and its magnitude seems mainly to depend on the receiver/transmitter distance. Especially metallic distortions and dynamic occuring errors are not displayed adequately by the provided Ascension quality value.

5 Error Correction Techniques

The presence of nearby metallic objects or electrical devices influences the accuracy of the electromagnetic tracking data in a negative way [58]. However, in many cases it is not possible to take the distortion causing objects out of the tracking volume or to reposition the electromagnetic transmitter. In a common surgery room endoscopes, OP table, monitors or surgical instruments are non-removeable and indispensible objects which strongly distort the field generated by an EMTS. Several groups of researchers measured distortions caused by such metallic objects in medical environments [8, 9, 34]. For static distorted fields (see figure 5.1) a couple of algorithms can be applied to compensate erroneous measurements in the operating volume of EMTS.

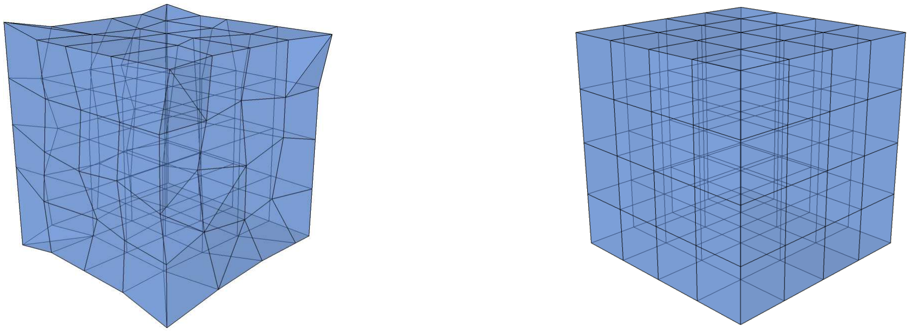

Figure 5.1: A **static distorted tracking volume** (left) can be compensated (right) by applying an error correction technique. To undistort the reported measurements a function f is computed from a number of acquired corresponding point pairs (p_i, q_i).

An overview about static error correction techniques was published by Kindratenko[1] [40]. In each approach an additional data acquisition procedure is necessary to compensate the erroneous measurements. This is usually accomplished by applying a secondary tracking device or measurement tool[2] providing a reliable ground truth data. In this section some of these static error correction techniques are reviewed and a short overview about some possible compensation approaches for dynamically distorted environments is given.

---

[1] Kindratenko released the summary of error correction methods in 2000. A couple of new algorithms was suggested by several researchers since that time especially for the rectification of orientational measurements [90, 28].

[2] Several error detection methods described in the previous section can be used (e.g. optical systems or robotic systems).

5.1 Static error correction

The common procedure to correct static errors in electromagnetic tracking systems is to record a set of (distorted) measurements and the corresponding (undistorted) reference data with an additional tracking system or measurement tool. In medical environments this is usually done before a clinical intervention in the operating room and the setup remains unchanged until the alignment of distortion causing objects or the electromagnetic transmitter are repositioned. After the data acquisition procedure the secondary tracking device can be removed from the surgery room. The process of compensating erroneous electromagnetic tracking data in static distorted environments is a 3 steps procedure:

1. Collect N corresponding point pairs (p_i, q_i) of measured electromagnetic tracking positions $\{p_i \in P \mid i = 1, ..., N\}$ and (undistorted) true locations $\{q_i \in Q \mid i = 1, ..., N\}$ detected by the secondary tracking device.

2. Determine function f based on the acquired data from the previous step. Several approaches are presented in this section to compute f.

3. Apply f at each reported electromagnetic tracking data in real-time (i.e. compute $f(p_{cur})$) and return the corrected position q_{cur}.

Mathematically the computation of the error function f can be seen as a 3D interpolation problem. Assuming that the position of the transmitter is fixed in space and the distortions remains unchanged during the process, then a mapping $f : P \to Q$ from distorted tracking space $P \subset \mathbb{R}^3$ to the distortion free space $Q \subset \mathbb{R}^3$ is searched. All reported tracking data $p \in P$ in the working volume of the EMTS has to be transformed to its corrected values $q \in Q$, where $f(p_i) = q_i$, $\forall i = 1, ..., N$. This function f should be at least C^1 continuous to provide a smooth interpolation mapping without oscillations. After determining f each reported tracking position $p_{cur} \in P$ can be mapped to its corrected position q_{cur} by computing $f(p_{cur}) = q_{cur}$.

The static error correction techniques can be classified into local and global methods: Local approaches subdive the working volume into a couple of small areas and define an unique mapping for each subregion. In contrast to that global techniques provide one common function for the entire tracking volume. A major drawback of the following static error correction approaches is the fact that the data acquisition procedure has to be repeated if the location of the field generator was modified or the spatial alignment of the distortion causing equipment was replaced or removed. Additionally, the collection of pairs of corresponding data is time-consuming and requires an additional tracking device, robotic system or high-precision measurement tools. However, very good results can be achieved by using the following error compensation techniques.

Tri-linear interpolation

The tri-linear interpolation [44] belongs to the group of local error correction techniques which subdivides the true space into j non-intersection cubic volumes. It is necessary to place the EMT sensor at eight positions $\{p_1, ..., p_8\}$ in the tracked space which defines such a regularly spaced cube and to know additionally the corresponding undistorted coordinates $\{q_1, ..., q_8\}$ of the cube vertices in true space. Then the corrected coordinates q of an arbitrary tracking position p inside this cube can be determined by using the tri-linear interpolation formula

$$\begin{aligned} q = f(p) &= (1-t)(1-u)(1-w)q_1 + t(1-u)(1-w)q_2 \\ &\quad + tu(1-w)q_3 + (1-t)u(1-w)q_4 \\ &\quad + (1-t)(1-u)wq_5 + t(1-u)wq_6 \\ &\quad + tuwq_7 + (1-t)uwq_8 \end{aligned}$$

where $t = \frac{x^P - x_1^P}{x_2^P - x_1^P}, \qquad u = \frac{y^P - y_1^P}{y_4^P - y_1^P}, \qquad w = \frac{z^P - z_1^P}{z_5^P - z_1^P}$

To correct a distorted location of an arbitrary position p_{cur} in the entire electromagnetic tracking volume, it is essential to determine the 8 vertices $\{p_i\}_j$ $(i = 1, ..., 8)$ of the surrounding cube j $(j = 1, ..., m)$ of p_{cur}. Therefore, the receiver has to be positioned at all grid vertices in true space during the data acquisition process. Frequently a lookup table is used to find the surrounding vertices $\{p_i\}_j$ of a reported tracking position p_{cur} and to store the corresponding pairs of distorted and corrected grid positions. By substituting the 8 neighboring vertex locations and the reported tracking position p_{cur} at the tri-linear interpolation formula, the undistorted location q_{cur} of any tracked point p_{cur} can be computed in the working volume.

The tri-linear interpolation technique provides C^1 continuous tracking inside each recorded cube. However, the gradients of the interpolation function change rapidly at the border regions of intersecting cubes. This can be observed at suddenly varying positional data at such areas. Additionally, the acquisition of data in a rectangular grid in distorted tracking spaces is a non-trivial problem and is usually compensated by resampling of the data[3]. Kindratenko reported that this approach belongs to a group of so called shape functions which allows to map an arbitrary hexahedron defined by $\{p_i\}_j$ in distorted space to a cube in corrected space [40]. The correction of orientational tracking errors can not be done by using the tri-linear interpolation technique.

---

[3] The process of resampling is an additional source of error at the tri-linear interpolation technique.

Hardy's multi-quadric method

Hardy's multi-quadric method is a global error correction technique proposed by Zachmann *et al* [93, 94] and bases on the HMQ (Hardy's Multi-Quadrick) interpolation approach. For data acquisition the sensor has to be located at a rectilinear 3D grid in true space Q to measure the n vertices q_i and the corresponding position p_i of the tracked space. The HMQ interpolation function $f : \mathbb{R}^3 \rightarrow \mathbb{R}^3$ is defined as

$$q = f(p) = \sum_{j=1}^{n} \alpha_j w_j(p) \qquad p, \alpha_j \in \mathbb{R}^3$$

with basis functions $w_j(p) = \sqrt{||p - p_j||^2 + R^2} \quad (R > 0)$. To determine f it is essential to compute the unknown coefficients α_j. Therefore an equation system can be build up containing n rows with n unknowns by substituting the corresponding pairs of vertices in true space q_i and in tracked space p_i at the formula

$$\sum_{j=1}^{n} \alpha_j w_j(p_i) = q_i$$

The solution of α_i can be computed by using a LU matrix decomposition technique. The parameter R^2 is essential for a smooth interpolation function and it is recommended to set its value to $10 \leq R^2 \leq 1000$. The HMQ approach allows full C^1 continuous mapping all over the tracking space and shows very smooth interpolation behaviour even at the border regions of the cubes. Together with the following high-order polynomial fit approach, this method provides the best results of compensation of erroneous measurements in static distorted environments [40].

High-order polynomial fit

Another global error correction technique is the high-order polynomial fit method [35]. Several measurements $\{q_i\}$ at n nodes of an equal-spaced three dimensional grid in undistorted space and the corresponding positions p_i in tracked space are stored. The formula $v_i = p_i - q_i$ defines the error vector for any tracked position p_i in P. Now for an arbitrary location $p \in P$ a vector polynomial with degree r, which fits an arbitrary error vector v can be written as

$$v = f(p) = f(x, y, z) = \sum_{j=1}^{R} \begin{bmatrix} c_{xj} \\ c_{yj} \\ c_{zj} \end{bmatrix} x^{s_j} y^{t_j} z^{u_j}$$

where the number of terms of the polynomial R is $\frac{(r+1)(r+2)(r+3)}{6}$, the s_j, t_j, u_j $(0 \leq s_j + t_j + u_j \leq r)$ are positive powers with unique permutations $\{s_j, t_j, u_j\}$ and $c_{x_y}, c_{y_j}, c_{z_j}$ are the unknown coefficient of the polynomial. A solution for these unknowns is given by minimizing the function $\sum_{i=1}^{n} ||v_i - f(p_i)||^2$ which can be rearranged to the formula:

$$\sum_{j=1}^{R} \begin{bmatrix} c_{xj} \\ c_{yj} \\ c_{zj} \end{bmatrix} \sum_{i=1}^{n} (x_i^{s_j} y_i^{t_j} z_i^{u_j})(x_i^{s_k} y_i^{t_k} z_i^{u_k}) = \sum_{i=1}^{n} v_i (x_i^{s_k} y_i^{t_k} z_i^{u_k})$$
$$(k = 1, ..., R) \quad (n > R)$$

The high-order polynomial fit method provides a smooth interpolation and C^1 continuity all over the tracking space. Polynomials of 3rd or 4th order are usually used to avoid oscillations which can typically occure by using higher order functions. The method corrects large distortions very well but in regions which are almost undistorted it can induce small additional errors.

Neural networks

An alternative error correction approach with a multi-layer feed-forward neural network was described by Saleh *et al.* [65], which provides also a C^1 continuous smooth mapping all over the volume. The calibration procedure in this method is both to obtain a calibration table (training set) and to train the network until a certain accuracy level in the tracking volume is reached. This method was used for location error correction in [65], but can be straightforwardly adapted to orientational measurements. The network (see figure 5.2)

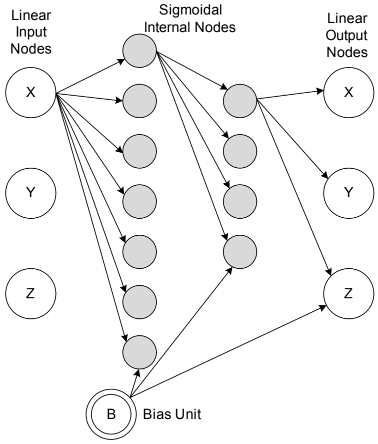

Figure 5.2: A **neural network** with 7 nodes at the first hidden layer and 4 nodes at the second layer. The input nodes represent the reported position of the sensor, the corrected location is illustrated as the output node. This design was suggested by Saleh *et al* [65] (source [65])

consists of three input and three output nodes. The input nodes represent the reported sensor position in the tracking volume and the output nodes depict the corresponding corrected location. Two hidden layers are placed between them, whereas each node in the first layer is connected to each node in the second layer. Saleh *et al.* [65] used $f(s) = s$ as linear activation function for external nodes (input and output nodes) and $f(s) = \frac{1}{1+e^{-s}}$ as sigmoidal activation function for internal neural network nodes. Additionally, a bias unit is connected to every internal and output node in the network. For training the network a standard backprojection algorithm is used until the desired level of accuracy is reached. A number of parameters which are crucial for the accuracy of the system has to be adapted. If the iterative network training is finished, the results can be used to correct reported sensor positions in a distorted environment.

A major drawback of this approch is the time consuming training which is necessary to reach specified accuracy requirements. The parameters of the network have to be adapted carefully to provide acceptable output values. Additionally, the quality of the compensating erroneous data is similar to other methods (e.g. to Hardy's multi-quadric method or high-order polynomial fit) [40].

Comparision of techniques

Most of the techniques described in the previous sections can be additionally used to correct orientational errors in distorted environments. For the correction of rotational errors a huge number of data has to be acquired and this proceeding is hardly applicable by a manual data collection. The details about some fundamental differences of the introduced methods are summarized in table 5.1.

Traub *et al.* [39, 76, 74] compared two different error correction methods to eliminate the electromagnetic field distortion caused by a metallic gantry in the radiation therapy room. Both a local approach based on tri-linear interpolation and a global method using Hardy's multi-quadric interpolation were applied to undistort the measurements reported by the tracking system. The data acquisition was done by moving a non-metallic block in a rectilinear grid in true space. In the case of the tri-linear interpolation this data was resampled to create an equal-spaced room in tracked space. The results demonstrate the major improvements which can be achieved by applying error correction techniques in a distorted environment: the tri-linear interpolation approach corrected 89.9% and Hardy's multi-quadric methods even 97.2% of tracked positions in the radiation therapy room. The global error function shows better performance in terms of accuracy and provides smoother interpolation of data. The mean error in the entire heavily distorted tracking volume was reduced from 50.5mm before applying an correction method to 5.0mm with the local approach and 1.4mm with Hardy's multi-quadric method.

Method	**Overall location error correction quality**	**Overall orientation error correction quality**	**Advantages (⊕) and Disadvantages (⊖)**
Tri-linear interpolation	average	——	⊖ topology limitations ⊖ discontinuity in gradients
Hardy's multi-multi-quadric interpolation	best	best	⊕ smooth continuous mapping ⊕ unstructured grid can be used
High-order polynomial fit	best	best	⊖ occasional increase in error value when the initial error is small ⊕ smooth continuous mapping ⊕ unstructured grid can be used
Neural network	fair	possible	⊖ network params not well defined ⊖ time consuming training required ⊕ smooth continuous mapping ⊕ unstructured grid can be used

Table 5.1: Comparison of different **static error correction techniques** which are described in this chapter. The best performance was observed by applying the high-order polynomial fit method and Hardy's multi-quadric approach. Both can also be adapted to correct orientational errors [40].

5.2 Dynamic error correction

Only a few techniques for compensation of dynamically distorted environments are reported in the literature. Feuerstein *et al.* [19, 64, 20] proposed some error detection and correction methods for dynamic errors in the field of laparoscopic ultrasound. Two EMTS sensors were attached to the shaft and the flexible tip of a laparascopic ultrasound transducer and an additional optical target was fixed at the shaft. A magneto-optical co-calibrated system was used for automatic detection of distortions at the redundantly tracked shaft sensor. Three different error correction techniques are suggested to correct the distorted tip values if the deviation of the computed shaft sensor positions was higher than a specific threshold:

1. Redundancy based error correction: The reported pose of the shaft sensor was compared to its ground truth position and orientation provided by the co-calibrated system and the correction of the shaft receiver was additionally applied to the sensor at the tip of the transducer.
2. Model based error correction: The movements of the flexible transducer tip were modeled by a special function of two parameters. The deviation of the reported tip

sensor pose to the computed model position was used to correct the distorted receiver position.

3. Image based error correction: The error compensation was done by segmenting the true transducer tip position at real-time images of an endoscope and processing this information to correct the erroneous data.

Feuerstein *et al.* [19, 64, 20] reported that the best results were observed by combining the model and image based correction. Additionally, the model based approach performed better than the redundancy based.

6 Experiments

In these experiments the analysis of jitter, positional or orientational errors and distortion caused by metallic objects in the electromagnetic tracking volume was accomplished with a standardized assessment protocol published by Hummel *et al.* [32, 33]. The same machined polycarbonate measurement plate which was described in more detail in section 4.2.2 for error detection and classification was used. This proceeding assures both reproducibility for the experiments described in this chapter and comparability to the previous results of Hummel *et al* [32, 33] where both NDI Aurora, Ascension MicroBIRD and a novel Aurora 6DOF were evaluated with same method.

6.1 Introduction

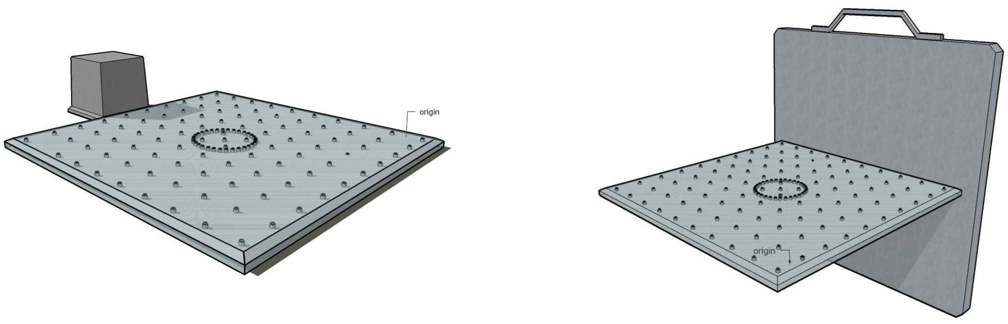

Figure 6.1: The **experimental setup**: both electromagnetic tracking systems were placed next to the polycarbonate plate in a distortion free environment. The flat transmitter (right) was fixed perpendicular to ensure comparability of the systems.

The experiments in this thesis were accomplished with the "3D Guidance" system manufactured by Ascension with both the mid-range and flat transmitter and in combination with two different sensor types of diameter 1.8mm and 1.3mm[1]. The polycarbonate plate and the field generator were rigidly attached to a wooden, non-metallic table in the laboratory. The experimental volume was totally free of metallic objects which can influence

---

[1] Technical details of tracking volume specification for different receiver/transmitter combinations and a description of the "3D Guidance" system can be found in section 1.1.

the results negatively [58, 9]. In the experimental setup (see figure 6.1 and 6.2) the mid-range transmitter was positioned centered at an edge of the measurement plate. To ensure comparability between both systems the flat emitter was placed at the same location but perpendicular aligned to the polycarbonate plate because all corresponding grid positions in both experimental setups should have a similar distance from the field generator.

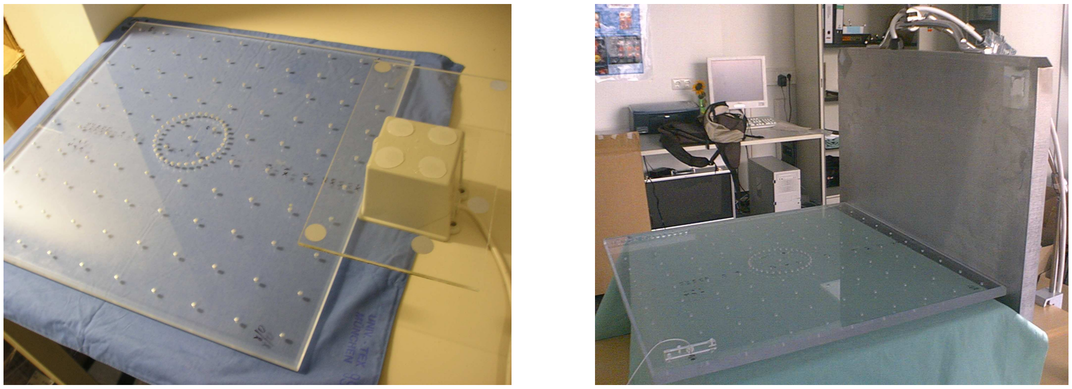
(a) (b)

Figure 6.2: The **experimental setup** for the plate experiments with the mid-range transmitter (a) and flat transmitter (b). The operating volume was totally free of distortion causing materials like metallic objects or electrical devices.

6.2 Methods

During all the experiments the sensor tip was fixed at the mount and located at the currently desired measurement position on the polycarbonate base plate. The receiver was attached to “Pos” location of the sensor mount for jitter error, metallic distortion, quality value and positional measurements. For determination of orientational errors all three positions (Pos, Rot1, Rot2) are needed due to the evaluation of rotations about all three main axes. The computation of errors in these experiments was done by using the following methodology[2]:

- For jitter error determination the sensor was fixed at all grid positions of the base plate and a 10 second continuous data stream was recorded at each location x. The positional jitter at each location x was computed as RMS from positional p_i $\{i = 1, ..., N\}$ measurements:

$$err_{posjitter}(x) = \sqrt{\frac{1}{N}\sum_{i=1}^{N} d(p_{mean}, p_i)^2}$$

---

[2] The mathematical backgrounds are described in detail in section 3.1.1.

- For positional error determination the mean position data was computed from a 10 second tracking data stream at all grid positions of the measurement plate. The distance between adjacent pairs of sensor locations were now compared to the corresponding physical spaces provided by the metrics of the measurement plate. For mean relative position error measurements all possible distances of 50mm (100mm, 150mm, ..., 400mm) between the recorded receiver placements were computed. Additionally, the positional data was evaluated as cumulative row distance error to observe the positional error distribution at the grid. Therefore, the distances between the first position in each row $P(1, i)$ $\{i = 1, ..., 9\}$ and the other locations in each row $P(i, j)$ $\{j = 2, ..., 10\}$ were computed.

- For computation of rotational errors again a 10 second data stream was recorded at each orientational measurement location around 360° with the sensor fixed in Pos, Rot1 and Rot2 position at the mount. The stored quaternions were averaged and compared to the known rotation angle of 11.25° between pairs of adjacent measurement positions.

- The metallic distortions were computed by fixing the sensor at a distance of 36cm away from the transmitter. Now the reference position p_{ref} of the sensor is recorded without any distortion causing material in the tracking volume. Afterwards, metallic rods (12.7mm×50mm) made of aluminium, bronze, SST[3] 303 and SST 416 were placed at several well-defined locations between sensor and transmitter. The metallic distortion at position x was determined by the deviation between reference value p_{ref} and the current positional measurement p_{cur}:

$$err_{metal}(x) = d(p_{ref}, p_{cur}) = \|p_{ref} - p_{cur}\|_2$$

- For quality value determination the Ascension quality number was investigated. It indicates disturbing influences at the current measurements. Crucial to this output are specific parameters which can be adapted by changing the default settings at the application programming interface. The reported value is computed by the system using the formula

$$QualityNumber = Sensitivity \times (ErrorSystem - (Offset + Slope \times Range))$$

  Slope, Offset and Sensitivity are adaptable parameters at the API, whereas Range and ErrorSystem are unchangeable values provided by the tracking system [4]. In these

---

[3] stainless steel.

experiments the distribution of Ascensions quality number was tested in a distortion free environment by using the measurement plate. All quality parameters remain at default settings which are loaded automatically at the start of the tracking system. This experiment helps to find specific threshold levels for applications in distorted environments and shows the behavior of the quality value distribution in combination with different transmitter and sensor setups. By understanding the quality distribution over the tracking volume it is possible to adapt the quality parameter settings at the API to determine a balanced threshold level for a specific application.

6.3 Results

6.3.1 Jitter Error

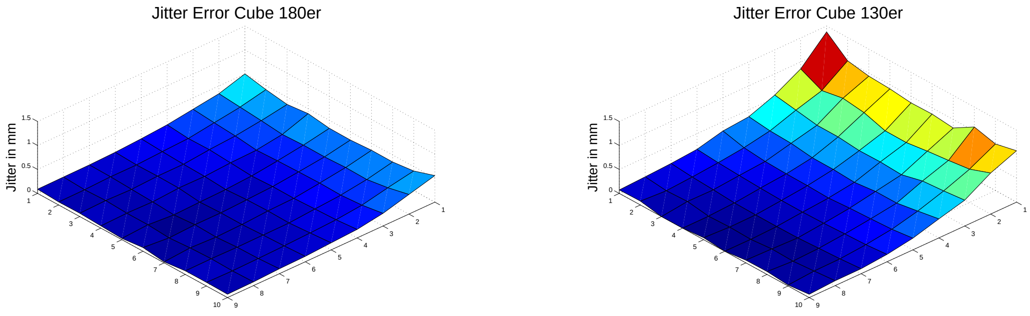

a) Cube 180er Sensor

b) Cube 130er Sensor

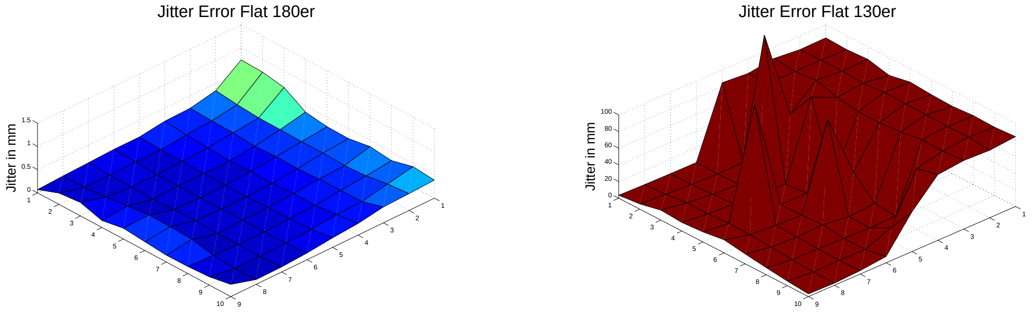

c) Flat 180er Sensor

d) Flat 130er Sensor

Figure 6.3: **Jitter error vs. grid position**. The z values indicate the resulting jitter in mm of (a) mid-range transmitter with model 180 sensor, (b) mid-range transmitter with model 130 sensor, (c) flat transmitter with model 180 sensor and (d) flat transmitter with model 130 sensor.

The plots in figure 6.3 display the jitter error as z value, whereas x and y correspond to the measurement positions on the base plate. With all four different system setups jitter errors increase with higher distances from the emitter. The Ascension mid-range transmitter with model 180 sensor shows the lowest mean jitter error values across the entire measurement plate (0.15 ± 0.12mm). If the system runs with the smaller receiver of diameter 1.3mm, the jitter error was much higher at an increasing distance to the field generator (0.31 ± 0.32mm). The flat transmitter in combination with the model 180 sensor shows a slightly higher jitter error (0.2 ± 0.13) with small drawbacks near the transmitter and (even more) with an increasing distance from the field generator. The worst jitter error in the experiments was observed at the flat field generator in combination with the receiver of 1.3mm diameter. Especially in regions >25cm away from the flat transmitter the results were extremely bad (41.9577 ± 41.2579 mm) and influenced the results negatively. A summery of the jitter error experiments can be seen in table 6.1.

err_{jitter}	"3D Guidance" mid-range transmitter	"3D Guidance" flat transmitter
Model 180 sensor	0.1533(±0.1171)mm	0.1999(±0.1258)mm
Model 130 sensor	0.3133(±0.3218)mm	41.9577(±41.2579)mm

Table 6.1: The **Jitter error results** of the "3D Guidance" with flat and mid-range transmitter as well as with two receiver types. The table contains the evaluated mean and standard deviation [mm].

6.3.2 Positional Error

For the positional error both the mean position error at all system/receiver combinations and the cumulative row distance error which is computed between the first position in each row and the other grid locations were evaluated.

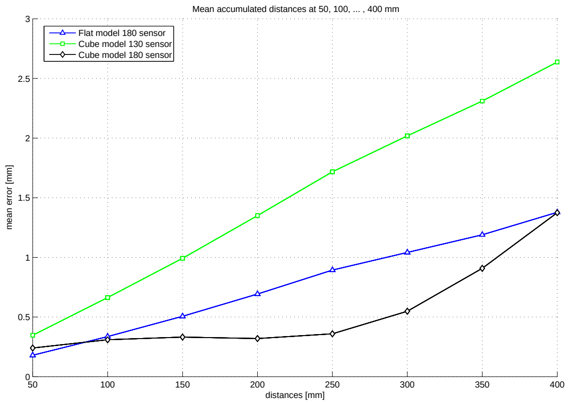

Figure 6.4: The mean **relative position error**. All possible distances of $50mm, 100mm, ..., 400mm$ of the grid positions were calculated and compared to the metric distances of the plate (flat with sensor 1.3mm was out of scale).

err_{pos}	at 50mm	at 150mm	at 300mm	at 400mm
Mid-range/ model 180	0.2405 (±0.7490)	0.3316 (±0.8083)	0.5482(±0.3066)	1.3749(±1.336)
Mid-range/ model 130	0.3469 (±0.2805)	0.9921 (±0.6448)	2.0186 (±1.6716)	2.6373(±2.2903)
Flat/ model 180	0.1794 (±0.2363)	0.5062 (±0.3265)	1.0415 (±0.8620)	1.3781(±1.1986)
Flat/ model 130	36.1352 (±118.0117)	79.2057 (±85.4615)	48.1971 (±37.4078)	57.5682(±67.8392)

Table 6.2: The **mean relative position error** results of the "3D Guidance" with flat and mid-range transmitter in combination with the two receiver types. The table contains the evaluated mean and standard deviation values [in mm].

The results of the mean positional error are displayed in figure 6.4 and summarized in table 6.2. The best performance was observed with the mid-range transmitter in combination with the sensor of 1.8mm (0.6238±0.6901mm) which has the lowest positional errors at these experiments. The flat field generator with the bigger receiver has a slightly higher positional error than the same sensor with the mid-range transmitter (0.7763±0.70073mm). The results of the mid-range transmitter with 1.3mm were higher than at the previous two systems but still at an acceptable level (1.498±1.2075mm). The flat transmitter equipped with the smaller receiver showed again very bad results (55.2766±77.1801mm).

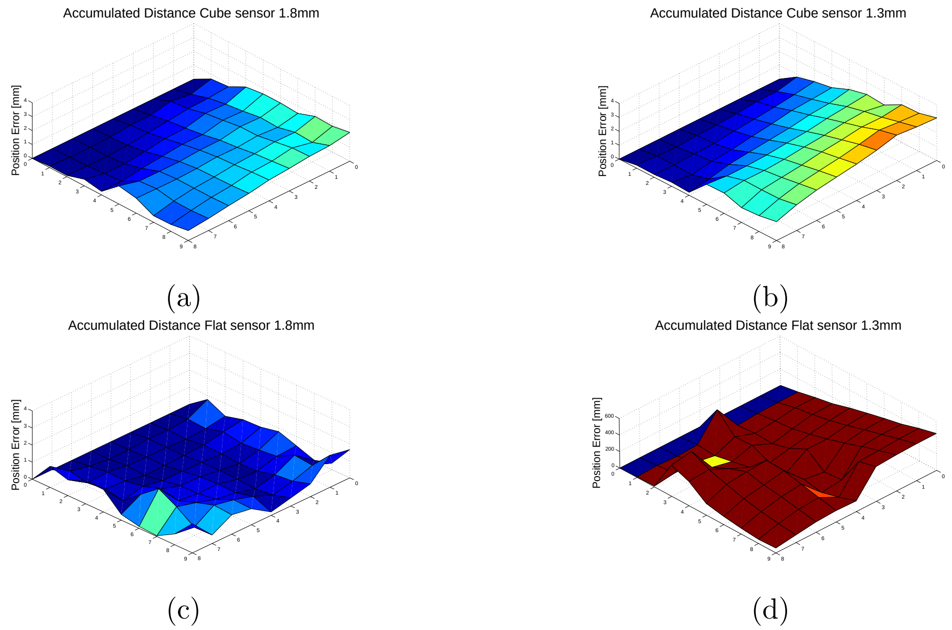

(a) (b)

(c) (d)

Figure 6.5: **Cumulative row distance**. The z values are calculated between the first position in each row $P(i,1)$ and the other row positions $P(i,j)$ of (a) midRange transmitter with sensor 1.8mm and (b) with sensor 1.3mm, (c) flat transmitter with sensor 1.8mm and 1.3mm (d).

The cumulative row distance error is displayed in figure 6.5. The most balanced error distribution over the grid was evaluated at the mid-range transmitter with the receiver of 1.8mm diameter. In combination with the sensor model 130, the plot shows an noticeable falling accuracy at increasing distances from the reference position. The flat field generator shows comparable results to the midrange emitter with the sensor of diameter 1.8mm, however, with drawbracks of slightly higher values near the field generator and at increasing distance from the emitter. The flat transmitter with 1.3mm sensor shows a very unbalanced error distribution over the grid.

6.3.3 Orientational Error

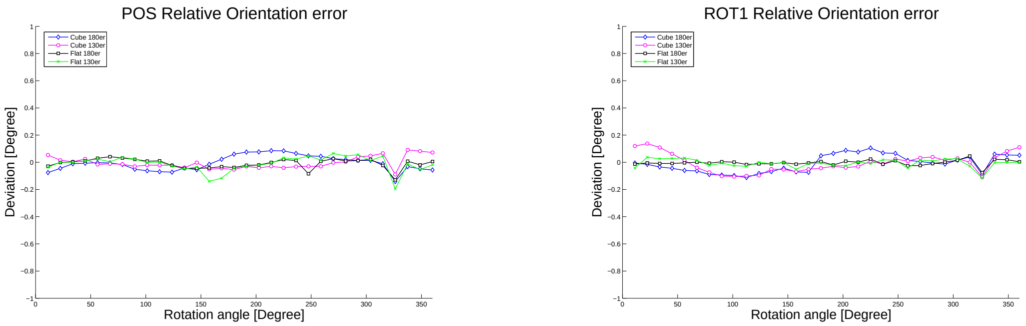

(a) Pos (b) Rot1

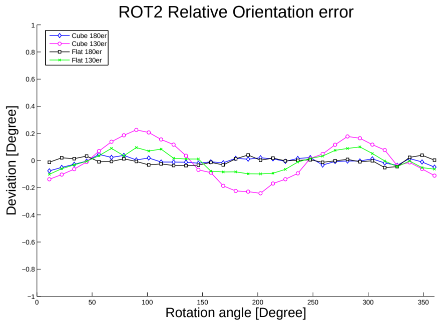

(c) Rot2

Figure 6.6: The **orientational error** of the “3D Guidance” system. The mid-range field generator with model 180 receiver is displayed in blue and model 130 in pink. The flat transmitter combined with the sensor of 1.8mm diameter is visualized in black and with diameter 1.3mm in green. Both receiver types were fixed at the sensor mount in positions Pos (a), Rot1 (b) and Rot2 (c) to evaluate the rotation about all three main axes.

The results in figure 6.6 show the orientation error about all three main axes. The flat field generator with model 180 receiver shows the best performance at all three fixation positions of the sensor mount (Pos 0.03°, Rot1 0.01°, Rot2 0.02°). In combination with the smaller

err_{rot}	"3D Guidance" mid-range transmitter	"3D Guidance" flat transmitter
	Pos (axial)	
Model 180 sensor	0.0453(±0.0308)°	0.0261(±0.0249)°
Model 130 sensor	0.0359(±0.0242)°	0.0387(±0.0413)°
	Rot1	
Model 180 sensor	0.0569(±0.0306)°	0.0136(±0.0147)°
Model 130 sensor	0.0572(±0.0382)°	0.0220(±0.0214)°
	Rot2	
Model 180 sensor	0.0204(±0.0162)°	0.0189(±0.0146)°
Model 130 sensor	0.1196(±0.0671)°	0.0559(±0.0334)°

Table 6.3: The **orientation error results** of the "3D Guidance" with flat and mid-range transmitter in combination with the two receiver types. The table contains the evaluated mean and standard deviation values [in deg].

type of receivers the results were slightly higher with drawbacks at Rot2 rotation (Pos 0.04°, Rot1 0.02°, Rot2 0.06°). The mid-range transmitter in combination with the model 180 sensor was less accurate than the flat field generator at orientational measurements (Pos 0.05°, Rot1 0.06°, Rot2 0.02°). The worst rotational measurements were evaluated with the mid-range field generator together with the smaller receiver of diameter 1.3mm particularly at Rot2 rotation (Pos 0.04°, Rot1 0.06°, Rot2 0.12°). Altogether the flat transmitter showed an increased performance in terms of orientation determination compared to the mid-range field generator at all experiments. The rotation error results are summarized in table 6.3.

6.3.4 Metallic Distortions

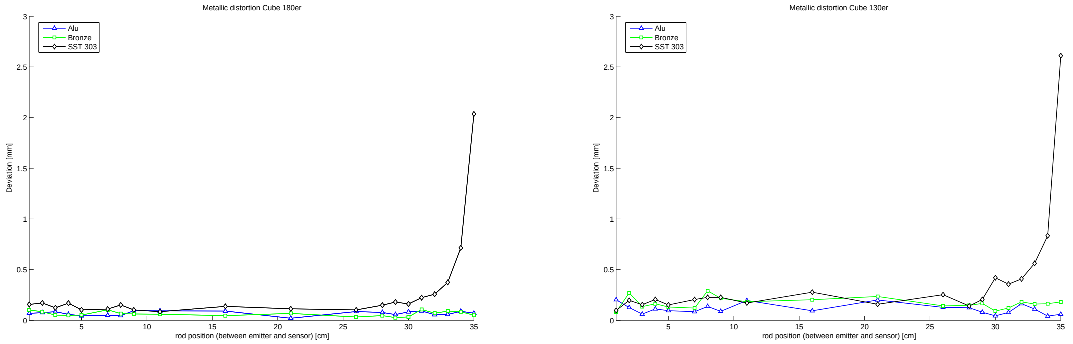

(a) Cube 180er Sensor

(b) Cube 130er Sensor

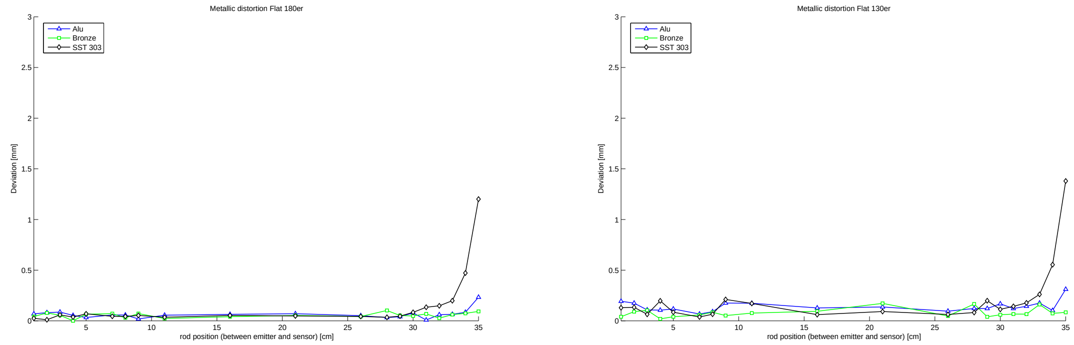

(c) Flat 180er Sensor

(d) Flat 130er Sensor

Figure 6.7: A comparision of **metallic distortions in different systems**: Mid-range transmitter with model 180 sensor(a) and model 130 (b) as well as the flat transmitter with the receiver of diameter 1.8mm (c) and 1.3mm (d) (SST416 was out of scale).

The results visualized in figure 6.7 show the influence of metallic objects on the accuracy of the “3D Guidance” system[4]. The flat transmitter in combination with the model 180 sensor showed the best performance with nearby metallic objects in the operating volume (max: 12.73mm(SST 416), min: 0.05mm(Bronze)). Also in combination with the smaller receiver of diameter 1.3mm this field generator was less affected by the presence of metal in the operating volume in the experiments (max: 13.13mm(SST 416), min: 0.08(Bronze)) than the mid-range transmitter. In combination with both the model 180 sensor (max: 16.81mm(SST 416), min: 0.05mm(Bronze)) and the receiver of diameter 1.3mm (max: 17.51mm (SST 416), min: 0.17mm (Bronze)) the mid-range field generator was much more sensitive due to the induced metallic rods. The comparison of the different system setups

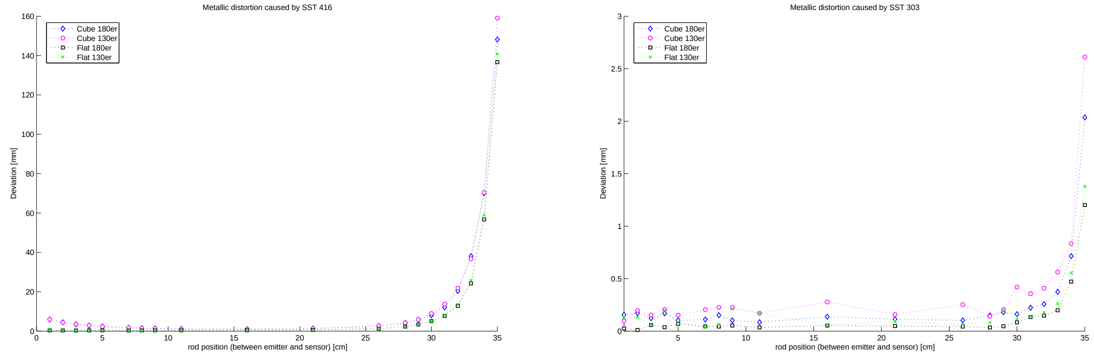

(a) SST 416 (scaled)

(b) SST 303

---

[4] Please note that the SST416 is not displayed in figure 6.7 because the distortion caused by this material was at a much higher level.

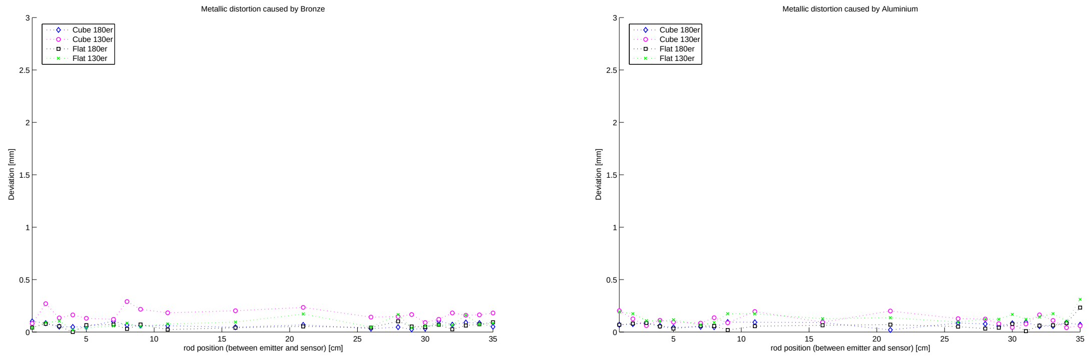

(c) Bronze

(d) Aluminium

Figure 6.8: The **influence of different metallic objects** made of steel SST416(a), SST303(b), bronze (c) and aluminium(d) to the systems. The flat transmitter (with sensor of diameter 1.8mm in black and 1.3mm in green) is less sensitive to all samples in comparision to the cube transmitter (with model 180 sensor in blue and 1.3mm in pink).

shows clearly that the sensor of diameter 1.8mm was less sensitive to distortion during all experiments. Additionally, the mid-range transmitter seems to be much more affected to metal than the flat. However, we were surprised that the distortion still appears because Ascension stated this system as "metal immun" [68, 5]. But especially with stainless steel (SST416 and SST303) the experiments show still significant distortions.

err_{metal}	"3D Guidance" mid-range transmitter	"3D Guidance" flat transmitter
	SST 416	
Model 180 sensor	16.8102(±34.2305)mm	12.7269(±31.2383)mm
Model 130 sensor	17.5060(±36.2966)mm	13.1338(±32.2669)mm
	SST 303	
Model 180 sensor	0.2810(±0.4252)mm	0.1420(±0.2624)mm
Model 130 sensor	0.3928(±0.5362)mm	0.2110(±0.2898)mm
	Bronze	
Model 180 sensor	0.0540(±0.0237)mm	0.0501(±0.0240)mm
Model 130 sensor	0.1692(±0.0528)mm	0.0797(±0.0419)mm
	Aluminium	
Model 180 sensor	0.0696(±0.0201)mm	0.0650(±0.0436)mm
Model 130 sensor	0.1111(±0.0480)mm	0.1414(±0.0515)mm

Table 6.4: The results of the **metallic distortion** experiments of the "3D Guidance" system with flat and mid-range transmitter in combination with the two receiver types. The table contains the evaluated mean and standard deviation values of all tested materials (SST 416, SST303, Bronze, Aluminium)[in mm].

The plots in figure 6.8 clearly show that the distortion caused by SST416 was much higher than for the other materials for all configurations[5]. The error induced with SST303 was also considerable with all transmitter/receiver combinations. Aluminium and bronze did not cause significant distortions to the system accuracy, where bronze affects the results a little bit more than aluminium. In all experiments the highest errors at all system setups was observed when the metallic objects were located close to the sensor.

6.3.5 Quality Values

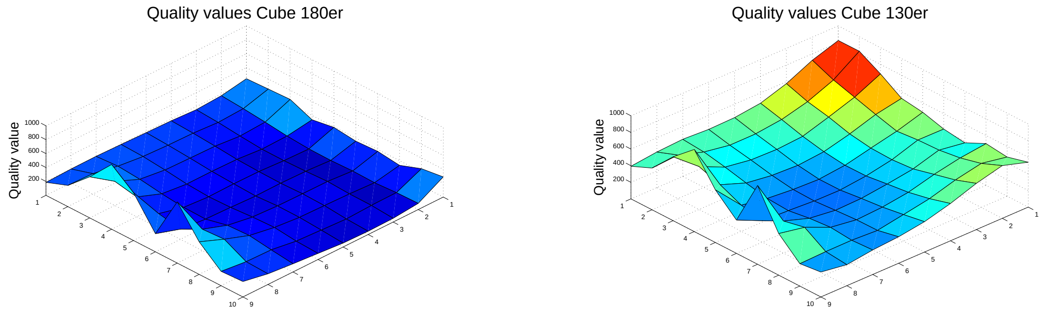

(a) Cube 180er Sensor (b) Cube 130er Sensor

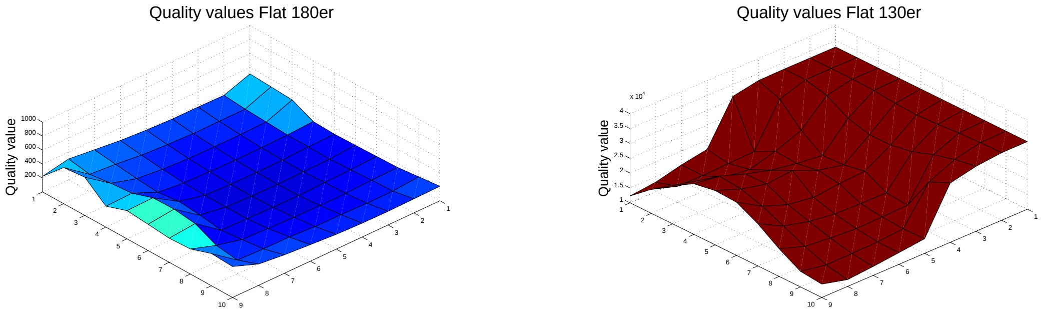

(c) Flat 180er Sensor (d) Flat 130er Sensor

Figure 6.9: **Ascension quality value vs. grid position**. The z values indicate the measured quality value of (a) mid-range transmitter with model 180 sensor, (b) mid-range transmitter with model 130 sensor (c) flat transmitter with model 180 sensor (d) flat transmitter with model 130 sensor.

In figure 6.9 the quality values are displayed as z values, whereas x and y denote the measurement position at the polycarbonate plate. Both the mid-range and flat transmitter showed a balanced distribution of the quality value in combination with model 180 receiver

---

[5] Please note that the plot in figure 6.8(a) is scaled in y direction because the distortion caused by that material was much higher than by the other metals.

(mid-range: 181.35 ± 151.86, flat 195.4 ± 106.39). In this case it seems to be quite easy to define a meaningful threshold, which helps to accept or discard the current tracking data in a distorted environment. The values of the mid-range emitter with the sensor of diameter 1.3mm are highly varying over the tracking volume with the best behavior in the center of the experimental area (415.47 ± 158.95). The flat transmitter in combination with the model 130 receiver shows an unbalanced behavior with very high values at distances > 25cm away from the emitter (23302 ± 7201.8). However, the quality value seems to be a good indicator of error in this system and a meaningful threshold can be easily defined to discard corrupted data. The experimental results are summarized in table 6.5.

Quality value	"3D Guidance" mid-range transmitter	"3D Guidance" flat transmitter
Model 180 sensor	181.3516(±151.8576)	195.3944(±106.3874)
Model 130 sensor	415.4726(±158.9457)	23302(±7201.8)

Table 6.5: The **quality values** of the "3D Guidance" with flat and mid-range transmitter in combination with the two receiver types. The table contains the evaluated mean and standard deviation values.

6.4 Discussion

In these experiments the "3D Guidance" system was evaluated with different types of sensors and field generators. Both the mid-range transmitter and flat transmitter as well as two different sensor types of diameter 1.8mm and 1.3mm were evaluated. With all system/receiver combinations some advantages and disadvantages were observed:

The mid-range transmitter showed a very good performance at the jitter error and positional measurements, especially with the receiver of diameter 1.8mm. However, orientation measurements were not as accurate as with the flat transmitter and the system is much more affected by metallic distortions. Additionally, the mid-range field generator seems to work better with the smaller receiver of 1.3mm. The flat transmitter has small drawbacks in terms of jitter error and positional measurements. The advantages of the system are an increased performance at the orientational measurments and metallic distortions. The term "metal immun" doesn't seems to be an adequat attribute of the system, however, the influence of nearby metals in the operating volume was clearly reduced. In combination with the smaller model 130 sensor the system reported extremly bad results in regions >25cm away from the emitter. A threshold level can be defined to discard corruptive measurements by using the provided quality value of the system.

Jitter error measurements can give an idea of a sensitive operating volume with respect to desired accuracy requirements. The magnitude of jitter values usually increases with raising distance from the emitter. Considering the metallic distortion experiments the mid-range transmitter was much more affected by metals than the flat transmitter system. When the metallic object was located in close proximity to the receiver, the highest deviation with both systems was observed. At all experimental systems stainless steel has the most negative influence on system accuracy with the highest distortion caused by SST 416[6] and (less) SST 303. Aluminium and bronze are not so crucial for system accuracy and just have small negative influence on the measurements. At the orientational experiments the flat emitter performed better than the mid-range transmitter and the sensor model 180 provides clearly the higher rotational accuracy. Similarly at the positional determination the model 130 sensor was less accurate than the receiver of 1.8mm. The flat showed an extremly bad behavior with the smaller sensor type for jitter and positional errors. Quality values can give a basic idea of the grade of distortion of a given tracking data, but it is not always easy to define a meaningful threshold to discard or accept a measurement. Additionally, the initial experiments (see section 4.4) showed that the quality value is sometimes deceptive and can just provide a non-reliable hint of the current distortion level. It strongly dependens on the distance between receiver and transmitter.

6.5 Comparison to the previous work

Hummel *et al.* [32, 33] accomplished the experiments by using the same assessment protocol for the Ascension MicroBird, the NDI Aurora and the newer Aurora 6DOF system. A comparision between the previous results and the experiments described in this chapter is given following.

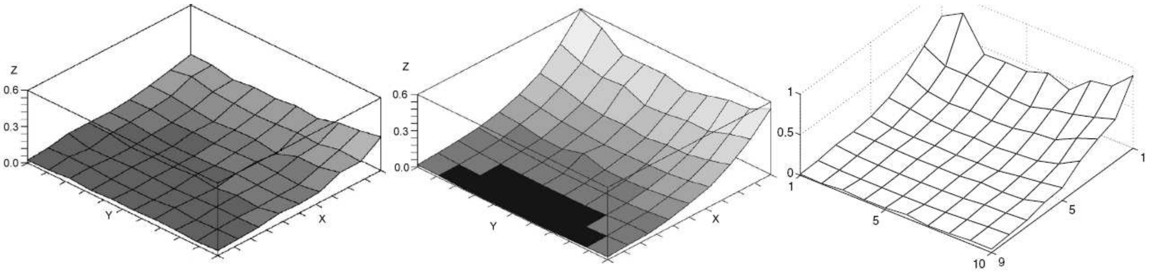

(a) (b) (c)

Figure 6.10: The **jitter vs. grid position** of the Ascension Microbird (a), NDI Aurora (b) and the newer NDI Aurora 6DOF (c) (source [32, 33]).

Considering the jitter results (see figure 6.10) the lowest values over the grid were observed at the MicroBird system (0.08±0.06mm). At both 3D Guidance transmitters the jitter error was higher (mid-range: 0.15±0.11mm; flat: 0.19±0.13mm) than at the MicroBird system. The NDI systems showed a similar performance than the 3D Guidance transmitters and

---

[6] SST 416 has a higher magnetic permeabiltiy than SST 303. This fact explains the different distortion levels caused by such materials.

the results are higher than at the MicroBird. Additionally, the newer 6DOF NDI system has slightly higher jitter values compared to its predecessor system (Aurora: 0.14±0.15mm; newer Aurora 6DOF: 0.17±0.19mm).

For the positional error determination the 3D Guidance transmitters showed the best performance (mid-range 0.24±0.75mm (at 50mm) and 0.55±0.30 (at 300mm); flat 0.17±0.23m (at 50mm) and 1.04±0.86mm (at 300mm)). The newer 6DOF Aurora system has a much higher positional accuracy than its predecessor system (newer Aurora 6DOF 0.25±0.22mm (at 50mm) and 0.97±1.01mm (at 300mm); Aurora 0.96±0.68mm (at 50mm) and 5.35±3.42mm (at 300mm)) and the positional error was reduced by circa factor three (see also figure 6.11). Also a bad performance was observed at the Ascension MicroBird system (1.14±0.78mm (at 50mm) and 3.17±2.88mm (at 300mm)).

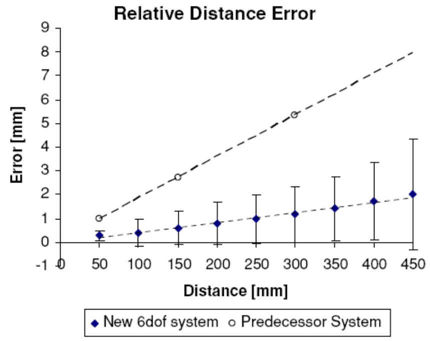

Figure 6.11: The **relative distance error** of the NDI Aurora and the newer Aurora 6DOF (source [33]).

Additionally, the cumulative distance error was also observed in the previous publications of Hummel *et al.* [32, 33] and the results are displayed in figure 6.12.

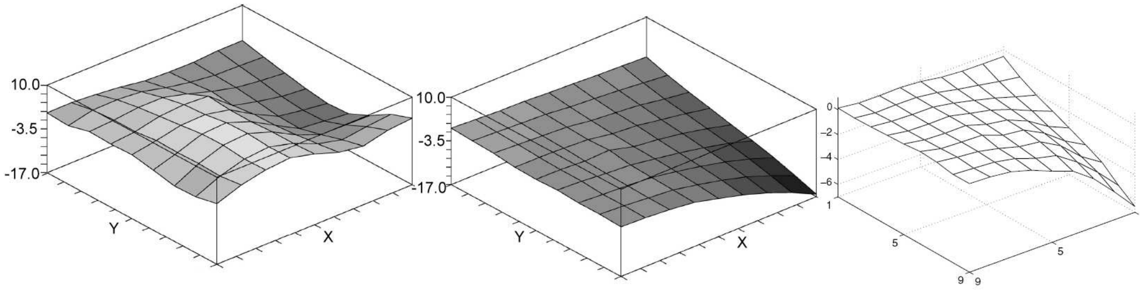

(a) (b) (c)

Figure 6.12: The **cumulative row distance vs. grid position** of the Microbird (a), Aurora (b) and the newer Aurora 6DOF (c) (source [32, 33]).

For orientation determination (see figure 6.13) the best performance was observed at the 3D Guidance in combination with the flat transmitter (Pos 0.03°, Rot1 0.01°, Rot2 0.02°). The MicroBird (0.04°) and the 3D Guidance mid-range transmitter showed similar results (Pos 0.05°, Rot1 0.06°, Rot2 0.02°), both at a very low level compared to the NDI systems. The Aurora (0.51°) and the newer 6DOF Aurora (Pos 0.20°, Rot1 0.68°) are less accurate considering rotational measurements than the investigated Ascension systems.

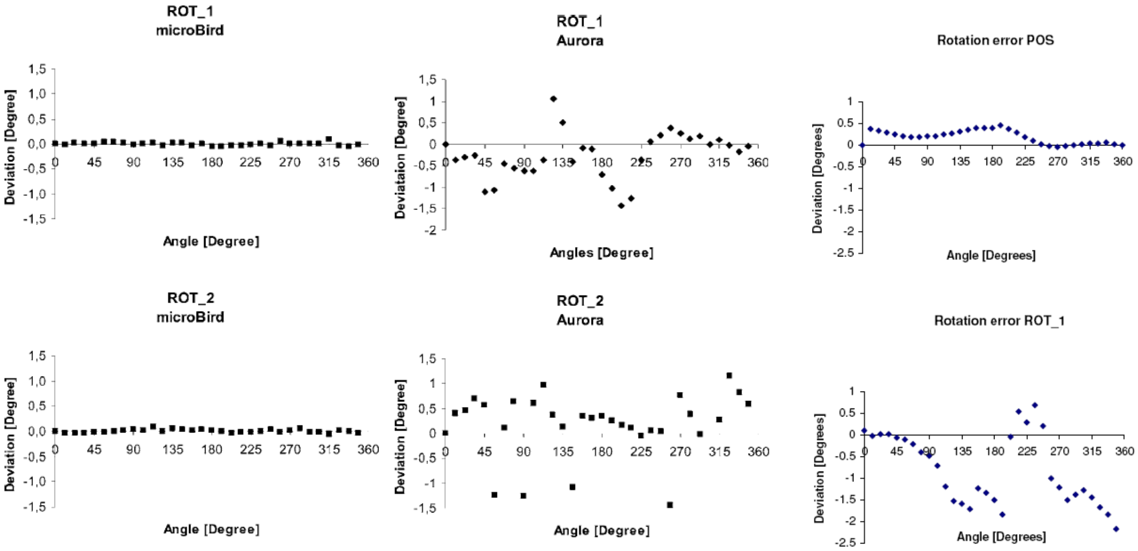

(a) (b) (c)

Figure 6.13: The **orientational error** of the Microbird (a), Aurora (b) and the newer Aurora 6DOF (c) (source [32, 33]).

Considering the metallic distortion experiments (see figure 6.14) the highest error at all system was caused by SST416. The NDI trackers are less affected by this material (Aurora: max. 4.2mm, newer Aurara 6DOF: max. 9.4mm) compared to the Ascension systems, where heavily distortions were observed (3D Guidance flat: max. 136.66mm, 3D Guidance mid-range: max. 148.16mm, MicroBird: >100mm). However, the Ascension EMTS are not as much influenced by Aluminium and Bronze as the older Aurora system. The newer 6DOF Aurora tracker showed an improved performance at SST303, aluminium and bronze compared to its predecessor system. The highest error values at the Ascension systems were observed with the distortion causing material at close distance to the receiver, whereas the NDI trackers are most sensitive to metals placed near the field generator.

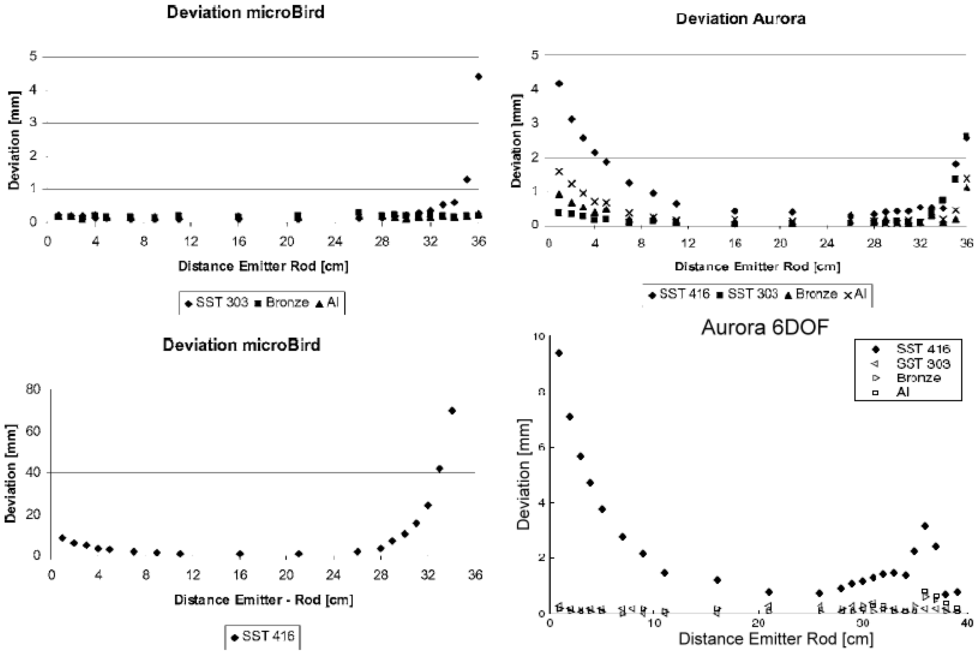

Figure 6.14: The **metallic distortion** for the Microbird (left), Aurora (upper right) and the newer Aurora 6DOF (lower right) (source [32, 33]).

All results of the previous work of Hummel *et al.* [32, 33] are summarized following in table 6.6.

Error	**MicroBird 1.8mm**	**Aurora**	**newer Aurora 6DOF**
Jitter error	0.08 ± 0.06mm 0.74°	0.14 ± 0.15mm 0.33°	0.17 ± 0.19mm —
Position error	1.14 ± 0.78mm(at 50mm) 3.17 ± 2.88mm(at 300mm)	0.96 ± 0.68mm(at 50mm) 5.35 ± 3.42mm(at 300mm)	0.25 ± 0.22mm(at 50mm) 0.97 ± 1.01mm(at 300mm)
Rotation errror	0.04°	0.51°	0.20° ± 0.14° (POS) 0.91° ± 0.68° (ROT2)
Metallic distortions	max. ≥100mm (SST 416)	max. 4.2mm (SST 416)	max. 9.4mm (SST 416)

Table 6.6: The **previous results** were published by Hummel *et al.* [32, 33], where the MicroBIRD, Aurora 5DOF and the newer Aurora 6DOF were evaluted by using the same assessment protocol and machined base plate (source [32, 33]).

7 Applications

The number of applications using electromagnetic tracking systems has grown enourmously in recent years [32]. These systems are essential in the field of image-guided surgery (IGS) or therapy (IGT) e.g. laparoscopy, ultrasound calibration, endoscopic navigation, gene therapy, neurosurgery, cardiology or catheter tracking. Furthermore, EMTS can not only be found in medical environments, but also in a number of industrial or military applications.

In laparoscopic interventions EMTS can be used to determine the real-time position of a flexible ultrasound transducer inside the human body. This procedure allows to visualize B-scan images acquired by the ultrasound device in relation to the image data of the patient during a surgery[1]. Feuerstein *et al.* [19, 18, 20] used such systems in laparoscopic interventions in combination with several online error detection and correction techniques to eliminate dynamic tracking errors caused by induced metallic objects in the operating room.

EMTS can also be applied for 3D ultrasound calibration [17, 56]. Both position and orientation of the ultrasound probe are tracked in real-time by an EMTS receiver to display the informations extracted from the 2D ultrasound image in a 3D context. For that reason an advanced calibration procedure is necessary to determine the transformation from the ultrasound probe to the electromagnetic receiver. However, these systems usually suffer from the inaccurate measurement of the EMTS and the presence of metallic substances in the ultrasound probe [34, 66].

In the next sections two systems using EMTS are described: A camera calibration procedure for augmented camera systems and navigated bronchoscopy application. The necessary mathematical background, the involved transformations and the registration or calibration procedures of the systems are introduced on the following pages.

---

[1] Either a superimposed camera image or a virtual 3D visualization computed from previously acquired CT or MRI data can be used to display the informations.

7.1 Camera Calibration

Camera calibration techniques are widely used in medical navigation[2] systems because they allow to superimpose endoscopic images with additional informations about anatomical structures, metric properties or navigation details. Mathematically, a camera calibration is an estimation of specific parameters based on the pinhole camera model which defines a distinct mapping from 3D world coordinates to 2D image coordinates. After a short introduction to the basic camera model and calibration procedures both optical distorted visual systems and oblique-viewing endoscopes are described in this section.

7.1.1 The pinhole camera model

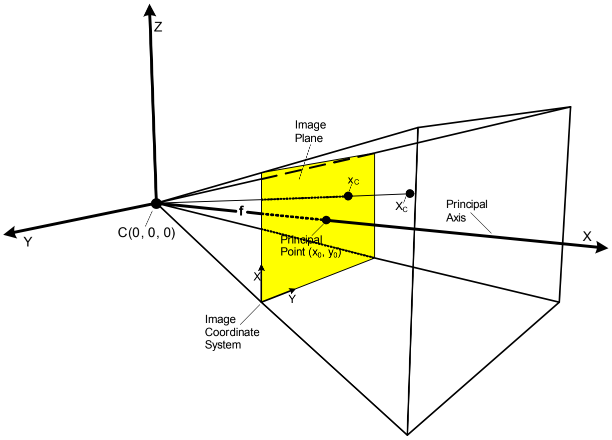

Figure 7.1: The basic **pinhole camera model** defines the projection of a point X_c in 3D WCS to its corresponding position in 2D ICS. The image point x_c is defined as the intersection of a distinct line from C to X_c and the image plane.

The basic model of a perspective camera can be seen in figure 7.1. The position of the camera $C(0, 0, 0)$ is the center of a projection which defines a mapping from an arbitrary point X_c in world coordinate system (WCS) to its 2D location x_c in the image coordinate system (ICS). In this model the x axis is usually denoted as principal axis which intersects the perpendicular aligned image plane at the principal point $p_0 = (x_0, y_0)$. The distance f between C and p_0 is called the focal length and both f and p_0 belong to the unknown parameters in the calibration procedure. Normally, the origin of the image coordinate system will differ from the principal point p_0 and a scaling of x and y axis can occur in the picture coordinate system. These unknowns have also to be computed in the calibration algorithm.

---

[2] Camera calibration techniques are additionally crucial in many machine vision systems, e.g. in robotics.

Geometrically, an image point x can be seen as the intersection of the image plane and a ray between the origin C and the position X in the WCS. This defines a projective mapping P which is modeled by a 3×4 matrix with 11 degree of freedom and is further subdivided into intrinsic and extrinsic parameters by using a matrix decomposition technique [29]. Extrinsic camera parameters define the transformation from the WCS to the camera coordinate system (CCS), while intrinsic camera parameters describe the projection from 3D CCS to the 2D ICS. Mathematically, the mapping of this point X in WCS into ICS x is described in the following way:

$$\begin{aligned}
\lambda \cdot x_{img} &= P_{3\times 4} \cdot X_{world} \\
&= KR[I| - \bar{C}] \cdot X_{world} \\
&= \underbrace{\begin{bmatrix} \alpha_x & s & x_0 \\ 0 & \alpha_y & y_0 \\ 0 & 0 & 1 \end{bmatrix}}_{K} \cdot \underbrace{\begin{bmatrix} r_{11} & r_{12} & r_{13} \\ r_{21} & r_{22} & r_{23} \\ r_{31} & r_{32} & r_{33} \end{bmatrix}}_{R} \cdot \underbrace{\begin{bmatrix} 1 & 0 & 0 & -\bar{C}_x \\ 0 & 1 & 0 & -\bar{C}_y \\ 0 & 0 & 1 & -\bar{C}_z \end{bmatrix}}_{I|-\bar{C}} \cdot \begin{pmatrix} X_1 \\ X_2 \\ X_3 \\ 1 \end{pmatrix}
\end{aligned}$$

In this equation $\bar{C}$ denotes the camera origin in world coordinates, R is a 3×3 rotation matrix which defines the mapping between the different orientations of world coordinate frame and camera coordinate systems, and K is the camera calibration matrix. Five DOF are usually necessary to model the intrinsic paramaters of the matrix K and six DOF for the extrinsic parameters[3]. These unknowns will be determined in the camera calibration procedure. In table 7.1 all necessary parameters are summarized:

Intrinsic camera parameters	**Extrinsic camera parameters**
• coordinates of the principle point (x_0, y_0)	• rotations between WCS and CCS
• (α_x, α_y) scale factors in x and y direction	• translations of the camera center
• skew parameter s (normally set to zero)	
• distortion coefficients $\kappa_1, \kappa_2, \kappa_3, \ldots$	

Table 7.1: The **intrinsic and extrinsic camera parameters** with 11 DOF. The 6 DOF for extrinsic parameters are subdivided into three for orientation and three for translation between WCS and CCS. The 5DOF for intrinsic parameters belongs to the 5 unknowns in the camera calibration matrix K.

---

[3] Three DOF for the rotation about all three main axes (α, β, γ) in R and three DOF for the translation (x, y, z) to the origin C.

7.1.2 Radial lens distortion

Additionally, camera lenses are usually radial distorted[4]. This effect can be described by additional unknown parameters which are denoted as the distortion coefficients $\kappa_1, \kappa_2, \ldots$. The radial distortion can be modeled by a nonlinear function L, which is defined as

$$\begin{pmatrix} x_d \\ y_d \end{pmatrix} = L(\tilde{r}) \cdot \begin{pmatrix} \tilde{x} \\ \tilde{y} \end{pmatrix}$$

where $(\tilde{x}, \tilde{y})$ is the undistorted image position, $\tilde{r}$ is the radial distance from the center of distortion (computed by $\tilde{r} = \sqrt{\tilde{x}^2 + \tilde{y}^2}$) and $L(\tilde{r})$ is the distortion factor with the radius as parameter. To correct this effect an approximation to the function $L(\tilde{r})$ is given by the Taylor expansion

$$L(r) = 1 + \kappa_1 r + \kappa_2 r^2 + \kappa_3 r^3 + \ldots$$

with $L(0) = 1$. The unknown coeffcients $\{\kappa_1, \kappa_2, \kappa_3, \ldots, x_c, y_c\}$ can be computed during the estimation of P by minimizing an error cost function[5] [29]. The correction of the lens distortion will then be done by using

$$\begin{aligned} x_{corrected} &= x_c + L(r)(x_{uncorrected} - x_c) \\ y_{corrected} &= y_c + L(r)(y_{uncorrected} - y_c) \end{aligned}$$

Zhang *et al.* [95] described an efficient method to detect the lens distortion and to correct the distorted camera image in real-time by using a lookup-table data structure.

7.1.3 Camera Calibration procedure

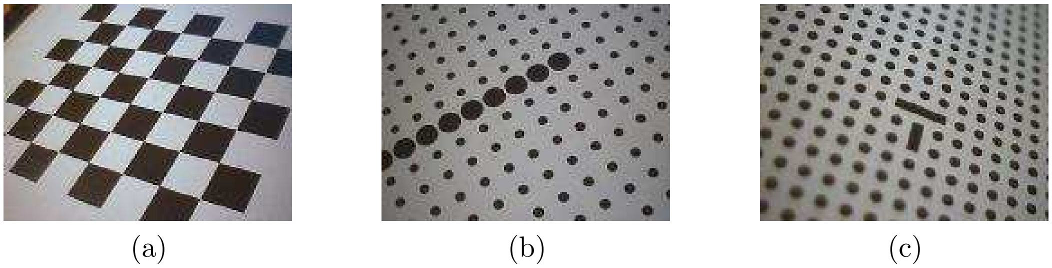
(a) (b) (c)

Figure 7.2: A couple of **planar calibration patterns** can be used to calibrate a camera device. The chessboard pattern (a) was used in several publications, whereas (b)[36] and (c)[86] were developed to deal with heavily distorted optics.

---

[4] Other kinds of lens distortion such as tangential distortion is not discribed in this thesis.

[5] Usually, two parameters κ_1, κ_2 are enough to model the radial lens distortion.

The computation of the intrinsic and extrinsic parameters is denoted as camera calibration and is widely used in industrial, medical or robotic applications. The procedure is usually performed only once before running the application and remains unchanged until the basic camera settings (e.g. zoom or focus) are adapted by the user. The process can be subdivided into the following steps which are described in more detail in [29]:

1. A calibration pattern must be rigidly attached to a planar surface. Several patterns are illustrated in figure 7.2.
2. Acquire several pictures of this pattern from different position and orientations with the camera device.
3. Extract the feature points from the images. This can be done by applying diverse image processing algorithms (see [37, 75]).
4. Identify corresponding point pairs[6] in ICS and WCS of each frame. From these results a basic equation system can be built up containing two rows for each identified pair.
5. The camera projection matrix is initially estimatated by running the DLT algorithm with the identified point pairs as input parameters after applying a normalization of the data[7].
6. The results can be optimized by minimizing a geometric cost function. In this step the estimation of the radial lens distortion coefficients can be additionally computed.

Several other algorithms were described in the literature to determine the camera calibration parameters [80, 31, 96]. In this work an existing implementation of OpenCV[8] which allows to compute all basic intrinsic and extrinsic parameters as well as radial and tangential lens distortion was used. A number of calibration patterns (see figure 7.2) were suggested by researchers to identify the corresponding point pairs. Some instances were designed to deal with heavily distorted optics which are common in medical endoscopic devices. Ishitani *et al.* [36] used such a calibration pattern to compute the intrinsic and extrinsic parameters of a heavily barrel-type lens distorted bronchoscopes. In our application a similar strategy was applied based on a pattern defined by Wengert *et al.* [86] (see figure 7.2 (c)). The algorithm to extract the pattern points and the identification of corresponding point pairs can be described in the following way:

1. Preprocessing of the image using several image filters [37]. This technique is essential to deal with different illumination situations of the camera. Furthermore, an

---

[6] Mathematically, the pairs are defined as $(p^i_{k,l} \Leftrightarrow P_{k,l})$, whereas $p^i_{k,l}$ is the location of the 3D world point $P_{k,l}$ in the i-the picture.

[7] The algorithm is described in more detail in [29].

[8] http://opencvlibrary.sourceforge.net/.

extraction of all blobs[9] from the image is performed by using OpenCV functions.

2. Compute ellipticity, solidity, area and center of gravity for each blob and filter the extracted object if the solidity is less than 0.8 or its area is smaller than a specific threshold.

3. Identify the two main bars in the image from their ellipticity[10] Additionally, the magnitude of their area allows to differ the larger bar from the smaller one. Two search directions $\vec{d_0}, \vec{d_1}$ can now be defined corresponding to the main axes of the identified bars and an initial search radius r_0 is determined.

4. Assuming that the local lens distortion is small between adjacent grid points, the search radius and the search direction is adapted in each iteration:

   - radius: $\vec{r}_{n+1} = 1.2 \cdot \|\vec{x}_n - \vec{x}_{n-1}\|$
   - direction: $\vec{d}_{n+1} = \frac{(\vec{x}_n - \vec{x}_{n-1})}{\|\vec{x}_n - \vec{x}_{n-1}\|}$

   where $\vec{x_n}$ are the image coordinates of the grid point extracted at step n. This step is repeated until no x_{n+1} can be found within the defined radius and according to the current search direction. The corresponding 3D position X_{n+1} in WCS is well-known because of the distinct coordinate system and the chosen metrics of the calibration pattern.

After acquiring several images with a number of different point pairs which were extracted with the algorithm above, the camera calibration was performed in the implemented application (see figure 7.3) by using OpenCV functions.

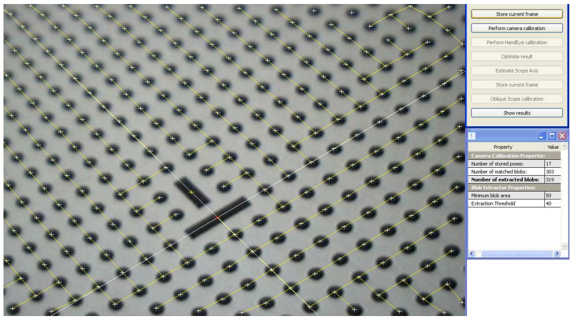

Property	Value
Camera Calibration Propertie:	
Number of stored poses:	17
Number of matched blobs:	303
Number of extracted blobs:	319
Blob Extractor Properties:	
Minimum blob area	50
Extraction Threshold	40

Figure 7.3: The figure shows the **implemented camera calibration application** using the calibration pattern of Wengert *et al.* [86] for heavily distorted optical systems. The live camera image is superimposed with the extracted metrics from the algorithm described above.

---

[9] Binary Large Object (blob).

[10] The ellipicity of both mainbars is larger than 2 due to their non-circular shape.

7.1.4 Calibration of augmented endoscopes/laparoscopes

To superimpose an endoscopic image online with additional informations, an optical tracking target or EMTS sensor have to be fixed at the camera and determine the position and orientation of the endoscope with the tracking system in real-time. The basic setups and involved transformations can be seen in figure 7.4 and are summarized following:

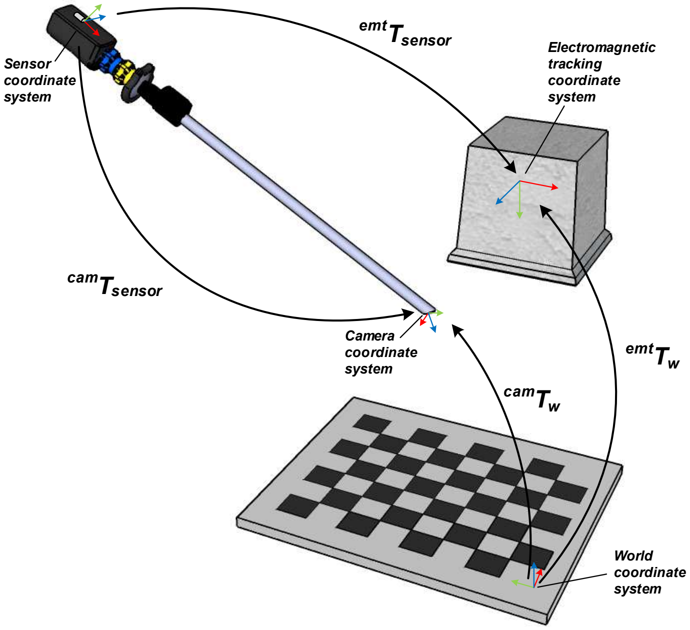

Figure 7.4: The typical setup of a real-time **augmented camera system**. The transformations from the sensor CS to the camera CS as well as from the world (pattern) coordinate system to the tracking system can be determined with a hand-eye calibration approach.

- $^{emt}\mathbf{T}_{sensor}$ from the sensor coordinate system to the electromagnetic tracking system which is usually provided dynamically by tracking the sensor attached to the camera with an EMTS.
- $^{emt}\mathbf{T}_{w}$ from the world coordinate system of the calibration pattern to the tracking system is initially unknown. This transformation will be determined during the calibration procedure with the hand-eye calibration approach.
- $^{cam}\mathbf{T}_{sensor}$ from the sensor coordinate system to the camera coordinate system is also initially unknown. This transformation will also be computed in the calibration procedure.

- ${}^{cam}\mathbf{T}_{w}$ is the extrinsic camera transformation which is usually computed in the previously described camera calibration procedure.

The unknown transformations[11] ${}^{cam}\mathbf{T}_{sensor}$ and ${}^{emt}\mathbf{T}_{w}$ are now determined with the hand-eye calibration method which was already used in section 4.3.1 within the computation of missing transformations for a hybrid magneto-optical tracking system. To find the unknowns for the augmented camera system the sensor poses have to be additionally collected during the previous camera calibration process. In combination with the computed extrinsic camera parameters for each image the necessary "hand" and "eye" motions between the acquisition positions of the i-th and j-th image can be defined:

1. The transformation ${}^{cam}\mathbf{T}_{sensor}$ can be determined with the following "hand" and "eye" motions:

$$\begin{aligned}\mathbf{T}_{sensor(i\to j)} &= \left({}^{emt}\mathbf{T}_{sensor}(j)\right)^{-1} \cdot^{emt} \mathbf{T}_{sensor}(i)\\ \mathbf{T}_{camera(i\to j)} &= {}^{cam}\mathbf{T}_{w}(j)\cdot\left({}^{cam}\mathbf{T}_{w}(i)\right)^{-1}\end{aligned}$$

   where ${}^{cam}\mathbf{T}_{w}(x)$ denotes the computed extrinsic camera parameters of the x-th image. Now the basic hand-eye equation $A\cdot X = X\cdot B$ can be applied to define the unknown transformation:

$$\begin{aligned}A\cdot X &= X\cdot B\\ \mathbf{T}_{camera(i\to j)}\cdot^{cam}\mathbf{T}_{sensor} &= {}^{cam}\mathbf{T}_{sensor}\cdot\mathbf{T}_{sensor(i\to j)}\end{aligned}$$

2. The transformation ${}^{emt}\mathbf{T}_{w}$ can be determined with the following "hand" and "eye" motions:

$$\begin{aligned}\mathbf{T}_{emt(i\to j)} &= {}^{emt}\mathbf{T}_{sensor}(j)\cdot\left({}^{emt}\mathbf{T}_{sensor}(i)\right)^{-1}\\ \mathbf{T}_{world(i\to j)} &= \left({}^{cam}\mathbf{T}_{w}(j)\right)^{-1}\cdot^{cam}\mathbf{T}_{w}(i)\end{aligned}$$

   Again the basic hand-eye equation $A\cdot X = X\cdot B$ can be rewitten to define the unknown transformation:

$$\begin{aligned}A\cdot X &= X\cdot B\\ \mathbf{T}_{emt(i\to j)}\cdot^{emt}\mathbf{T}_{w} &= {}^{emt}\mathbf{T}_{w}\cdot\mathbf{T}_{world(i\to j)}\end{aligned}$$

In both cases a linear equation system can be built up and the unknown transformation ${}^{cam}\mathbf{T}_{sensor}$ and ${}^{emt}\mathbf{T}_{w}$ can be computed by using the algorithms of Tsai and Lenz [81] or Daniilidis [15]. Additionally, an optimization can be performed in a similar way as described for the hybrid magneto-optical tracking system in section 4.3.2.

---

[11] The unknown transformation ${}^{cam}\mathbf{T}_{sensor}$ is even more important than ${}^{emt}\mathbf{T}_{w}$, because the pattern will usually be removed from the scene after the calibration procedure.

7.1.5 Calibration of oblique-viewing endoscopes

Oblique-viewing endoscopes (see figure 7.5) are widely used in today's medical applications like in arthroscopy, laparoscopy or sinus endoscopy. They improve the observation of objects which are not placed directly in front of the camera. The viewing direction of such visual systems has a typical tilt (e.g. 30°) away from the normal forward-viewing camera direction which is changeable by rotating the camera shaft. Therefore a camera model and an advanced calibration procedure was developed by Yamaguchi *et al.* [91, 92].

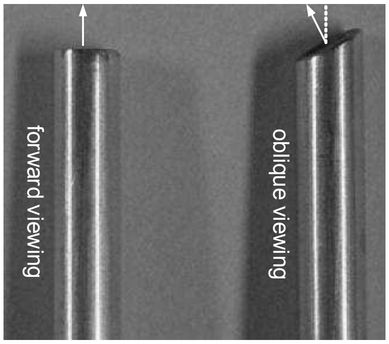

Figure 7.5: Two kinds of **endoscopes** are commonly used in minimally invasive surgery: Forward-viewing endoscopes whose viewing direction is aligned to the scope cylinder axis and oblique-viewing endoscopes which have a typical tilt between viewing direction and scope axis direction (source [91]).

Yamaguchi *et al.* [91, 92] modeled the extrinsic camera parameters which define the transformation from the world coordinate system to the camera coordinate system as a funtion of the rotation angle θ around the camera shaft axis. The intrinsic camera parameters which determine the projection from the 3D camera coordinate frame to the 2D image plane remains unchanged at an oblique-viewing endoscope. Either a rotary encoder or an additional sensor (or optical target) attached to the endoscope scope cylinder is necessary to measure this rotation θ about the camera axis. In the oblique scope calibration procedure the relationship between the current scope orientation angle θ and the extrinsic parameters has to be determined. The basic setup can be seen in figure 7.6

The following additional transformations must be available to calibrate an oblique viewing camera:

- ${}^{emt}\mathbf{T}_{rot}$ from the rotation sensor fixed at the camera shaft to the EMTS coordinate system. Its position and orientation is usually dynamically reported by the tracking system.
- ${}^{cam}\mathbf{T}_{sensor}(\theta)$ from the sensor coordinate system to the camera coordinate system modifies the previous mapping ${}^{cam}\mathbf{T}_{sensor}$: In an oblique viewing system this transformation is now expressed as a function of parameter θ.

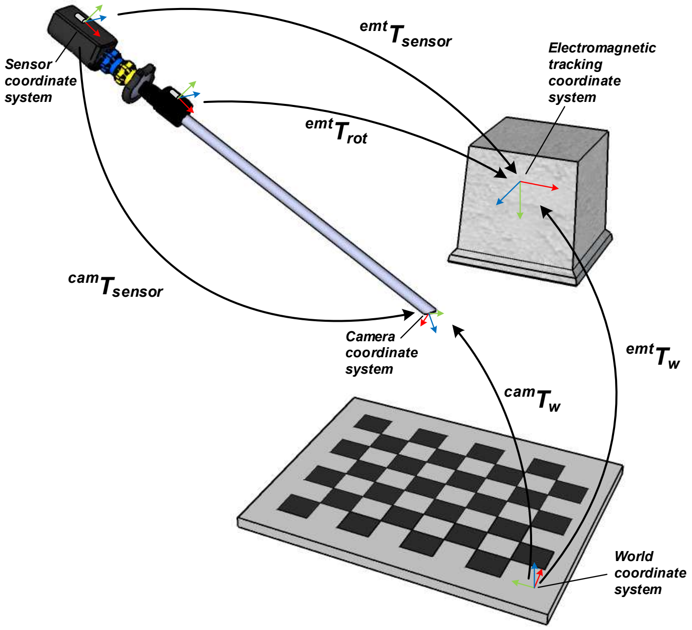

Figure 7.6: The setup of an **oblique camera calibration**. The transformations from the sensor CS to the camera CS are now expressed as a function of the rotation angle θ around the camera shaft axis. The shaft pose is determined by tracking the additional rotation sensor.

To transform a point X_{world} in homogenous world coordinates to its position at the image plane x_{image} the following transformation is necessary at oblique viewing systems:

$$x_{image} = K \cdot^{cam} \mathbf{T}_{sensor}(\theta) \cdot (^{emt}\mathbf{T}_{sensor})^{-1} \cdot^{emt} \mathbf{T}_{w} \cdot X_{world}$$

In oblique viewing systems the transformation $^{cam}\mathbf{T}_{sensor}$ is now defined in terms of the rotion angle parameter θ which is measured by tracking the rotation sensor at the camera shaft. The transformation $^{cam}\mathbf{T}_{sensor}(\theta)$ can be further subdivided into two transformations: First the rotation about the scope axis l_s of both the camera head and cylinder about θ (whole scope rotation) and the inverse rotation about $-\theta$ around l_h of the camera head (camera head rotation), where l_h is defined as the z axis of the camera coordinate system. The mapping can now be expressed as a function of the angle θ as

$$^{cam}\mathbf{T}_{sensor}(\theta) \quad = \quad \overbrace{\mathbf{T}(-\theta, l_h(\theta))}^{camera\ head\ rotation} \quad \cdot \quad \underbrace{\mathbf{T}(\theta, l_s)}_{whole\ scope\ rotation} \quad \cdot \overbrace{^{cam}\mathbf{T}_{sensor}}^{T\ at\ \theta=0^{\circ}}$$

where l_h and l_s are unknows which can be calibrated using the following procedure.

Calibration procedure for oblique viewing endoscopes

The camera calibration for oblique viewing endoscopes is a three step procedure:

1. Perform a basic camera calibration without rotating the camera shaft axis. This means that the shaft is in fixed position during the acquisition of images from different poses.
2. Estimation of the scope cylinder axis l_s (i.e. determine a point c_s and direction n_s) by rotating the camera shaft.
3. Estimation of the oblique viewing axis l_h (i.e. determine a point c_h and direction n_h) by the acquisition of pictures at different rotation angles θ_i

Both the axis of the scope cylinder and the oblique viewing axis have to be determined. To estimate the parameters n_s and c_s of the axis l_s, the rotation sensor is necessary: The camera shaft is rotated around the endoscope main axis, and the recorded rotation sensor positions defines a plane in space. The normal of this plane is the unknown parameter n_s and the center of the circle of measurement points is c_s. This can be computed by minimizing a specific cost function. To estimate the values n_h and c_h of the oblique viewing axis l_h, images at several rotations of the endoscope shaft cylinder have to be acquired. Again the desired values are computed by minimizing specific cost functions. Yamaguchi *et al.* [91, 92] also tested the accuracy of such side-viewing systems and proved the clinical applicability with a reprojection error of less than 2 pixels.

7.2 Navigated Bronchoscopy

In recent years various groups developed systems for navigated bronchoscopy based on using EMTS. In such applications a previously acquired CT scan is needed to visualize the position and orientation of the tip of a flexible bronchoscope, a forceps or biopsy tool during a bronchoscopic intervention on the screen. These systems are able to determine the current lung location without any radiation exposure[12] in contrast to the commonly used fluoroscopic systems.

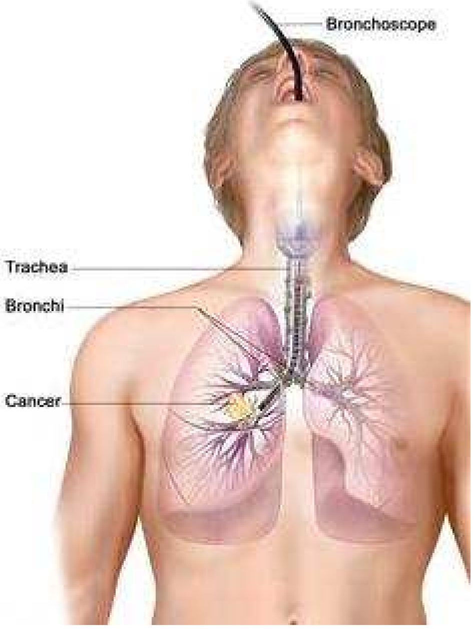

Figure 7.7: In a **navigated bronchoscopy** system at least two EMTS sensors are used to determine the movement of the patient (sensor is fixed at the sternum of the patient) and the position of a flexible bronchoscope inside the lung. The current receiver location is then displayed in a previously acquired CT scan in real-time (source [57]).

The navigated bronchoscopy application depends on the transformation ${}^{image}\mathbf{T}_{world}$ between the coordinate coordinate reference (world) frame (fixed at the patient) and preoperatively acquired CT image data. To determine this mapping in real-time it is essential to find correspondences between both coordinate systems. These relationships are usually computed only once in a registration procedure between the image and tracking space. Additionally, the movement of the patient has to be considered by sensing the motion with one (or more)

---

[12] Only the acquisition of CT data uses radiation exposure [12]. However, for diagnostic purpose the CT data is usually necessary in bronchoscopy, so that these images can be reused for the navigated endoscopy in the human lung without any additional radiation exposure for the patient.

receivers fixed at the patient's skin (e.g. at the sternum). Afterwards, the system allows to track the EMTS receiver inside the human body relative to the CT data. A navigation interface running on a host computer is usually provided to display the position and orientation in real-time at slice windows[13] or a virtual 3D view. A number of different registration procedures was proposed by researchers in the recent years. These are based on finding corresponding points, surfaces or images.

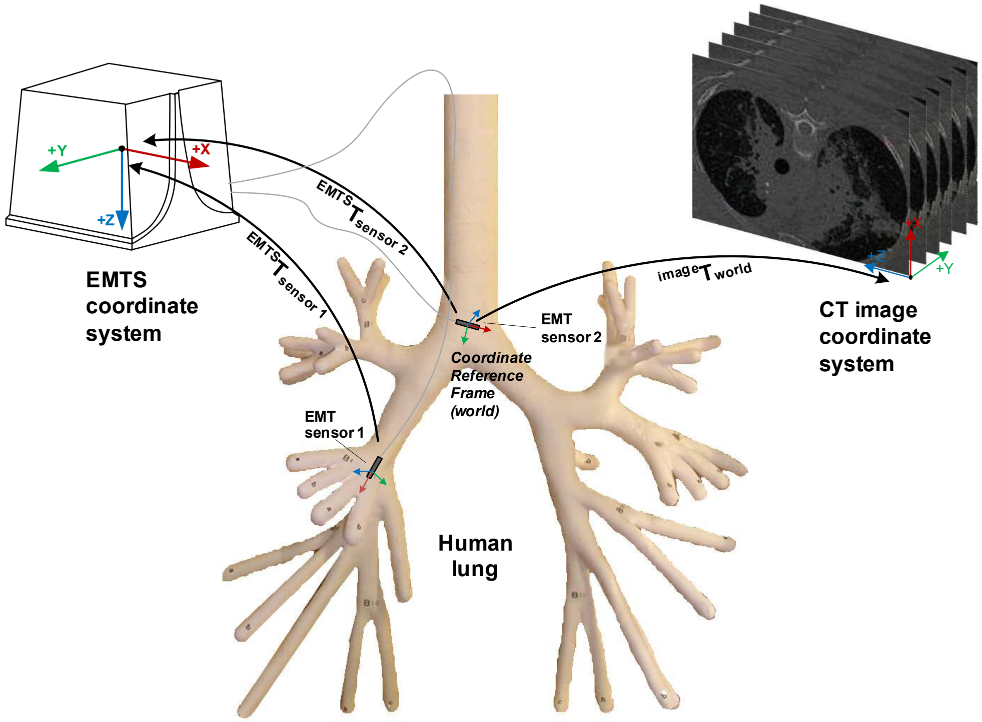

Figure 7.8: The involved **transformations in a navigated bronchoscopy** application: The first EMT receiver is usually located at the tip of a flexible bronchoscopes and reports the current location in real-time. The second sensor serves as reference frame and tracks the motion of the patient during an intervention.

The involved transformations in the navigated bronchoscopy application can be seen in figure 7.8 are described following:

- The transformation $^{EMTS}\mathbf{T}_{sensor1}$ is dynamically reported by the EMTS. The first receiver is usually moved through the working channel of a flexible bronchoscope to determine the current position and orientation of the sensor in the human lung.

- The mapping $^{EMTS}\mathbf{T}_{sensor2}$ is also determined dynamically by the electromagnetic

---

[13] Normally axial, coronal and sagital views are provided by the navigation systems to assist the surgeon at the navigation to the desired lung location.

tracker. The second sensor determines the current pose of the patient in real-time and defines the coordinate reference (world) frame.

- The transformation ${}^{image}\mathbf{T}_{world}$ is initially unknown and is determined once in a registration procedure. Several ways to compute the mapping are discussed following.

7.2.1 Point-based registration

The point-based registration method is the simplest and most commonly used method in navigated bronchoscopy systems. At least three corresponding point pairs in CT data and physical tracking space are necessary to determine the unknown transformation ${}^{image}\mathbf{T}_{world}$ between patient and image data. Superdimension Inc.[14] offers an commercial available navigated bronchoscopy system based on this registration procedure. The accuracy was tested by Schwarz *et al.* [70, 69] at several patients and the clinical applicability was proved.

Solomon *et al.* [73] tested this registration method with fiducial CT markers fixed at the patient's skin and anatomical landmarks in the airways. The second method showed better results compared to the fiducials and this proceeding additionally avoids a repeated CT data acquisition with attached fiducial CT markers. For the point-based approach typical registration points which are easy identified on the CT data and accessable by a bronchoscope in the human lung can be found at the Main Carina, Right-Upper Lobe Carina, Middle Lobe Carina, Left-Upper Lobe Carina or S6 Carina [41].

Hautmann *et al.* [30] proved that the navigated bronchoscopy approach in combination with a point-based registration procedure is applicable, accurate and safe in clinical settings. Four anatomical landmarks were used to examine the application at interventions of 16 patients. A fluoroscopy unit was used to verify the locations reported by the EMTS. The error at the registration points was approximately 5mm away from the real positions.

An error prediction model for the point-based registration was proposed by several researchers [46, 25, 87, 24] and is described in more detail in section 3.2. The error occuring during the data acquisition of the corresponding points in both image and physical space is called the fiducial localization error (FLE). It is strongly influenced by the inaccurate or distorted measurements of an EMTS, the difficulty to reach the desired landmarks exactly and the deformation of the bronchial wall. The resulting error after registration is called the target registration error (TRE) and provides a reliable prediction of the current system accuracy.

---

[14] http://www.superdimension.com/.

7.2.2 Surface-based registration

The surface based registration procedure uses a recorded trajectory of the EMTS output acquired during the routine examination of the airways. The necessary mapping ${}^{image}\mathbf{T}_{world}$ is computed automatically from the trajectory data without any time-consuming navigation to specific registration landmarks in the bronchus.

Deguchi *et al.* [16] computed the transformation from the recorded electromagnetic trajectory to a centerline of the airways by using ICP[15]. Furthermore, a similar fully automatic method was proposed by Klein *et al.* [42, 41] for the registration procedure in navigated bronchoscopy using the segmented bronchi extracted from the CT data. An additional optimization method (in volume maximization, IVM) was suggested to improve the results of the surface based computed transformation.

The advantages of this approach is clearly the unchanged medical workflow during a bronchoscopic intervention, the short data acquisition time during the routine examination of the airways and the reported high accuracy for determining the registration transformation between physical and image space.

7.2.3 Image-based registration

An alternative approach for registration in navigated bronchoscopy was proposed by Mori *et al.* [48, 51, 50] who used image-based methods to register the patient to the previously acquired CT scan. This method computes the necessary transformation by an image comparison between the bronchoscope real-time image and a vitual bronchoscopy image computed from the previously acquired CT scan. Additionally, the last bronchoscope position can be reused to speed up the technique which requires to find the best fitting pose from of a huge number of possible camera positions and orientations. It is essential to know the intrinsic camera parameters such as focal length, aspect ratio, camera projection center and especially distortion coefficients because the images of the bronchoscope camera are usually heavily barrel-type lens distorted and the resolution of its pictures is quite low.

Ishitani *et al.* [36] combined a calibrated camera system and an electromagnetic tracking system. One sensor measuring both position and orientation of the camera was placed at the tip of the flexible bronchoscope. By combining these techniques it is possible to superimpose the bronchoscope images with informations about anatomical structures and tissues beyond the bronchial wall in real-time.

---

[15] Iterative closest point (ICP) was proposed by Besl and McKay [7] and describes the matching of two point clouds by minimizing the distance between corresponding elements iteratively until convergence.

Additionally, Mori *et al.* [49, 52] proposed a way to track the camera motion of an endoscope by using epipolar geometry and combined that output with an image-based registration method. This approach does not require the use of an additional tracking system, however, the computation is usually time-consuming.

Problems of navigated bronchoscopy systems

In the future the described navigation system might be an useful application during bronchoscopic interventions, because these systems do not require radiation exposure and provide additional full 3D informations to the surgeon. Unfortunately, the system still suffers from the following problems:

- Movement of the patient during an bronchoscopic intervention.
- Respiration motion of the patient.
- Deformation of anatomical surfaces in the bronchus and at the patient's skin.
- EMTS errors caused by metallic distortions or inaccurate measurements.

Wegener *et al.* [84, 83] published a way to solve the inaccuracy problems caused by EMTS or point-based registration by mapping the measured position to the closest point on a previously computed centerline. This approach provides a much smoother motion of the bronchoscope position and guarantees the bronchoscope location to be inside the airways. The required centerline can be extracted from the CT data by a segmentation procedure [37, 75] before the medical intervention. The position correction is done by using both the centerline and the diameter of the segmented airways. The approach maps the (distorted) position of the electromagnetic tracker to the nearest centerline point in real-time. Unfortunately, this method seems to be hardly applicable if the target region (e.g. a tumor) is at a peripherial lung location where the airways are too small to compute usable centerlines and a feasible airways segmentation.

7.2.4 Experiments in the bronchoscopy room

The accuracy of electromagnetic tracking based applications (e.g. in navigated bronchoscopy) is influenced by distortions caused by conductive or ferromagnetic materials. Therefore, the experiments from section 6 were performed in the bronchoscopy room to measure the influence of electrical devices (e.g. endoscopes, monitors, light sources) and metallic objects (e.g. table, surgical instruments) in the intervention room. It is essential to analyse the operating volume before a bronchoscopic intervention to avoid sources of failure in the tracking area. However, this procedure is usually not applicable in daily medical practice because of the time-consuming data acquisition process. A reproducible experiment in both the bronchoscopy room and the laboratory was accomplished with the polycarbonate measurement plate to ensure comparablity between distorted and undistorted environments and to find sources of errors in the navigated bronchoscopy application.

Introduction and Experimental Setup

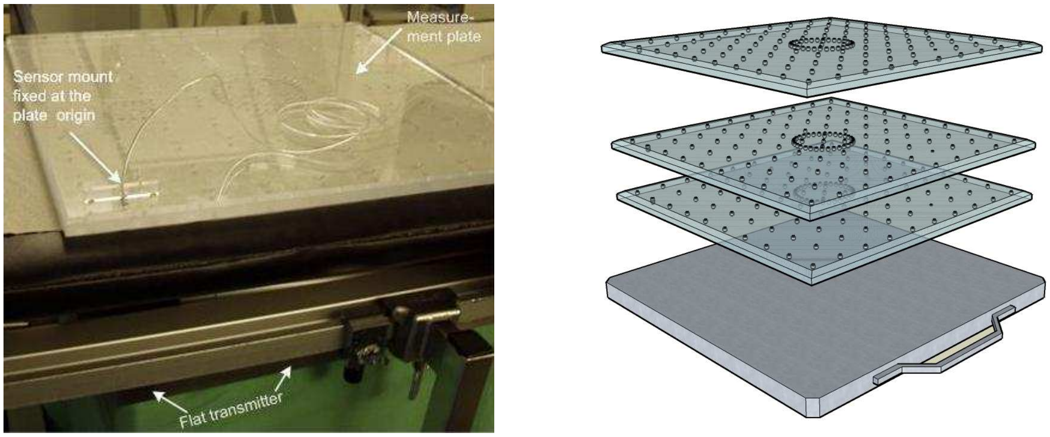

Figure 7.9: The **experimental setup** in the bronchoscopy room: The measurement plate of Hummel *et al.* [32, 33] was placed at 3 different positions (150mm, 240mm and 400mm) above the Ascension “3D Guidance” flat transmitter. The experiments were accomplished in a distortion free environment in the laboratory and in the bronchoscopy room where a number of metalic objects are present in the working volume.

The setup of the experiment is illustrated in figure 7.9. The flat transmitter of the Ascension “3D Guidance^{TM}” system was placed beneath the operating table[16] in the bronchoscopy room. The measurement plate was positioned with a distance of 150mm, 240 mm and

---

[16] The operating table contains metallic rods at its edges, but not directly in the tracking volume. Additionally, this is the most convenient position for both patient and surgeon during a bronchoscopic intervention.

400mm above. This protocol allows to reproduce the experiments in the distortion free environment of the laboratory with the polycarbonate plate and to compare the result of both settings to each other. Both jitter and positional error measurements were evaluated in a similar manner as in the previous experiments (see section 6) with the plate of Hummel *et al.* [32, 33].

Results

Major differences between both experimental setups can be seen at jitter error results.

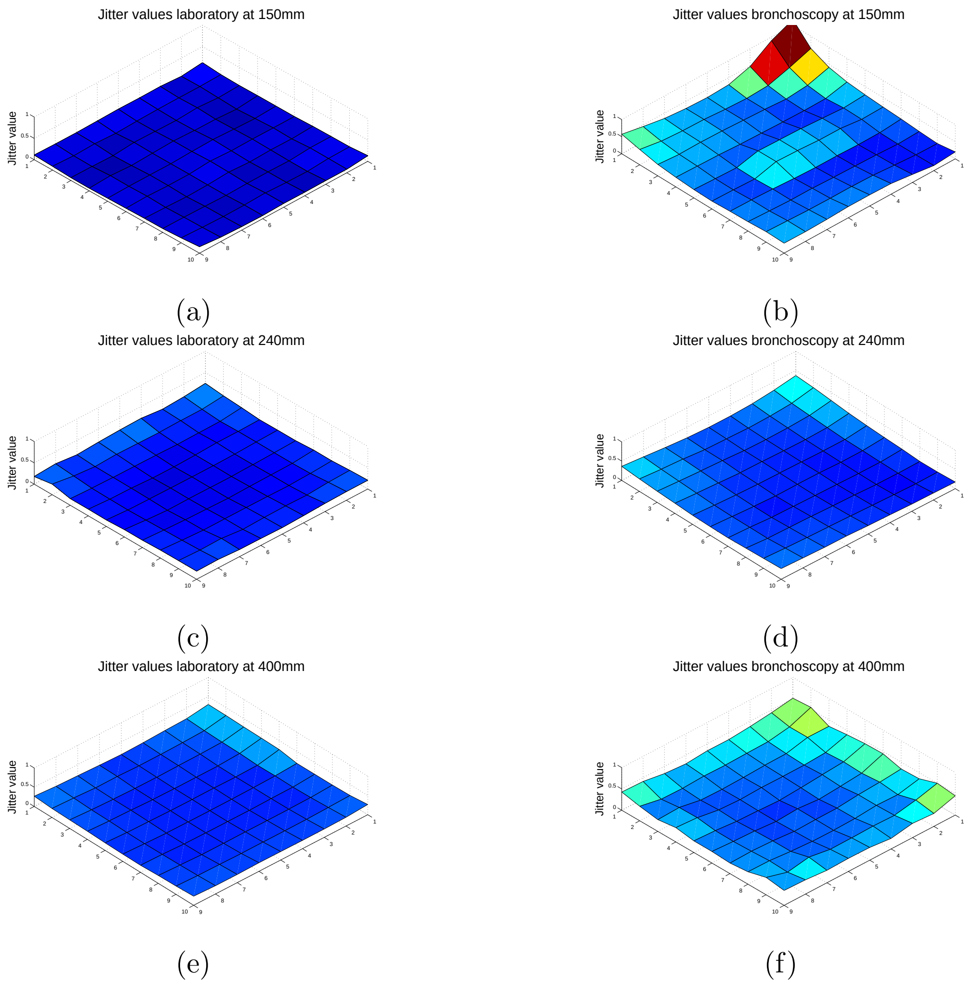

(a) (b) (c) (d) (e) (f)

Figure 7.10: The **jitter error** in the laboratory at 150mm (a), at 240mm (c) and at 400mm (e) as well as in the bronchoscopy room at 150mm (b), at 240mm (d) and at 400mm (f).

If the plate is positioned at 150mm above the transmitter, the laboratory experiments (0.0814±0.0183mm) were much better than the results in the medical environment (0.2775± 0.1464mm). Similarly, at the distance of 240mm from the field generator the laboratory results show lower values (0.1467±0.0362mm) compared to the bronchoscopy room (0.1995 ± 0.0553mm). At the highest gap between transmitter and measurement plate jitter errors are again quite different with a much higher value in the medical environment (0.2869±0.0804mm) compared to the distortion free setup (0.1864±0.0375mm). In total the avarage jitter was at (0.1381±0.0306mm) in the labaratory and at (0.2546±0.0940mm) in the bronchoscopy room. This shows clearly that the distorted environment is much more affected to jitter than the laboratory. The results of the jitter error experiments are summarized in table 6.1.

err_{jitter}	Laboratory	Bronchoscopy room
At 150mm	0.0814(±0.0183)mm	0.2775(±0.1464)mm
At 240mm	0.1467(±0.0362)mm	0.1995(±0.0553)mm
At 400mm	0.1864(±0.0375)mm	0.2869(±0.0804)mm
total	0.1381(±0.0306)mm	0.2546(±0.0940)mm

Table 7.2: The **jitter error results** in the labarotory and the bronchoscopy room. The table contains the evaluated mean and standard deviation values [in mm].

The evaluation of the mean positonal errors shows again a much better accuracy in the laboratory setup than in the bronchoscopy room (see figure 7.11). In both environments a higher distance error was observed at increased distances between the measurement positions.

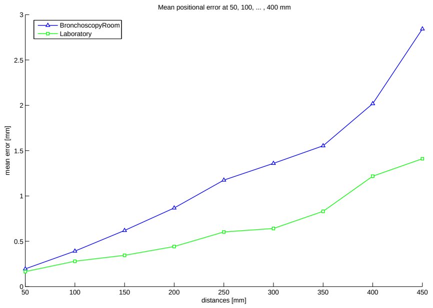

Figure 7.11: The mean **relative position error** in the bronchoscopy room and in the laboratory. All possible distances of $50mm, 100mm, ..., 450mm$ of the grid positions were calculated and compared to the metric distances of the plate.

The values recorded in the bronchoscopy room were constantly on a much higher distortion level at all examined distances (1.048 ± 1.2452mm) than in the laboratory (0.5919 ± 0.8314mm). The results of the mean position error are summarized in table 7.3.

err_{pos}	Laboratory	Bronchoscopy room
Distances of 50mm	0.1647(±1.4896)mm	0.1952(±1.1820)mm
Distances of 150mm	0.3449(±0.2184)mm	0.6191(±0.4211)mm
Distances of 300mm	0.6408(±0.5652)mm	1.3595(±1.1632)mm
Distances of 450mm	1.2175(±1.0527)mm	2.0182(±1.8224)mm
total	0.5919(±0.8314)mm	1.048(±1.2452)mm

Table 7.3: The **mean relative position error** results at different heights in the laboratory and the bronchoscopy room. The table contains the evaluated mean and standard deviation values [in mm].

Additionally, the cumulative row distance error is illustrated in figure 7.12. All plots show that the measurements in the bronchoscopy room are much more distorted than in the laboratory. Especially at the volume endings highly varying values are occuring in the intervention room. These errors might be caused by metallic rods in the operating table. The laboratory values are much more balanced at all observed distances from the transmitter.

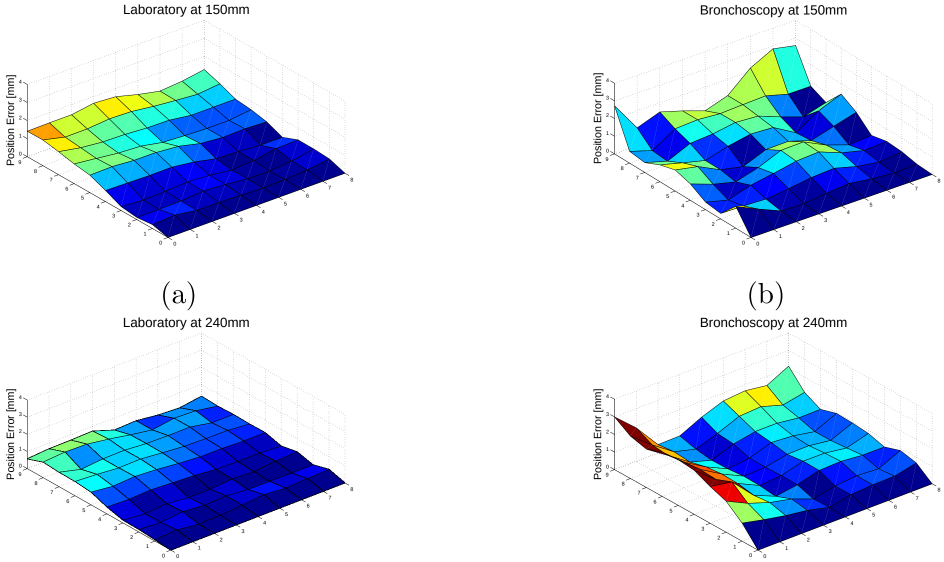

(a) (b)

(c) (d)

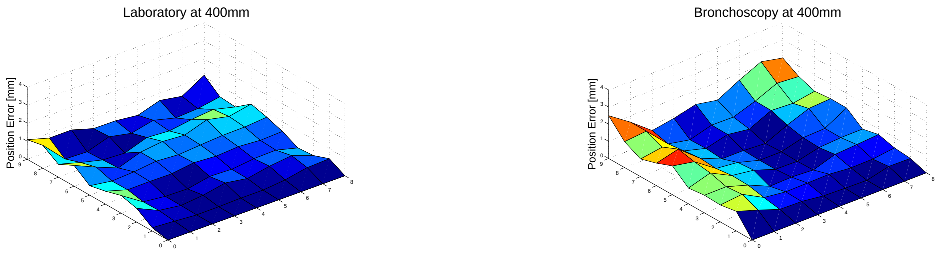

(e) (f)

Figure 7.12: The **cumulative row distance error** in the laboratory at 150mm (a), at 240mm (c) and at 400mm (e) as well as in the bronchoscopy room at 150mm (b), at 240mm (d) and at 400mm (f).

7.2.5 Discussion

A comparison between the distorted and undistorted experimental area shows clearly a reduced accuracy in the bronchoscopy room. The displayed cumulative row distance error can give an idea of distortion in the medical environment. Especially the border regions of the tracking volume were much more affected by varying values than the center of the working area. This might be caused by metallic rods which are present in operating table near the flat transmitter. Both mean jitter and positional error were about twice as big as in the undistorted laboratory environment.

The major source of the observed distortion in the bronchoscopy room is of a static nature. In this case it is possible to apply static error correction methods which are described in more detail in chapter 5. These techniques are able to correct erroneous measurements by computing an error compensation function. The data acquisition procedure can be done by using an optical tracking system or other high-precision detection methods. Afterwards, the error correction can be applied until the system setup is manipulated.

8 Conclusion

The negative influence of electromagnetic tracking errors on the accuracy of a number of applications in image-guided surgery encourages the consideration of the erroneous measurements on a lower level. The described error classification method allows to group the error into its subclasses and to draw conclusions about its origin. Positional and orientational errors can be classified into static and dynamic distorted data, where static errors can be grouped into jitter error and distortions caused by the influence of nearby metallic objects in the operating volume. Dynamic errors are either sensor movement or dynamically occuring field distortions in the tracking area. Robotic systems, measurement tools and optical tracking systems can be used to classify an occuring electromagnetic error and to measure the magnitude of its components. Error correction approaches can be applied to compensate the faulty tracking data and might play a major role in improved systems.

Several experiments were accomplished by using a high-precision measurement plate published in the work of Hummel *et al.* [32, 33]. Jitter, positional and rotational errors as well as metallic distortions were examined by a well-defined standardized assessment protocol which assures both comparablity to the results of related works and repeatablity of the experiments. The Ascension "3D Guidance^{TM}" system was investigated with a mid-range transmitter and a flat transmitter in combination with two receiver types of 1.8mm and 1.3mm diameter. Together with the published results of Hummel *et al.* [32, 33], which are analysed at the same measurement plate, it is possible to compare the performance of the "3D Guidance^{TM}" to the MicroBird system of Ascension and to the older and newer NDI Aurora system. Additionally, an user interface was implemented for online error tracking. The error components, which are determined by using a co-calibrated magneto-optical system, are displayed in some plots at runtime. Furthermore, this software allows to observe the quality value of Ascension. However, the magnitude of this value is sometimes deceptive and can just provide a non-reliable hint of the current distortion level. It strongly depends on the distance between receiver and transmitter.

The described navigated bronchoscopy and augmented camera systems might benefit from the presented error classification. The assessment experiments were performed in the bronchoscopy room and major distortions were observed for jitter and positional measurements probably caused by metallic objects. Theses errors influence the accuracy of the EMTS in the bronchoscopy room negatively. The mathematical background of augmented camera applications was presented in this thesis and the calibration procedure was implemented in combination with a special calibration pattern for heavily distorted optics.

8.1 Future Work

Detection of dynamic tracking errors

The focus of the experiments in this thesis was clearly at the detection of static errors like jitter errors and distortions caused by metallic objects. Several error detection methods are discussed in section 4 which facilitate the determination of dynamic electromagnetic tracking errors. Very few publications are released which determine the error values caused by fast sensor movements or dynamically inserted error sources. A future work is to determine the magnitude of dynamic occuring tracking errors in relation to the sensor velocity at the "3D Guidance^{TM}" system.

Error Propagation approaches

The lack of propagation models for a number of image-guided surgery systems is a major drawback for a common prediction of expected errors. The error propagation of the frequently used point-based registration method was discussed in more detail in this thesis and can be seen as an early prototype for error prediction in image-guided surgery applications. The development of new approaches for other registration or calibration procedures in medical navigation systems will be a key-issue to understand the relation of electromagnetic tracking errors and application errors in the future.

Error correction in the bronchoscopy room

The experiments in the bronchoscopy room clearly show big distortions caused by metallic rods in the tracking volume of the EMTS. The data acquisition process based on Hummel's measurement plate was a time-consuming procedure and is hardly applicable at the limited time before a bronchoscopic intervention. The use of an optical tracking system as secondary device and the appliance of an error correction method might reduce the negative influence of the detected metallic objects. However, this and the degree of improvement have to be evaluated in a set of standardized experiments applying error correction methods in the intervention room.

Framework with classified electromagnetic tracking errors

The implementation of a framework for EMTS errors which allows to detect the current error online, subdivides it into static and dynamic errors and further groups the static error into its subclasses is a further goal for future EMTS. For the initial experiments of this thesis a hybrid magneto-optical system was implemented to classify the occuring errors (see section 4.4). However, the use of an visual based tracking system as reference system is not applicable in many applications.

8.2 Results

The classification of errors occuring in EMTS is an useful technique to understand the nature of an occuring electromagnetic tracking error. The subdivision into its components is a possibility to detect error sources in the tracking volume and to draw conclusions about its origin. Error propagation models help to predict the occuring error in specific applications. Several experiments were accomplished to evaluate the magnitude of the classified error in this thesis. Additionally, in the initial experiments the Ascension quality number was observed by using a co-calibrated magneto-optical system. Its value seems not to be an adequate indicator of the current error reported by the tracking system, but depends more or less only on the transmitter/receiver distance. A classified error in combination with a specific propagation model provides a much better idea of the expected error in an application using EMTS. Furthermore, more reliable navigation interfaces can be implemented for a set of image-guided surgery systems.

Bibliography

[1] Advanced Realtime Tracking GmbH, *ARTtrack & DTrack Manual, version 1.20.*

[2] Advanced Realtime Tracking GmbH, *http://ar-tracking.de.* Internet, December 2007.

[3] Ascension Technology Corporation, *3D Guidance - Installation and Operation Guide, 940034 Rev A.* 9/29/06.

[4] Ascension Technology Corporation, *MicroBIRD technical reference guide, 910121 Rev A.*

[5] Ascension Technology Corporation, *http://www.ascension-tech.com.* Internet, December 2007.

[6] M. Bauer, M. Schlegel, D. Pustka, N. Navab, and G. Klinker, *Predicting and Estimating the Accuracy of n-occular Optical Tracking Systems*, in The Fifth IEEE and ACM International Symposium on Mixed and Augmented Reality, Santa Barbara, CA, USA, Oct. 22-25, 2006, 2006.

[7] P. Besl and N. McKay, *A Method for Registration of 3-D Shapes*, IEEE Trans. on Pattern Analysis and Machine Intelligence., 14(2), February 1992, pp. 239–256.

[8] W. Birkfellner, *Tracking Systems in Surgical Navigation*, PhD thesis, Department of Biomedical Engineering and Physics, General Hospital, University of Vienna, 2000.

[9] W. Birkfellner, F. Watzinger, F. Wanschitz, G. Enislidis, C. Kollmann, D. Rafolt, R. Nowotny, R. Ewers, and H. Bergmann, *Systematic Distortions in Magnetic Position Digitizers*, Medical Physics, 25(11), November 1998, pp. 2242–2248.

[10] W. Birkfellner, F. Watzinger, F. Wanschitz, G. Enislidis, M. Truppe, R. Ewers, and H. Bergmann, *Concepts and Results in the Development of a Hybrid Tracking System for CAS*, in Proc. Int'l Conf. Medical Image Computing and

Computer Assisted Intervention (MICCAI), Lecture Notes in Computer Science, 1998, pp. 343–351.

[11] W. Birkfellner, F. Watzinger, F. Wanschitz, R. Ewers, and H. Bergmann, *Calibration of Tracking Systems in a Surgical Environment*, IEEE Transactions on Medical Imaging, 17, No.5, 1998, pp. 737–742.

[12] T. Buzug, *Einführung in die Computertomographie. Mathematisch - physikalische Grundlagen der Bildrekonstruktion*, Springer-Verlag Berlin Heidelberg, 2004.

[13] A. Chung, P. Edwards, F. Deligianni, and G.-Z. Yang, *Freehand Cocalibration of Optical and Electromagnetic Trackers for Navigated Bronchoscopy*, MIAR, LNCS 3150, 2004, pp. 320–328.

[14] J. Craig, *Introduction to Robotics: Mechanics and Control*, Prentice Hall, 3nd ed., 2004.

[15] K. Daniilidis, *Hand-eye Calibration using Dual Quaternions*, International Journal of Robotics Research, 18, 1999, pp. 286–298.

[16] D. Deguchi, K. Ishitani, T. Kitasaka, K. Mori, Y. Suenaga, H. Takabatake, M. Mori, and H. Natori, *A method for bronchoscope tracking using position sensor without fiducial markers*, in SPIE Medical Imaging, 2007.

[17] P. Detmer, G. Bashein, T. Hodges, K. Beach, E. Filer, D. Burns, and D. Strandness Jr., *3D Ultrasound image feature localization based on magnetic scanhead tracking: in vitro calibration and validation*, Ultrasound in Medicine and Biology, 20(9), 1994, pp. 923–936.

[18] M. Feuerstein, *Augmented Reality in Laparoscopic Surgery - New Concepts for Intraoperative Multimodal Imaging*, PhD thesis, Technische Universität München, 2007.

[19] M. Feuerstein, T. Reichl, J. Vogel, A. Schneider, H. Feussner, and N. Navab, *Magneto-optic Tracking of a Flexible Laparoscopic Ultrasound Transducer for Laparoscope Augmentation*, in Proc. Int'l Conf. Medical Image Computing and Computer Assisted Intervention (MICCAI), 2007. To appear at Int'l Conf. Medical Image Computing and Computer Assisted Intervention (MICCAI).

[20] M. Feuerstein, T. Reichl, J. Vogel, J. Traub, and N. Navab, *Magneto-optic Tracking of a Flexible Laparoscopic Ultrasound Transducer for Online Detection and Correction of Dynamic Magnetic Field Distortions*, Submitted to IEEE Transactions of Medical Imaging, 2007.

[21] M. Feuerstein, S. Wildhirt, R. Bauernschmitt, and N. Navab, *Automatic Patient Registration for Port Placement in Minimally Invasive Endoscopic Surgery*, in Medical Image Computing and Computer-Assisted Intervention - MICCAI 2005, 8th International Conference, J. S. Duncan and G. Gerig, eds., vol. 3750 of Lecture Notes in Computer Science, Palm Springs, CA, USA, September 2005, Springer Verlag, pp. 287–294.

[22] G. Fischer, *Electromagnetic tracker characterization and optimal tool design (with application to ENT surgery)*, Master's thesis, Johns Hopkins University, April 2005.

[23] G. Fischer and R. Taylor, *Electromagnetic Tracker Measurement Error Simulation and Tool Design*, in Proc. Int'l Conf. Medical Image Computing and Computer Assisted Intervention (MICCAI), 2005.

[24] M. Fitzpatrick and J. West, *The Distribution of Target Registration Error in Rigid-Body Point-Based Registration*, IEEE Transactions on Medical Imaging, 20(9), 2001, pp. 917–927.

[25] M. Fitzpatrick, J. West, and C. Maurer Jr., *Predicting Error in Rigid-Body Point-Based Registration*, IEEE Trans. Med. Imag., 14(5), 1998, pp. 694–702.

[26] D. Frantz, A. Wiles, S. Leis, and S. Kirsch, *Accuracy assessment protocols for electromagnetic tracking systems*, Physics in Medicine and Biology, 48, 2003, pp. 2241–2251.

[27] C. Gramkow, *On Averaging Rotations*, Journal of Mathematical Imaging and Vision, 15, 2001, pp. 7–16.

[28] J. Hagedorn, S. Satterfield, and J. Kelso, *Correction of Location and Orientation Errors in Electromagnetic Motion Tracking*, Presence, 16(4), 2007, pp. 352–366.

[29] R. Hartley and A. Zisserman, *Multiple View Geometry in Computer Vision*, Cambridge University Press, 2nd ed., 2003.

[30] H. Hautmann, A. Schneider, T. Pinkau, F. Peltz, and H. Feussner, *Electromagnetic Catheter Navigation During Bronchoscopy: Validation of a Novel Method by Conventional Fluoroscopy*, Chest, 128, 2005, pp. 382–387.

[31] J. Heikkilä and O. Silvén, *A Four-step Camera Calibration Procedure with Implicit Image Correction*, in Proc. IEEE Conf. Computer Vision and Pattern Recognition (CVPR), IEEE Computer Society, 1997, pp. 1106–1112.

[32] J. Hummel, M. Bax, M. Figl, Y. Kang, C. Maurer Jr., W. Birkfellner, H. Bergmann, and R. Shahidi, *Design and Application of an Assessment Protocol for Electromagnetic Tracking Systems*, Medical Physics, 32(7), July 2005, pp. 2371–2379.

[33] J. Hummel, M. Figl, W. Birkfellner, M. Bax, R. Shahidi, C. Maurer Jr., and H. Bergmann, *Evaluation of a new electromagnetic tracking system using a standardized assessment protocol*, Physics in Medicine and Biology, 51, 2006, pp. 205–210.

[34] J. Hummel, M. Figl, C. Kollmann, and H. Bergmann, *Evaluation of a miniature electromagnetic position tracker*, Medical Physics, 29, 2002, pp. 2205–2212.

[35] M. Ikits, J. Brederson, C. Hansen, and J. Hollerbach, *An improved calibration framework for electromagnetic tracking devices*, Proc. IEEE Virtual Reality, 2001, pp. 63–70.

[36] K. Ishitani, D. Daisuke, T. Kitasaka, K. Mori, Y. Suenaga, H. Takabatake, Masaki, and H. Natori, *Easy and stable bronchoscope camera calibration technique for bronchoscope navigation system*, in Proc. of SPIE, vol. 6509, 2007.

[37] B. Jähne, *Digitale Bildverarbeitung. 6. überarbeitete und erweiterte Auflage*, Springer-Verlag Berlin Heidelberg, 2005.

[38] M. Johnson, *Exploiting Quaternions to Support Expressive Interactive Character Motion*, PhD thesis, Massachusetts Institute of Technology, 2003.

[39] S. Kaur, *Master Thesis: Error Correction for ElectroMagnetic Tracking*, Technische Universität München, 2006.

[40] V. Kindratenko, *A survey of electromagnetic position tracker calibration techniques*, Virtual Reality: Research, Development and Applications, 5(3), 2000, pp. 169–182.

[41] T. Klein, *Diploma Thesis: Fiducial Free Registration Procedure for Navigated Bronchoscopy*, Technische Universität München, 2007.

[42] T. Klein, J. Traub, H. Hautmann, A. Ahmadian, and N. Navab, *Fiducial-Free Registration Procedure for Navigated Bronchoscopy*, in Proc. Int'l Conf. Medical Image Computing and Computer Assisted Intervention (MICCAI), Lecture Notes in Computer Science, Brisbane, Australia, October/November 2007, Springer Verlag.

[43] K. Levenberg, *A Method for the Solution of Certain Problems in Least Squares*, Quarterly of Applied Mathematics, 2, 1944, pp. 164–168.

[44] M. Livingston and A. State, *Magnetic Tracker Calibration for Improved Augmented Reality Registration*, Presence: Teleoperators and Virtual Environments, 6(5), 1997, pp. 532–546.

[45] D. Marquardt, *An Algorithm for Least-Squares Estimation of Nonlinear Parameters*, Journal of the Society for Industrial and Applied Mathematics, 11(2), June 1963, pp. 431–441.

[46] C. Maurer Jr., M. Fitzpatrick, M. Wang, R. Galloway Jr., R. Maciunas, and G. Allen, *Registration of Head Volume Images Using Implantable Fiducial Markers*, IEEE Trans. Med. Imag., 16(4), 1997, pp. 447–462.

[47] A. Mor, *Accuracy of dynamic electromagnetic tracking*, Journal of Biomechanics, 39 (Suppl. 1), 2006, pp. 556–557.

[48] K. Mori, D. Deguchi, K. Akiyama, T. Kitasaka, C. Maurer Jr., Y. Suenaga, H. Takabatake, M. Mori, and H. Natori, *Hybrid Bronchoscope Tracking Using a Magnetic Tracking Sensor and Image Registration*, in Proc. Int'l Conf. Medical Image Computing and Computer Assisted Intervention (MICCAI), Springer-Verlag, 2005, pp. 543–550.

[49] K. Mori, D. Deguchi, J. Hasegawa, Y. Suenaga, J. Toriwaki, H. Takabatake, and H. Natori, *A Method for Tracking the Camera Motion of Real Endoscope by Epipolar Geometry Analysis and Virtual Endoscopy System*, in Proc. Int'l Conf. Medical Image Computing and Computer Assisted Intervention (MICCAI), Springer-Verlag, 2001, pp. 1–8.

[50] K. Mori, D. Deguchi, K. Ishitani, T. Kitasaka, Y. Suenaga, Y. Hasegawa, K. Imaizumi, and H. Takabatake, *Bronchoscope Tracking Without Fiducial Markers Using Ultra-tiny Electromagnetic Tracking System and its Evaluation in Different Environments*, in Proc. Int'l Conf. Medical Image Computing and Computer Assisted Intervention (MICCAI), vol. 4792 of Lecture Notes in Computer Science, Springer-Verlag, 2007, pp. 644–651.

[51] K. Mori, D. Deguchi, T. Kitasaka, Y. Suenaga, H. Takabatake, M. Mori, H. Natori, and C. Maurer, *Bronchoscope Tracking Based on Image Registration Using Multiple Initial Starting Points Estimated by Motion Prediction*, in Proc. Int'l Conf. Medical Image Computing and Computer Assisted Intervention (MICCAI), R. Larsen, M. Nielsen, and J. Sporring, eds., vol. 4191 of Lecture Notes in Computer Science, Springer-Verlag, 2006, pp. 645–652.

[52] K. Mori, D. Deguchi, J. Sugiyama, Y. Suenaga, J. Toriwaki, C. Maurer Jr., H. Takabatake, and H. Natori, *Tracking of a bronchoscope using epipolar geometry analysis and intensity-based image registration of real and virtual endoscopic images*, Medical Image Analysis, 6, 2002, pp. 321–336.

[53] D. Mucha, B. Kosmecki, and J. Bier, *Plausibility check for error compensation in electromagnetic navigation in endoscopic sinus surgery*, International Journal of Computer Assisted Radiology and Surgery, 1, 2006, pp. 316–318.

[54] C. Nafis, V. Jensen, L. Beauregard, and P. Anderson, *Method for estimating dynamic EM tracking accuracy of Surgical Navigation tools*, in SPIE, 2006.

[55] K. Nakada, M. Nakamoto, Y. Sato, K. Konishi, M. Hashizume, and S. Tamura, *A Rapid Method for Magnetic Tracker Calibration Using a Magneto-Optic Hybrid Tracker*, in Proc. Int'l Conf. Medical Image Computing and Computer Assisted Intervention (MICCAI), R. E. Ellis and T. M. Peters, eds., vol. 2879 of Lecture Notes in Computer Science, Springer-Verlag, 2003, pp. 285–293.

[56] M. Nakamoto, Y. Sato, M. Miyamoto, K. Konishi, Y. Nakamjima, M. Shimada, M. Hashizume, and S. Tamura, *3D Ultrasound System Using a Magneto-optic Hybrid Tracker for Augmented Reality Visualization in Laparoscopic Liver Surgery*, in Proc. Int'l Conf. Medical Image Computing and Computer Assisted Intervention (MICCAI), 2002.

[57] National Cancer Institute, *Bronchoscopy.* Internet, December 2007.

[58] M. Nixon, B. McCallum, R. Fright, and B. Price, *The Effects of Metals and Interfering Fields on Electromagnetic Trackers*, Presence, 7(2), 1998, pp. 204–218.

[59] Northern Digital Inc., *System Guide, Rev 1.0 Sept 2003*, 2003. http://www.ndigital.com.

[60] Northern Digital Inc., *User Guide, Rev 1.0 Sept 2003*, 2003. http://www.ndigital.com.

[61] Northern Digital Inc., *http://www.ndigital.com.* Internet, December 2007.

[62] W. Press, S. Teukolsky, and W. Vetting, *Numerical Recipes in C: The Art of Scientific Computing*, Cambridge University Press, 2nd ed., 1993.

[63] F. Raab, E. Blood, T. Steiner, and H. Jones, *Magnetic Position and Orientation Tracking System*, IEEE Transactions on aerospace and electronic systems, AES-15, No.5, 1979, pp. 709–718.

[64] T. Reichl, *Diploma Thesis: Online Error Correction for the Tracking of Laparoscopic Ultrasound*, Technische Universität München, 2007.

[65] T. Saleh, V. Kindratenko, and W. Sherman, *On Using Neural Networks to Calibrate Electromagnetic Tracking Systems*, submitted to Virtual Reality: Reasearch, Development and Applications, 2000.

[66] K. Schicho, M. Figl, M. Donat, W. Birkfellner, R. Seemann, A. Wagner, H. Bergmann, and R. Ewers, *Stability of miniature electromagnetic tracking systems*, Physics in Medicine and Biology, 50, 2005, pp. 2089–2098.

[67] J. Schmidt, F. Vogt, and H. Niemann, *Robust Hand-Eye Calibration*, in 25. Symposium für Mustererkennung, DAGM 2003, Magdeburg, B. Michaelis and G. Krell, eds., vol. 2781 of LNCS, Springer-Verlag, Berlin, 2003.

[68] M. Schneider and C. Stevens, *Development and testing of a new magnetic-tracking device for image guidance*, SPIE 2007, 6509, 2007.

[69] Y. Schwarz, J. Greif, H. Becker, A. Ernst, and A. Mehta, *Real-time electromagnetic navigation bronchoscopy to peripheral lung lesions using overlaid CT images: The first human study*, in Chest, vol. 129, 2006, pp. 988–994.

[70] Y. Schwarz, A. Mehta, A. Ernst, F. Herth, A. Engel, D. Besser, and H. Becker, *Electromagnetic Navigation during Flexible Bronchoscopy*, in Respiration 2003, vol. 70, 2003, pp. 516–522.

[71] T. Sielhorst, M. Bauer, O. Wenisch, G. Klinker, and N. Navab, *Online Estimation of the Target Registration Error for n-ocular Optical Tracking Systems*, in Proceedings of Medical Image Computing and Computer-Assisted Intervention (MICCAI 2007), Brisbane, Australia, October 2007, June 2007.

[72] T. Sielhorst, M. Feuerstein, J. Traub, O. Kutter, and N. Navab, *CAMPAR: A software framework guaranteeing quality for medical augmented reality*, Computer Assisted Radiology and Surgery (CARS), 1, 2006, pp. 29–30.

[73] S. Solomon, P. White Jr., C. Wiener, J. Orens, and K. Wang, *Three-dimensional CT-Guided Bronchoscopy With a Real-Time Electromagnetic Position Sensor: A Comparison of Two Image Registration Methods*, Chest, 118, 2000, pp. 1783–1787.

[74] C. Thormann, *Diploma Thesis: Fast and efficient error correction of electromagnetic tracking and its application in prostate cancer treatment*, Technische Universität München, 2007.

[75] K. Tönnies, *Grundlagen der Bildverarbeitung*, Pearson Studium, 2005.

[76] J. Traub, S. Kaur, P. Kneschaurek, and N. Navab, *Evaluation of Electromagnetic Error Correction Methods*, Bildverarbeitung fuer die Medizin (BVM 2007), 2007.

[77] J. Traub, P. Stefan, S.-M. Heining, T. Sielhorst, C. Riquarts, E. Euler, and N. Navab, *Hybrid navigation interface for orthopedic and trauma surgery*, in Proceedings of MICCAI 2006, LNCS, Copenhagen, Denmark, Oct. 2006, MICCAI Society, Springer, pp. 373–380.

[78] J. Traub, P. Stefan, S.-M. Heining, T. Sielhorst, C. Riquarts, E. Euler, and N. Navab, *Towards a Hybrid Navigation Interface: Comparison of a Slice Based Navigation System with In-situ Visualization*, in Proceedings of MIAR 2006, LNCS, Shanghai, China, Aug. 2006, Springer, pp. 364–372.

[79] G. Treece, A. Gee, R. Prager, C. Cash, and L. Berman, *High-Definition Freehand 3-D Ultrasound*, Ultrasound in Medicine and Biology, 29(4), 2003, pp. 529–546.

[80] R. Tsai, *A versatile Camera Calibration Technique for High Accuracy 3D machine Vision Metrology Using Off-the-shelf TV Cameras and Lenses*, IEEE Journal of Robotics and Automation, RA-3(4), 1987, pp. 323–344.

[81] R. Tsai and R. Lenz, *Real Time Versatile Robotics Hand/Eye Calibration using 3D Machine Vision*, in Proceedings of the IEEE International Conference on Robotics and Automation, vol. 1, 1988, pp. 554–561.

[82] M. Walker, L. Shao, and R. Volz, *Estimating 3-D location parameters using dual number quaternions*, CVGIP: Image Underst., 54(3), 1991, pp. 358–367.

[83] I. Wegner, J. Biederer, R. Tetzlaff, I. Wolf, and H.-P. Meinzer, *Evaluation and extension of a navigation system for bronchoscopy inside human lungs*, in SPIE Medical Imaging, 2007.

[84] I. Wegner, M. Vetter, I. Wolf, and H.-P. Meinzer, *Development of a navigation system for endoluminal brachytherapy in human lungs*, SPIE Medical Imaging: Visualization, Image-Guided Procedures, and Display, 6141(6141), 2006, pp. 23–30.

[85] T. Wendler, J. Traub, S. Ziegler, and N. Navab, *Navigated three dimensional beta probe for optimal cancer resection*, in Proceedings of MICCAI 2006, R. Larsen, M. Nielsen, and J. Sporring, eds., vol. 4190(1) of LNCS, Copenhagen, Denmark, Oct.

2006, MICCAI Society, Springer, pp. 561–569.

[86] C. Wengert, M. Reeff, P. C. Cattin, and G. Szekely, *Fully Automatic Endoscope Calibration for Intraoperative Use*, Bildverarbeitung fr die Medizin 2006, 8, 2006, pp. 419–423.

[87] J. West and M. Fitzpatrick, *The Distribution of Target Registration Error in Rigid-Body, Point-Based Registration*, in IPMI '99: Proceedings of the 16th International Conference on Information Processing in Medical Imaging, London, UK, 1999, Springer-Verlag, pp. 460–465.

[88] J. West, M. Fitzpatrick, S. Toms, C. Maurer Jr., and R. Maciunas, *Fiducial point placement and the accuracy of point-based, rigid body registration*, Neurosurgery, 48(4), 2001, pp. 810–817.

[89] J. West and C. Maurer Jr, *Designing Optically Tracked Instruments for Image-Guided Surgery*, IEEE Transactions on Medical Imaging, 23(5), 2004, pp. 533–545.

[90] X. Wu and R. Taylor, *A Direction Space Interpolation Technique for Calibration of Electromagnetic Surgical Navigation Systems*, in Proc. Int'l Conf. Medical Image Computing and Computer Assisted Intervention (MICCAI), R. E. Ellis and T. M. Peters, eds., vol. 2879 of Lecture Notes in Computer Science, Springer-Verlag, 2003, pp. 215–222.

[91] T. Yamaguchi, M. Nakamoto, Y. Sato, K. Konishi, Y. Nakajima, T. Nishii, N. Sugano, M. Hashizume, H. Yoshikawa, K. Yonenobu, and S. Tamura, *Camera Model and Calibration Procedure for Oblique-Viewing Endoscope*, in Proc. Int'l Conf. Medical Image Computing and Computer Assisted Intervention (MICCAI), R. E. Ellis and T. M. Peters, eds., LNCS, Springer-Verlag, 2003, pp. 373–381.

[92] T. Yamaguchi, M. Nakamoto, Y. Sato, K. Konishi, N. Sugano, M. Hashizume, H. Yoshikawa, and S. Tamura, *Development of a camera model and calibration procedure for oblique-viewing endoscopes*, Computer Aided Surgery, 9, 2004, pp. 203–214.

[93] G. Zachmann, *Distortion Correction of Magnetic Fields for Position Tracking*, in Proc. Computer Graphics International (CGI'97), Belgium, June 23-27, 1997.

[94] G. Zachmann, *Virtual Reality in Assembly Simulation – Collision Detection, Simulation Algorithms and Interaction Techniques*, PhD thesis, Technische Universität Darmstadt, 2000.

[95] C. Zhang, J. Helferty, G. McLennan, and W. Higgins, *Nonlinear distortion correction in endoscopic video images*, International Conference on Image Processing, 2000, pp. 439–442.

[96] Z. Zhang, *Flexible Camera Calibration By Viewing a Plane From Unknown Orientations*, International Conference on Computer Vision, 1999, pp. 666–673.

[97] Y. Zhigang and Y. Kui, *An improved 6DOF Electromagnetic Tracking Algorithm with Anisotropic System Parameters*, Edutainment, Springer LNCS 3942, 2006, pp. 1141–1150.